STABILITY OF LIQUID FILMS AND DROPLETS ON POROUS-GRANULAR BEDS

A thesis submitted

in partial fulfillment of the requirements

for the degree of

Doctor of Philosophy

by

A. Ananth Praveen Kumar

Department of Chemical Engineering

Indian Institute of Technology Guwahati

July 2013

CERTIFICATE

It is certified that the work contained in this thesis entitled **“Stability of Liquid Films and Droplets on Porous-Granular Beds”**, by A. Ananth Praveen Kumar, has been carried out under our supervision and that this work has not been submitted elsewhere for a degree.

Thesis Supervisor	*Thesis Co-supervisor*
Dr. Dipankar Bandyopadhyay	**Dr. Tamal Banerjee**
Assistant Professor	Associate Professor
Department of Chemical Engineering	Department of Chemical Engineering
Indian Institute of Technology Guwahati	Indian Institute of Technology Guwahati

July 2013

ACKNOWLEDGEMENT

Working for this PhD has been an unforgettable experience for me and it would not possible without these people.

First and foremost, I would like to thank my thesis supervisors **Dr. Dipankar Bandyopadhyay** and **Dr. Tamal Banerjee** for giving me an opportunity to work in a very interesting area of research. I am very grateful to Dr. Dipankar Bandyopadhyay for his continuous guidance, important advices and stimulating discussions. In spite of his busy schedule he always took time to analyze problems and gave needed suggestions for the betterment of my work. Some of his remarkable qualities, such as his depth of perfection and lucid presentation, will always continue to inspire me. The experience of working with him will have far-reaching influence in my future life. I consider it an honor to work under him.

I would like to express my deepest gratitude to Dr. Tamal Banerjee for his insightful comments and suggestions thought-out my research work. His continuous encouragement and support gave me a lot of inspiration to carry out this research work.

It gives me great pleasure in acknowledge the support and help of **Prof. R. Usha**, Department of Mathematics, Indian Institute of Technology Madras.

I would like to thank my doctoral committee members, **Dr. Anugrah Singh, Dr. Kaustubha Mohanty**, **Dr. Ashok Kumar Das Mahapatra**, Department of Chemical Engineering and **Dr. Arnab Kumar De,** Department of Mechanical Engineering, for their valuable suggestion and effort which made my thesis successful.

My sincere thanks to **Mr. Kartick Mondal**, research scholar of our research group, for his co-operative assistance in learning the basics concepts and provided me constant source of encouragement throughout my PhD.

I am particularly grateful to **Mr. Himanshu goyal** and **Mr. Venkatanarayana Prasad S**. for their support in computation and experiments. I am also thankful to present research group members **Mr. Bolledu Ravi, Mr. Amit Kumar Singh, Mr. Seim**

Timung, Mr. Saptak Rarotra, Mr. Vijeet Tiwari, Mr. Sunny Kumar, Mr. Nilanjan Mandal, Mr. Abhinav Sharma, Mr. Viswanath Pasumarthi, and **Ms. Abhijna Das.**

I would like to thank my fellow research scholars **Mr. Venkata Swamy Nalajala, Mr. Satyannarayana Edubilli, Mr. Vijay Singh, Mr. Anand Babu Desamala,** and **Mr. Leela Manohar.**

I cannot forget to thank my friends **Mr. Appaji Posina, Mr. Anoop Kishore, Mr. Diwakar Reddy, Mr. Ayanavilli Srinivas, Mr. B. Manohar, Mr. Girivasu Pavuluri,** and **Mr. Gouri Shankar Cheripally** for the lovely support in making my stay at IIT Guwahati memorable.

Above all, I would like to thank my **parents, sisters,** and **brother-in-laws** for their love and support throughout everything, as always. Finally, my fiancée **Swarupa** deserve a special mention for her love and persistent confidence in me, has taken the load off my shoulders.

I dedicate this thesis to *My Family.*

A. Ananth Praveen Kumar

SYNOPSIS

Stability of Liquid Films and Droplets on Porous-Granular Beds

The hydrodynamic instabilities of superposed fluid layers have sparked research interest over the years because of their appearance in diverse applications ranging from simple oil-water two-phase flows, complex co-extrusion of polymer melts to the flow of cryolite/Aluminum (Al) melts in a conventional Al reduction cell. An important issue in this regard is the stability of the interface between the fluids because a stable interface is essential to ensure desired mechanical, optical and barrier properties of the products. In contrast, a highly unstable interface finds important applications in enhanced mass, momentum, and heat transfer, especially in the micro/nano scale devices. The stability/instability of the interface depends on several factors such as the properties of the fluids and the confining substrates, the viscosity and/or density stratification of the liquid layers, thickness ratio of the layers jump in the velocities or the stresses across the interface and so on.

The recent advent of microfluidic devices indicates that the flows and instabilities of single and multilayer liquids can potentially be exploited for micro/nanoscale mixing, heat and mass transfer and pumping. A number of investigations have shown the influence of porous and rough substrates on the flows in the microfluidic devices, fuel cells, biological membranes, and micro-electro-mechanical-systems (MEMS), and micropores of oil reservoirs. These studies highlight that the flow physics in the smaller dimensions can be notably different from the same in the macroscopic domain because even a little roughness, porosity, permeability, and slippage at the bounding surfaces can significantly alter the flow pattern. Among the previous theoretical studies related to the macroscopic flows over porous media, the studies mentioned consider either the instabilities of a single film flowing on a porous medium or the instabilities of a two-layer plane Poiseuille flow (PPF) when confined between non-porous substrates.

1. Instabilities of a confined two-layer flow on a porous medium

The hydrodynamic instabilities of a pair of immiscible liquid films flowing on a porous medium is another interesting system and yet to be explored in detail. Herein, with the help of an Orr-Sommerfeld (O-S) analysis of the governing equations and boundary conditions, the instabilities of a two-layer flow confined between a Darcy-Brinkman porous medium (PPFPM) and a rigid substrate have been explored. In order to ensure the accuracy of the results, the O-S system is solved employing two different numerical techniques and validated with the available asymptotic cases. The study reveals that similar to PPF, the PPFPM is unstable by long-wave interfacial and finite wavenumber shear modes of instabilities. PPFPM shows the coexistence of the dominant or subdominant interfacial and shear modes beyond a critical porosity, permeability, and thickness of the porous layer, for any combination of viscosity ratio (μ_r) and thickness ratio (h_r) of the liquid layers. This is in contrast with the two-layer PPF results where the interfacial and shear mode instabilities occur for $\mu_r > h_r^2$ and $\mu_r < h_r^2$, respectively, when the films are of equal density. Interestingly, the parameters characterizing porous medium profoundly influence the time and the length scales of the shear mode whereas the interfacial mode remains rather insensitive to these parameters. For example, the strength of the shear mode increases with, (i) increase in porosity, (ii) initially increases and then becomes constant with increase in the thickness, (iii) initially increases and then reduces with the increase in permeability, and (iv) reduces with the increase in the stress jump coefficient across the porous-liquid interface. Further, the effects of porosity, thickness, and permeability of the porous layer on the instabilities of inclined and non-inclined PPFPM have been compared to understand the influence of the gravitational field on the instability modes.

2. Instabilities of a Couette two-layer flow on a porous medium

The instabilities of a plane two-layer Couette flow confined between a rigid and a Darcy-Brinkman porous medium (CFPM) is investigated through a detailed O-S analysis. The study seamlessly compares and contrasts both macro- and microscopic features of the different instability modes of CFPM. Similar to two-layer PPF, the CFPM is found to be unstable by the long-wave interfacial and the finite wavenumber shear modes. Interestingly, we observe the presence of twin shear modes for a CFPM in which one shows its dependence on the velocity of the bounding surface whereas the other is responsive to the flow inside the porous layer. The strength of these shear modes are tunable with the thickness, porosity, and permeability of the porous layer together with the plate velocity whereas the interfacial mode remains rather insensitive to these changes. The shear modes emerge stronger than the interfacial mode when the frictional influence is reduced in the CFPM by increasing the porosity, thickness, and permeability of the porous layer or when the bounding plate velocity is moved faster. The conditions for the co-existence and dominance of all these modes are explored for a large parameter space, which can be of importance in the studies related to the microscale mixing and heat and mass transfer employing two-layer flows.

3. Instabilities of free bilayer flow on a inclined porous medium

The instability of gravity driven bilayer flow on a Darcy-Brinkman porous medium is another interesting system. A linear stability analysis of the conservation laws leads to an O-S system, which is solved numerically with appropriate boundary conditions to identify the time and length scales of the instability modes. At the liquid-liquid interface due to viscosity stratification and at liquid-air interface due to surface tension there present two interfacial modes of instabilities. The study uncovers that the inclination of the porous medium together with the slippage at the porous-liquid interface originating from the flow inside the porous layer can fuel up a pair of finite wavenumber shear modes in addition to the twin interfacial modes of instabilities. Interestingly, strength of one of the shear modes is found to increase with the increase in Reynolds number whereas the other shear mode gains strength in presence of highly porous, permeable, and thick porous layer. The strength of the porous media shear mode increases with, (i) increase in porosity, (ii) initially increases and then becomes constant with increase in the thickness, and (iii) initially increases and then reduces with the increase in permeability.

The parameter space reported reflects the salient features of both macroscopic and microscopic flows. The results showing the augmented destabilizing influence of the porous layer on the plain Poiseuille flow, Couette flow, and bilayer flow can be of importance especially in improving the mixing, heat and mass transfer, emulsification, and phase separation of multiphase flows.

4. Dynamics of a Liquid Droplet on a Granular Bed of Micro-Structured Particles

Dynamics and morphologies of droplet permeation on a loosely bound porous-granular bed composed of micro-porous and micro-patterned particles have been explored. Naturally abundant particles such as *Cycas revoluta* (sago), *Papaver somniferum* (poppy), and *Sinapis alba* (mustard), have been employed to prepare homogenous and heterogeneous porous-granular beds. The experiments uncovered that a bed of bigger mustard particles can not only stabilize a static water lens by pinning the three-phase contact line on the micro-patterns decorated on the particle surfaces but also dynamically convert a water lens to 'liquid marbles' when the granular bed is composed of smaller poppy particles having a micro-patterned surface similar to the mustard particles. Computational studies identified that the flow inside the droplet originating from coupled influence of the drop deformation and recoil together with the vertical capillary force at the pinned three-phase contact line of the droplet could convert a water lens to a liquid marble when the particles are smaller and the gravitational pull is below a critical value. In contrast to the micro-patterned particles, the smaller micro-porous particles were also found to show a phenomenon similar to marble effect in which the hydrophilic particles remain embedded inside the droplet surface rather than hanging outside, as observed for the poppy particles. The simulations uncovered that an air current issuing out of the porous bed owing to the droplet seepage enforces the smaller micro-porous particles to dislodge from the bed and develop a marble effect type scenario. Heterogeneous porous-granular beds composed of mustard-poppy combination show a coupling of 'lens' formation and 'marble effect' at the two-parts of the droplet whereas a poppy-crushed sago combination show the two-different types of marble effect occurring simultaneously at the same droplet from different sides. The study on the kinetics of the drop permeation unfold that the rate of permeation is much slower when the drop passes through the bed-air interface than when a part of the drop seeped inside the bed. Addition of surfactant to the water droplet showed a faster permeation of the droplet, which also ensured a smaller life time for the lens and marble formation. Arguably, for the first time, the study uncovers a multitude of interesting dynamics of droplets over granular beds composed of particles with micro-porous and micro-patterned surface.

In summary, the thesis focuses on the theoretical and experimental understanding of the stability, dynamics and morphologies of the liquid layers and droplets on porous-granular beds. The outcomes of this research work will not only enhance the basic understanding of these configurations but also contribute in the applications related to the microscale flow over porous medium.

CONTENTS

LIST OF TABLES

LIST OF FIGURES

Figure No. **Page No.**

NOMENCLATURE

μ_j	Viscosity of the j^{th} layer
μ_e	Effective viscosity of the film in porous media
ρ_j	Density of the j^{th} layer
γ_1	Interfacial tension
γ_2	Surface tension
α	Angle of inclination
β	Composite thickness of the two liquid layers
d	Porous media thickness
$b\,,\delta$	Porosity
κ	Permeability
ξ	Stress jump coefficient
ϕ	Void fraction
Da	Darcy number
Re	Reynolds number
D_m	Dimensionless porous media thickness
χ	Dimensionless stress jump coefficient
G	Galileo number
Γ_1	Dimensionless interfacial tension
Γ_2	Dimensionless surface tension

K, $K_{\max}$, K_c	Dimensionless: wave number, dominant wave number, critical wave number
C	Complex eigenvalue
C_i, C_r	Imaginary, real part of the complex eigenvalue
h_0	Mean thickness of the lower layer
h_1	Variable thickness of the lower layer
h_2	Variable composite thickness of the upper layer in free bilayer system
H_0	Dimensionless mean thickness of the lower layer
H_1	Dimensionless thickness of the lower layer
H_2	Dimensionless composite thickness of two-liquids in free bilayer system
B	Dimensionless composite thickness of two-liquids in confined bilayer system
t	Dimensional time
T	Dimensionless time
x, y, z	Dimensional *x*-axis, *y*-axis, *z*-axis
X, Y, Z	Dimensionless: *X*-axis, *Y*-axis, *Z*-axis
O-S	Orr-Sommerfeld
PPF	Two-layer plane Poiseuille flow
PPFPM	Two-layer plane Poiseuille flow confined between a rigid wall and a Darcy-Brinkman porous medium
CFPM	Two-layer Couette flow confined between a rigid wall and a Darcy-Brinkman porous medium

Chapter 1

Introduction

1.1 INSTABILITIES IN MULTIPHASE FLOW

The stability and dynamics of pressure-driven stratified flow of a pair of liquid layers have been studied over the years because of their presence in a variety of important scientific and technological prototypes such as oil-water flow, extrusion of polymers,[1-3] electrochemical cells,[4] fuel cells,[5] microfluidic devices,[6-7] and bio-processes.[8] An important issue is the stability of the interface between the fluids because a stable interface is essential to ensure desired mechanical, optical and barrier properties of the products. In contrast, a highly unstable interface finds important applications in enhanced mass, momentum, and heat transfer, especially in the micro/nano scale devices. The stability or instability of the interface depends on several factors such as the properties of the fluids and the confining substrates, the viscosity and/or density stratification of the liquid layers, thickness ratio of the layers jump in the velocities or the stresses across the interface and so on. Extensive theoretical[9-15] and experimental[16,17] efforts have been invested in exploring the salient features of the instabilities of the stratified two-layer fluid flows.

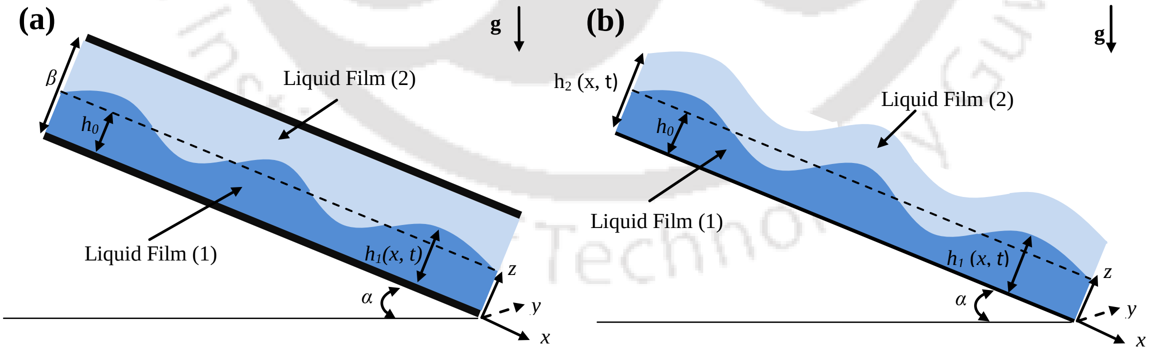

Figure 1.1: Schematic diagram representing (a) two-layer flow inside a confined inclined channel (b) free bilayer on an inclined solid substrate. Where β is composite thickness of the two liquid layers, h_0 is mean thickness of the lower layer, h_1 is variable thickness of the lower layer, h_2 variable composite thickness of the upper layer, α is angle of inclination, and **g** is acceleration due to gravity.

A pioneering study by Yih[9] considered the pressure-driven two-layer Plane Poiseuille (PPF) and Couette (CF) [Figure1.1(a)] flows of two stratified fluids and uncovered that viscosity stratification alone can engender a long-wave interfacial mode of instability even at vanishingly small Reynolds numbers. Subsequently, it was found that the interfacial mode can also exist in a two-layer pipe flow.[18] Later, the importance of the volume ratio of the liquid layers on the interfacial stability was also established.[19] Hooper and Boyd[20] were the first to show that, beyond a threshold flow rate, a two-layer CF can undergo an additional finite-wave number shear flow mode of instability. The origin of the shear mode was attributed to the destabilizing Reynolds stresses across the liquid layers beyond the laminar regime of the flow,[20,21] which is also recognized as Tollmein-Schlichting instability in a single layer PPF.[22] Yiantsios and Higgins,[12] Hooper[23] summarized that in the absence of gravity, a two layer PPF is neutrally stable when $\mu_r = h_r^2$ because of the fading shear rate near the interface. Here μ_r and h_r denote viscosity and the thickness ratios of the liquid layers, respectively. Importantly, the studies infer that the interfacial mode (shear mode) can be present only when the condition $\mu_r > h_r^2$ ($\mu_r < h_r^2$) is met for a two-layer PPF with liquid layers of equal density.

Apart from the linear theories, the nonlinear instability of a pair of superposed viscous fluids in a channel showed that the linearly unstable interface can evolve into undisturbed state or to a finite amplitude steady state when the capillary forces or the nonlinear effects are dominant.[24] Further, a long-wave instability was observed for the configuration with more viscous lower layer confined between a semi-infinite upper layer and a solid wall.[25] However, the same configuration showed a stable interface when the less viscous fluid was placed next to the wall.[10, 23, 26] Later, this lubrication effect in multilayer flows were also experimentally realized along with an explanation through a unified theory.[27-29] In addition to the horizontal pressure driven flows, the free surface instabilities of inclined single layer flows have also attracted attention.[30-34] A number of previous studies uncovered the spatiotemporal interfacial structures resulting from the instabilities of this configuration.[35-40] The horizontal and inclined channel two-phase flows can be unstable by long wave and finite wavenumber instabilities.[14,15] The details of the various instabilities of two-layer flows can be found in some excellent review articles.[41-44]

The instabilities of the free bilayer systems also uncover many interesting aspects of fundamental science which includes the origin of the squeezing (varicose) or bending (sinuous) modes at the coupled deformable interfaces, pattern formation, phase separation of immiscible layers, formation of embedded and encapsulated droplets, coalescence or pinching-off of the droplets, and the motion of three-phase contact line, among many others.[45-47] The instabilities in free bilayers [Figure 1.1(b)] are rather different than the same in the confined bilayers because of the presence of the twin interfacial modes at the coupled deformable gas-liquid free-surface and the liquid-liquid interface. Kao[48-50] was the first to identify these modes appear only beyond a critical Reynolds number while considering the effects of both viscosity and density stratifications. Later, it was found that much like the confined bilayers the interfacial mode of instability was more apparent when upper layer is more viscous[51,52] and the wavelength of the instabilities at the free-surface and the interface show a resonance while evolving spatiotemporally.[53] The traveling interfacial modes under varied conditions were also simulated employing long-wave nonlinear simulations to uncover the role of the interfacial shear on the evolution of the instability.[54-56] Attempts were made to predict the wave velocity and growth rate of the interfacial modes employing a longitudinal velocity perturbation associated with the surface and interfacial deflections.[57] Further, a lot of attention has been paid to uncover the convective nature of the unstable modes[58] and also to identify the flexibility of the underlying substrate.[59] Importantly, other than the viscosity and density stratification, the interfacial modes of instabilities of a free bilayer down an inclined plane can be under various stabilizing or destabilizing inertial influences depending on the position of the more or the less viscous liquid film.[59] For example, when the less viscous fluid is adjacent to the inclined wall, inertia was found to stabilize the interfacial mode at the liquid-liquid interface whereas the same effect destabilizes the liquid-air free-surface. In contrast, inertia destabilizes both the interfacial modes when the more viscous layer is adjacent to the inclined wall.

1.2 INSTABILITIES IN POROUS-MEDIA FLOW

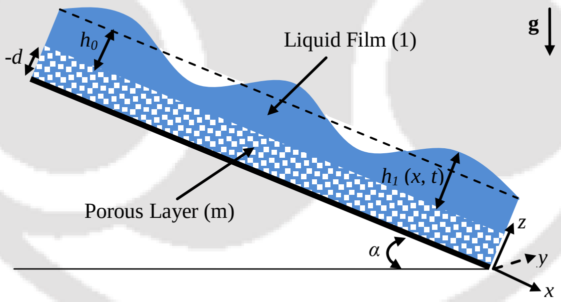

Figure 1.2: Schematic diagram of liquid-layer flow over an inclined porous substrate. Where h_0 is mean thickness of the lower layer, h_1 is variable thickness of the lower layer, d is thickness of the porous media, α is angle of inclination, and **g** is acceleration due to gravity.

The recent advent of microfluidic devices indicates that the flows and instabilities of single and multilayer liquids can potentially be exploited for micro/nanoscale mixing,[60-66] micro/nanoscale pattern formation,[67,68] heat and mass transfer[62,69] and pumping.[70-72] A number of investigations have shown the influence of porous and rough substrates on the flows in the microfluidic devices, fuel cells, biological membranes, and micro-electro-mechanical-systems (MEMS), and micropores of oil reservoirs.[5-8] These studies highlight that the flow-physics in the smaller dimensions can be notably different from the same in the macroscopic domain because even a little roughness, porosity, permeability, and slippage at the bounding surfaces can significantly alter the flow pattern. Among the previous theoretical studies related to the macroscopic flows over porous media, Beavers and Joseph[73] showed that the flow of liquid over a porous bed (Figure 1.2) can be studied by enforcing a semi-empirical slip boundary condition at the porous-liquid interface in the Stokes flow regime. Later, Darcy's law was employed for the porous medium to show the destabilizing influence of the permeability at the free surface of a thin film flowing down an inclined porous plane.[74,75] The influence of permeability and surface tension on the amplitude and shape of the surface waves of a film flowing on a porous substrate[76-79] had also been explored. A recent work employed a generic Darcy-Brinkman transport equation to model the porous medium and performed a long-wave analysis to show the influence of porosity, permeability, and stress jump coefficient on the free surface instabilities of a thin film flowing over a heated porous substrate.[80-82] They showed that this continuum approach suits very well for a porous medium with high permeability and at low permeability, the results of which match asymptotically with one-sided model results with appropriate slip coefficient. Further, a series of recent work on the Orr-Sommerfeld (O-S) analysis of thin films on inclined porous planes highlight the importance of the Darcy-Brinkman approach in predicting different instability modes.[83-85] A collection of works by Hill and Straughan[86-90] further corroborate the comprehensiveness of the Darcy-Brinkman description in resolving the different modes of the instabilities of a single layer PPF on a porous medium especially when the porous medium is highly permeable.

1.3 DYNAMICS OF DROPLETS ON POROUS GRANULAR BEDS

Natural surfaces have inspired the usage of micro or nanoscale engineering for ages on the development of artificial functional surfaces. While the vibrant peacock feathers triggered the development of synthetic surfaces that can emit structural colours, the lotus leaf (*Nelumbo nucifera*) prompted the use of hierarchical patterns in the development of self-cleaning water repelling surfaces.[96-98] The properties of functional surfaces are often tested through the droplet splashing experiment, which also manifests fascinating crater or corona or bell or crown shaped morphologies, under varied conditions.[99-101] A deeper understanding on the scientific and technological aspects of these phenomena has improved the efficiency of a range of applications which includes ink-jet printing, spray painting, fuel combustion, pesticide delivery, and electro-spinning, among many others.[100-103]

The impact of objects into a pool of liquid or with a solid surface have been extensively studied in the past and the physics associated with these phenomena is now fairly well understood.[100,104,105] In comparison, the impact of a liquid droplet on a bed of granular particles (porous-granular bed) imitating the impact of a raindrop into a bed of soil has started gaining attention only recently owing to its complex but interesting physics.[106-127] Impact and subsequent permeation of a liquid droplet through a porous-granular bed also finds important applications in the trickle bed reactors, ink-jet printing, food engineering, rain water harvesting, heap leaching in mineral processing, coated pill fabrication, and starch wetting. The characteristics of a porous-granular bed are rather different from similar solid or liquid beds because of the dissipative nature of frictional and collisional forces acting on the bed particles.[128] A collection of granular particles behave like a porous solid bed in absence of any external influence. However, influence of external fields or shear or vibration arising from the movement of the interstitial fluid can move a bed of particles like a complex fluid. Recent experiments confirmed that the splashing of a water droplet on a hydrophobic porous-granular bed (powder or sand) could form interesting crater or pie or donut shaped patterns on the bed-surface in which the viscous and capillary forces plays a decisive role in determining the bed morphologies.[106-111] The impact of a water droplet on a bed of hydrophobic particles can also form ‘liquid marbles’ – a liquid core encapsulated by poorly wetting particles,[112-127] which find important applications in the storage and transportation of active materials.[117-124]

From the computational point of view spreading of droplets on porous beds have been studied over the years based on approximate analytical methods and numerical modeling.[129-132] The studies uncovered that a droplet on a porous layer with the no-slip condition undergoes deformation at the initial stages in which the thickness increases near the contact line due to capillary pressure. These studies also discuss diverse features of the complete wetting and partial wetting scenarios when the capillary number is low. The theoretical predictions have also been validated with the experiments on spreading radius, injection velosity for complete wetting and partial wetting cases. In the present work, we perform full fledged numerical simulations of the experimental system to uncover interesting aspects of the drop permation through porous-granula beds.

1.4 OBJECTIVES OF THE THESIS

The aim of the thesis is to explore the possible instability modes in two-layer free and confined flows when bounded by a porous substrate. For this purpose, three different configurations have been considered for the study namely, (i) a confined two-layer plane Poiseuille flow in an inclined channel, (ii) a confined two-layer Couette flow in a confined channel, and (iii) flow of a free bilayer in an inclined channel. The dynamics of droplets on porous granular beds have also been studied through experiments and simulations.

In chapter-2, the hydrodynamic instabilities of a confined bilayer on an inclined Darcy-Brinkman porous layer have been explored with the help of an O-S analysis. The O-S equations have been numerically solved with appropriate boundary conditions to identify the time and length scales of the instabilities. This study points out the two modes of instability (i) long-wave interfacial mode – engendered by the viscosity stratification across the interface and (ii) finite wavenumber shear mode – originating from the inertial stresses. By changing the porous media parameters like porosity, porous media thickness, permeability and surface roughness, the origin and development of different instability modes have been explored in this chapter.

In chapter-3, we further destabilize the configuration by moving the upper surface, and find out an extra shear mode originating from the shear of the upper plate. The base flow replicates a Couette type confined bilayer two-phase flow, which appear very frequently in diverse applications. The instability modes observed in this chapter can be of importance for the studies related to the microfluidic devices having a moving boundary, which can significantly influence the flow patterns inside the channel.

In chapter-4, the instabilities of an inclined free bilayer flowing over a Darcy-Brinkman porous layer is considered. An O-S analysis of the governing equations and boundary conditions uncover that the pair of interfaces together with the presence of the porous media engenders, (i) a pair of long-wave interfacial mode at the interfaces, and (ii) a porous media shear mode generated by the slippage at liquid-porous interface.

In chapter-5, the dynamics and morphologies of droplet permeation on loosely bound porous beds composed of micro-porous and micro-patterned granular particles have been explored. Experiments are done on naturally abundant particles such as *Cycas revoluta* (sago), *Papaver somniferum* (poppy), and *Sinapis alba* (mustard). The dynamics of drop permeation for different types of beds were analysed through computational fluid dynamic (CFD) simulations, which uncovered different origins for the marble formation on beds with micro-patterned and micro-porous particles.

Concisely, we explore a host of interesting open problems, which can provide important observations on the stability and dynamics of the droplets and films inside micro- and macroscopic configurations.

Chapter 2

Instabilities of a confined two-layer flow on a porous medium

ABSTRACT

Instabilities of a pressure driven two-layer plane Poiseuille flow confined between a rigid wall and a Darcy-Brinkman porous layer are explored. A linear stability analysis of the conservation laws leads to an Orr-Sommerfeld system, which is solved numerically with appropriate boundary conditions to identify the time and length scales of the instabilities. The study uncovers the coexistence of twin instability modes, (i) long-wave interfacial mode – engendered by the viscosity stratification across the interface and (ii) finite wavenumber shear mode – originating from the inertial stresses, for almost all combinations of the viscosity (μ_r) and thickness (h_r) ratios of the liquid layers. The presence of the porous layer reduces the frictional influence on the films, which significantly alters the length and time scales of the shear mode while the interfacial mode remains dormant to this effect. This is in stark contrast to the two-layer flow confined between non-porous plates where an unstable interfacial (shear) mode is observed when $\mu_r > h_r^2$ ($\mu_r < h_r^2$). The study reveals that strength of the shear mode, (a) increases with porosity, (b) initially increases and then becomes constant with porous layer thickness, (c) initially increases then reduces with increase in permeability, and (d) reduce with increase in the stress jump coefficient at the porous-liquid interface. Moreover, the gravity expedites the destabilization of both the modes in the inclined channels as compared to the similar non-inclined channels. The parametric study presented can find important applications in enhancing heat and mass transfer, mixing, and emulsification especially in the microscale flows.

This chapter is published in *Chem. Eng. Sci.*, 97, 109-125 (2013).

2.1 INTRODUCTION

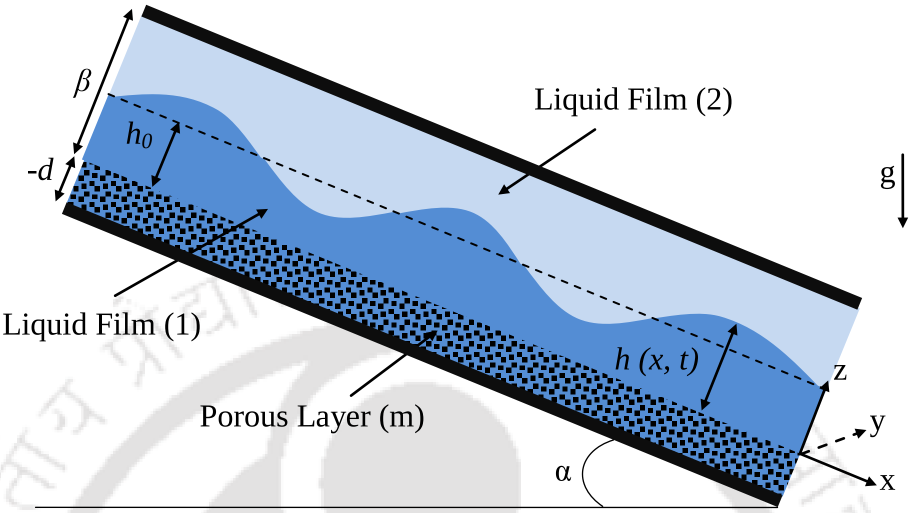

Figure 2.1: Schematic diagram of a two-layer flow inside a channel confined between a porous and a non-porous substrate. Where β is composite thickness of the two liquid layers, h_0 is mean thickness of the lower layer, h is variable thickness of the lower layer, d is thickness of the porous media, α is angle of inclination, and **g** is acceleration due to gravity.

The hydrodynamic instabilities of a pair of immiscible liquid films flowing on a porous medium (Figure 2.1) is another interesting system and yet to be explored in detail. Herein, with the help of an Orr-Sommerfeld (O-S) analysis of the governing equations and boundary conditions, the instabilities of a two-layer plane Poiseuille flow confined between a rigid wall and a Darcy-Brinkman porous medium (PPFPM) have been explored. In order to ensure the accuracy of the results, the O-S system is solved employing two different numerical techniques and validated with the available asymptotic cases. The study reveals that similar to plane Poiseuille flow (PPF), the PPFPM is unstable by long-wave interfacial and finite wavenumber shear modes of instabilities. PPFPM shows the coexistence of the dominant or subdominant interfacial and shear modes beyond a critical porosity, permeability, and thickness of the porous layer, for any combination of μ_r and h_r of the liquid layers. This is in contrast with the two-layer PPF results where the interfacial and shear mode instabilities occur for $\mu_r > h_r^2$ and $\mu_r < h_r^2$, respectively, when the films are of equal density.[12] Interestingly, the parameters characterizing porous medium profoundly influence the time and the length scales of the shear mode whereas the interfacial mode remains rather insensitive to these parameters. For example, the strength of the shear mode increases with, (i) increase in porosity, (ii) initially increases and then becomes constant with increase in the thickness, (iii) initially increases and then reduces with the increase in permeability, and (iv) reduces with the increase in the stress jump coefficient across the porous-liquid interface. Further, the effects of porosity, thickness, and permeability of the porous layer on the instabilities of inclined and non-inclined PPFPM have been compared to understand the influence of the gravitational field on the instability modes. The parameter space reported reflects the salient features of both macroscopic and microscopic flows. The results showing the augmented destabilizing influence of the porous layer on the PPFPM can be of importance especially in improving the mixing, heat and mass transfer, emulsification, and phase separation of multiphase flows.

This chapter is organized in the following manner. In Sec. 2.2, the details of the governing equations and boundary conditions are discussed. Brief outlines of the base state analysis and discussion on the base state velocity profiles are presented in Sec. 2.3. In Sec. 2.4, the linear stability analysis is described concisely and the details are shown in the Appendix A. In Sec. 2.5, the numerical methods to solve the O-S equation are discussed and the results are validated with the previous investigations. The results are analyzed in detail in the Sec.2.6 before concluding with important observations in the Sec 2.7.

2.2 PROBLEM FORMULATION

A Cartesian coordinate system is employed with the origin fixed at the porous substrate-lower layer interface $(z=0)$ and the unit vectors ($\mathbf{e_x}$, $\mathbf{e_y}$, $\mathbf{e_z}$) directed along the *x*-, *y*-, and *z*- directions as schematically shown in Figure 2.1. In the formulation, the variables for the lower and upper liquid layers are denoted by the subscripts *1* and *2*, respectively, and the porous medium variables are denoted by the subscript *m*. We assume a two-dimensional (2D) flow of Newtonian, incompressible, and immiscible liquid films with constant density, ρ_j and viscosity, μ_j, over a Darcy-Brinkman porous medium of porosity *b*, permeability κ, and thickness *d*. A general formulation is presented for the inclined channels, which asymptotically reduces to the non-inclined case when the angle of inclination α is set to zero.

The conservation of mass and momentum for the fluid layers (*j* = *1* and *2*) are,

$$\nabla\cdot\mathbf{u}_j=0, \tag{2.1}$$

$$\rho_j\left[\dot{\mathbf{u}}_j+\left(\mathbf{u}_j\cdot\nabla\right)\mathbf{u}_j\right]=-\nabla p_j+\mu_j\nabla^2\mathbf{u}_j+\rho_j\mathbf{g}. \tag{2.2}$$

The governing equations for the Darcy-Brinkman porous medium[80,81,83,91,92] are,

$$\nabla\cdot\mathbf{u}_m=0, \tag{2.3}$$

$$\frac{\rho_1}{b}\dot{\mathbf{u}}_m=-\nabla p_m+\mu_e\nabla^2\mathbf{u}_m-\frac{\mu_1}{\kappa}\mathbf{u}_m+\rho_1\mathbf{g}. \tag{2.4}$$

Where $\mathbf{g}$, $\mathbf{u}_j\left\{u_j,w_j\right\}$, and p_j represent, acceleration due to gravity, velocity vectors, and pressure for layer j = *1*, *2*, and *m*, respectively, μ_e is the effective viscosity. The over-dots in the equations represent the time derivative. The ratio of the lower layer viscosity to the effective viscosity of the porous layer is defined as the porosity ($b = \mu_1 / \mu_e$) of the porous medium.

No-slip and impermeability conditions are applied at the porous-solid ($z = -d$) and liquid-solid ($z = \beta$) boundaries are given by,

$$\mathbf{u}_m = 0, \tag{2.5}$$

$$\mathbf{u}_2 = 0. \tag{2.6}$$

Where β represents the combined thickness of the liquid layers. The continuity of normal stresses and velocities are enforced as boundary conditions along with the jump in the tangential stress at the lower layer-porous medium interface ($z = 0$),

$$\mathbf{u}_1 = \mathbf{u}_m, \tag{2.7}$$

$$-p_m + 2\mu_e w_{mz} = -p_1 + 2\mu_1 w_{1z}, \tag{2.8}$$

$$\mu_e u_{mz} - \mu_1 u_{1z} = \frac{\xi}{\sqrt{\kappa}} u_m . \tag{2.9}$$

Where jump coefficient ξ is the measure of spatial heterogeneity of the porous medium-lower layer interfacial region.[92] The subscripts x and z denote the partial derivatives of the variables. The balances of the normal and tangential stresses and the continuity of the velocities are enforced as boundary conditions at the liquid-liquid interface ($z = h$),

$$\mathbf{n} \cdot \overline{\boldsymbol{\tau}}_2 \cdot \mathbf{n} - \mathbf{n} \cdot \overline{\boldsymbol{\tau}}_1 \cdot \mathbf{n} = \gamma \left(\nabla \cdot \mathbf{n} \right), \tag{2.10}$$

$$\mathbf{t} \cdot \overline{\boldsymbol{\tau}}_2 \cdot \mathbf{n} = \mathbf{t} \cdot \overline{\boldsymbol{\tau}}_1 \cdot \mathbf{n}, \tag{2.11}$$

$$\mathbf{u}_1 = \mathbf{u}_2 . \tag{2.12}$$

Where γ represents the interfacial tension of the liquid-liquid interface, $\overline{\boldsymbol{\tau}}_j$ is the stress tensor, ∇ is gradient operator, $\mathbf{n}\left[\left(-h_x\big/\sqrt{\left(1+h_x^2\right)},1\big/\sqrt{\left(1+h_x^2\right)}\right)\right]$ is outward normal vector and $\mathbf{t}\left[\left(1\big/\sqrt{\left(1+h_x^2\right)},h_x\big/\sqrt{\left(1+h_x^2\right)}\right)\right]$ represent tangent vector. The location of the interface $(y=h)$ is defined by the kinematic condition,

$$\dot{h}=-u_1\left(\partial h/\partial x\right)+w_1. \tag{2.13}$$

The dimensional governing equations and the boundary conditions [Eqs. (2.1) – (2.13)] are transformed into non-dimensional forms employing the thickness of the lower layer (h_0) as length scale and $\rho_1 h_0^2/\mu_1$, as the viscous time scale. The dimensionless variables employed are, $X=x/h_0$, $Z=z/h_0$, $H=h/h_0$, $T=t\mu_1/\rho_1 h_0^2$, $\mathbf{U}_j=\mathbf{u}_j\rho_1 h_0/\mu_1$, $\rho_r=\rho_2/\rho_1$, $\mu_r=\mu_2/\mu_1$, $B=\beta/h_0$, $h_r=B-1$, $D_m=d/h_0$, $G=gh_0^{\,3}\big/\nu_1^{\,2}$, and $P_j=p_j h_0^2\rho_1/\mu_1^2$.

The resulting dimensionless continuity equations for the liquid layers and the porous medium are,

$$U_{1X}+W_{1Z}=0, \tag{2.14}$$

$$U_{2X}+W_{2Z}=0, \tag{2.15}$$

$$U_{mX}+W_{mZ}=0. \tag{2.16}$$

Here subscripts X and Z denote partial derivatives. The dimensionless equations of motions for the liquid layers and the porous layer are,

$$\dot{U}_1+U_1U_{1X}+W_1U_{1Z}=-P_{1X}+\left(U_{1XX}+U_{1ZZ}\right)+G\sin\alpha, \tag{2.17}$$

$$\dot{W}_1 + U_1 W_{1X} + W_1 W_{1Z} = -P_{1Z} + \left(W_{1XX} + W_{1ZZ}\right) - G\cos\alpha\,, \tag{2.18}$$

$$\rho_r\left(\dot{U}_2 + U_2 U_{2X} + W_2 U_{2Z}\right) = -P_{2X} + \mu_r\left(U_{2XX} + U_{2ZZ}\right) + \rho_r G\sin\alpha\,, \tag{2.19}$$

$$\rho_r\left(\dot{W}_2 + U_2 W_{2X} + W_2 W_{2Z}\right) = -P_{2Z} + \mu_r\left(W_{2XX} + W_{2ZZ}\right) - \rho_r G\cos\alpha\,, \tag{2.20}$$

$$(1/b)\dot{U}_m = -P_{mX} + (1/b)\left(U_{mXX} + U_{mZZ}\right) - (1/Da)U_m + G\sin\alpha\,, \tag{2.21}$$

$$(1/b)\dot{W}_m = -P_{mZ} + (1/b)\left(W_{mXX} + W_{mZZ}\right) - (1/Da)W_m - G\cos\alpha\,. \tag{2.22}$$

The dimensionless no-slip and impermeability boundary condition at the porous-solid interface $\left(Z = -D_m\right)$ and at the liquid-solid interface $\left(Z = B\right)$ are,

$$U_m = W_m = 0\,, \tag{2.23}$$

$$U_2 = W_2 = 0\,. \tag{2.24}$$

The continuity of velocities, normal stress balance, and the stress jump conditions at the liquid-porous interface $\left(Z = 0\right)$ have the following non-dimensional forms,

$$U_1 = U_m\,, \tag{2.25}$$

$$W_1 = W_m\,, \tag{2.26}$$

$$(1/b)U_{mZ} - U_{1Z} - \left(\chi/\sqrt{Da}\right)U_m = 0\,, \tag{2.27}$$

$$P_1 - P_m + 2\left((1/b)W_{mZ} - W_{1Z}\right) = 0\,. \tag{2.28}$$

The continuity of velocities, normal and tangential stress balances, and the kinematic equation at the liquid-liquid interface $\left(Z = H\right)$ have the following non-dimensional forms,

$$U_1 = U_2\,, \tag{2.29}$$

$$W_1 = W_2\,, \tag{2.30}$$

$$P_2 - P_1 + \frac{2}{\left[1+H_X^2\right]}\left\{\begin{matrix}\left[\left(\left(1-H_X^2\right)W_{1Z} - H_X\left(W_{1X}+U_{1Z}\right)\right)\right] \\ -\mu_r\left[\left(1-H_X^2\right)W_{2Z} - H_X\left(W_{2X}+U_{2Z}\right)\right]\end{matrix}\right\} = \frac{\Gamma H_{XX}}{\left[1+H_X^2\right]^{\frac{3}{2}}}, \tag{2.31}$$

$$\left[\left(U_{1Z}+W_{1X}\right)\left(1-H_X^2\right)+2H_X\left(W_{1Z}-U_{1X}\right)\right]-\mu_r\begin{bmatrix}\left(U_{2Z}+W_{2X}\right)\left(1-H_X^2\right) \\ +2H_X\left(W_{2Z}-U_{2X}\right)\end{bmatrix}=0, \tag{2.32}$$

$$\dot{H} = -U_1 H_X + W_1. \tag{2.33}$$

In Eqs. (2.14) – (2.33) the dimensionless numbers, $Da = \kappa / h_0^2$, $\chi = \xi / \mu_1$, $b = \mu_1 / \mu_e$, $D_m = d / h_0, G = g h_0^{\,3} / \nu_1^{\,2}$, and $\Gamma = \gamma h_0 / \rho_1 \nu_1^2$ denote dimensionless permeability (Darcy number), stress jump coefficient, porosity, thickness of the porous layer, gravity (Galileo number), and surface tension (Capillary number), respectively. In terms of the dimensionless variables, at the base state the lower, upper, and porous layers occupy, $0 \le Z \le H$, $H \le Z \le B$ and $-D_m \le Z \le 0$, respectively, where $H(X,T)$ describes the location of the interface between fluids. In what follows, unless otherwise mentioned, the discussions are carried out in terms of the non-dimensional variables.

2.3 BASE STATE ANALYSIS

The governing equations are solved for the unperturbed interface to obtain the steady base state solutions of the *x*-directional flow by setting,

$$H = 1,\ \bar{W}_j = 0 \text{ and } U_j = \bar{U}_j(Z)\ (j = 1, 2, \text{and } m). \tag{2.34}$$

Where the over-bars indicate base state solutions. The expressions for the steady-state velocity profiles obtained from the base state governing equations are,

$$\bar{U}_1 = C_{11}Z^2 + C_{12}Z + C_{13},\ \ 0 \le Z \le 1, \tag{2.35}$$

$$\bar{U}_2 = C_{21}Z^2 + C_{22}Z + C_{23},\ \ 1 \le Z \le B, \tag{2.36}$$

$$\bar{U}_m = C_{m1}\,\mathrm{e}^{MZ} + C_{m2}\,\mathrm{e}^{-MZ} + C_{m3}, \quad -D_m \le Z \le 0\,. \tag{2.37}$$

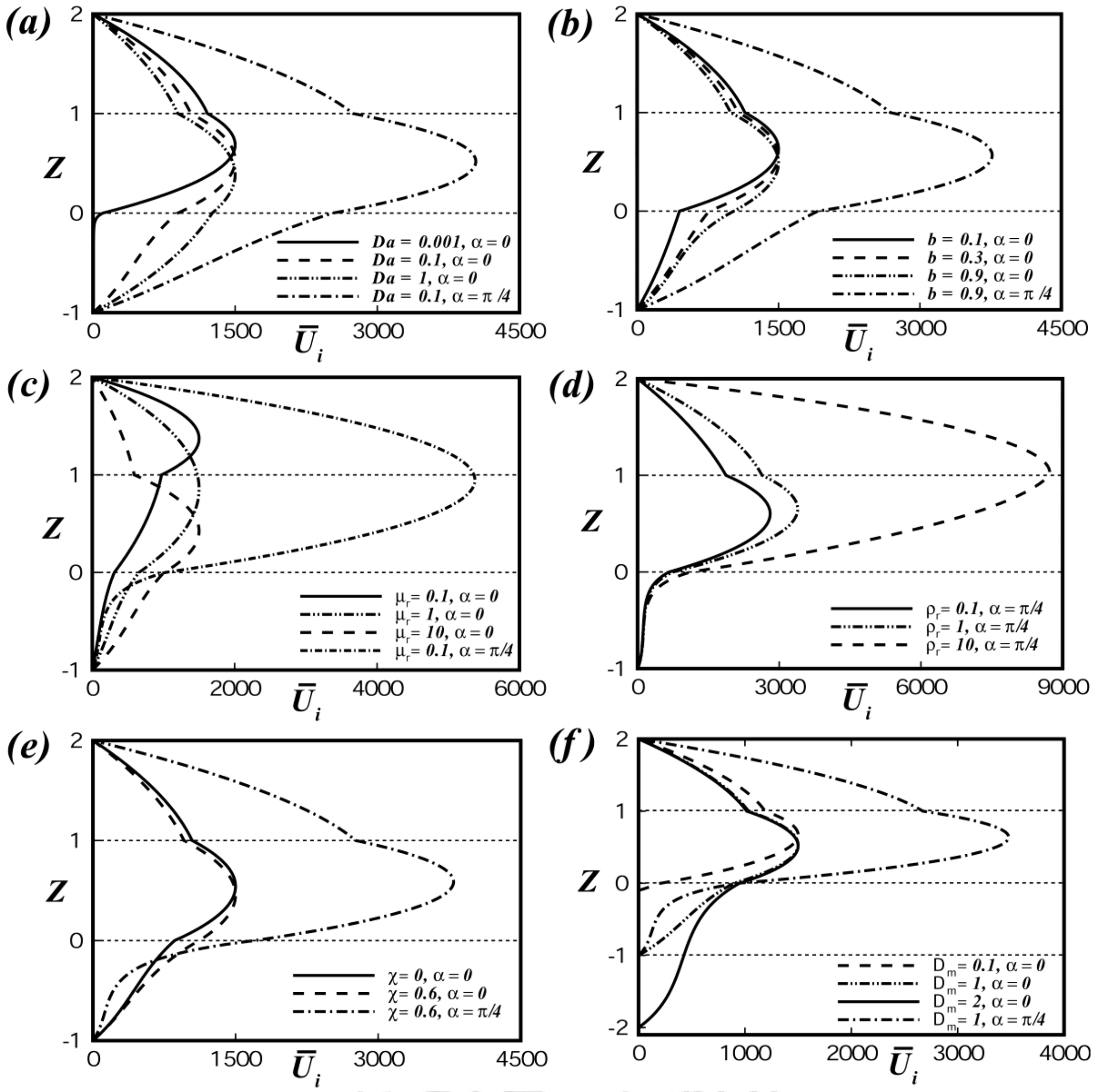

Figure 2.2: Plots (a) – (f) show the dimensionless base state velocity ($\bar{U}_i$) profiles across the channel (Z) when h_r = 1 and G = 9800. The curves in plot (a) – (f) corresponds to different Da, b, μ_r , ρ_r , χ and D_m respectively, the other parameters kept fixed at Da = 0.1, b = 0.5, μ_r = 4, ρ_r = 1, χ = 0.1, and D_m = 1; The porous media parameters and α necessary for the plots are provided in the insets.

The global constraint that the volumetric flow rate Q in the channels is,

$$Q = \int_{-D_m}^{0} \bar{U}_m + \int_{0}^{1} \bar{U}_1 + \int_{1}^{B} \bar{U}_2 \,. \tag{2.38}$$

For a confined flow the base state pressure (P_0) is obtained from the volumetric flow rate (Q). Here $\bar{U}_1$, $\bar{U}_2$, and $\bar{U}_m$ represent the base state velocities at the lower, upper, and porous layers, respectively, and $M = \sqrt{b/Da}$. The constants C_{ij} ($i = 1, 2$ and m; $j = 1, 2,$ and 3) in the expressions (35) – (37) are determined from the base state governing equations and boundary conditions as presented in the Appendix A. Figure 2.2 shows the typical base state velocity profiles under varied conditions. Since the influences of the thickness, viscosity, and density ratios on the base state flows of two-layer PPF and Couette flow are already studied in detail,[23] we focus mainly on the influence of the porous-media parameters in a two-layer PPFPM. It may be noted here that for the non-inclined cases in Figure 2.2, the flow rate is kept constant and properties of the porous layer are varied to show the change in the flow profile with the properties of the porous medium. For the inclined cases, the flow rates are modified as the angle of inclination is changed. Plot (a) shows that the velocity profile of a PPFPM with an impermeable porous layer (low *Da*, solid line) resembles PPF. As the permeability is increased (increasing *Da*), the less viscous lower layer ($\mu_r > 1$) undergoes strong slippage at the porous-liquid interface (broken lines). Consequently, the reduced frictional influence at the lower layer shifts the location of maximum velocity. Further, for the inclined case ($\alpha = \pi/4$), a larger flow rate is observed because of the gravity. Similar to permeability, the increased porosity (b) of the porous medium also imparts strong slippage to a less viscous lower layer, which in turn reduces the frictional influence at the lower layer, as shown in plot (b). These plots infer that in a PPFPM increase in porosity and permeability accelerates the overall flow in the liquid layers by inducing slippage at the liquid-porous media interface. Plot (c) shows that when the lower layer is more viscous, the additional frictional influence reduces the effect of slippage at the porous-liquid interface. The figure also shows that with the change in μ_r , the location of the maximum velocity can shift from one liquid layer to the other. Plot (d) shows that for the inclined case, the density ratio of the films (ρ_r) also significantly influences the base state flow because of the varied gravitational influences at the liquid layers. Plots (e) and (f) show that with increase in the stress jump coefficient (χ) at the porous-liquid interface and thickness of the porous layer (D_m) can also change the flow pattern by shifting the location of the maximum velocity. The velocity profiles shown in Figure 2.2 clearly indicate that the introduction of a porous layer underneath a two-layer PPF can significantly alter flow physics by changing the force distribution across the liquid layers.

2.4 LINEAR STABILITY ANALYSIS

The non-dimensional governing equations (2.14) – (2.22) and the boundary conditions (2.23) – (2.33) are linearized by imposing small perturbations to the base state, $U_j = \bar{U}_j + U'_j$, $W_j = W'_j$, and $P_j = \bar{P}_j + P'_j$, where j = *1*, *2*, and *m*. The over-bars indicate the base state and the primes denote perturbed quantities. The equations for velocity perturbations are then transformed in terms of the stream functions as, $U'_j = \partial\Psi_j / \partial Z$ and $W'_j = -\partial\Psi_j / \partial X$. The resulting expressions are then linearized employing normal modes, $\Psi_j(X,Z,T) = \tilde{\Psi}_j(Z)e^{iK(X-CT)}$, $P'_j(X,Z,T) = \tilde{P}_j(Z)e^{iK(X-CT)}$, $H(X,Z,T) = 1 + \tilde{H}e^{iK(X-CT)}$, to obtain the following dimensionless coupled O-S equations for the lower layer, upper layer, and the porous medium,

$$\left(D^2-K^2\right)^2\tilde{\Psi}_1=\mathbf{i}K\left[\left(\bar{U}_1-C\right)\left(D^2-K^2\right)-D^2\bar{U}_1\right]\tilde{\Psi}_1, \tag{2.39}$$

$$\nu_r\left(D^2-K^2\right)^2\tilde{\Psi}_2=\mathbf{i}K\left[\left(\bar{U}_2-C\right)\left(D^2-K^2\right)-D^2\bar{U}_2\right]\tilde{\Psi}_2, \tag{2.40}$$

$$\left(D^2-K^2\right)^2\tilde{\Psi}_m=\left(b/Da-\mathbf{i}KC\right)\left(D^2-K^2\right)\tilde{\Psi}_m. \tag{2.41}$$

In this formulation, the notation D and subscript Z represent the differentiation d/dZ, $\nu_r\left(=\mu_r/\rho_r\right)$, and K is the wavenumber, $C\ (=C_r+\mathbf{i}C_i)$ is the phase speed where C_r and KC_i are the wave speed and the growth rate of the perturbation. Here C_r and C_i are the real and imaginary parts of the wave speed, respectively. The linearized non-dimensional boundary conditions at the porous-solid and liquid-solid boundaries are,

$$\tilde{\Psi}_{mZ}(-D_m)\ =\ \tilde{\Psi}_m(-D_m)=\ \tilde{\Psi}_{2Z}(B)\ =\ \tilde{\Psi}_2(B)=0. \tag{2.42}$$

At the porous-liquid interface (Z = 0),

$$\tilde{\Psi}_1=\tilde{\Psi}_m, \tag{2.43}$$

$$\tilde{\Psi}_{1Z}=\tilde{\Psi}_{mZ}, \tag{2.44}$$

$$\frac{1}{b}\tilde{\Psi}_{mZZ}-\tilde{\Psi}_{1ZZ}=\frac{\chi}{\sqrt{Da}}\tilde{\Psi}_{mZ}, \tag{2.45}$$

$$\begin{aligned}&iK\bar{U}_{1Z}\tilde{\Psi}_1+\left[-3K^2+iK\left(C-\bar{U}_1\right)\right]\tilde{\Psi}_{1Z}+\tilde{\Psi}_{1ZZZ}=\\&\frac{1}{b}\left[-3K^2-\frac{b}{Da}+iKC\right]\tilde{\Psi}_{mZ}+\frac{1}{b}\tilde{\Psi}_{mZZZ}.\end{aligned} \tag{2.46}$$

At the liquid-liquid interface (Z = 1),

$$\tilde{H}=\tilde{\Psi}_1/\left(C-\bar{U}_1\right), \tag{2.47}$$

$$\tilde{\Psi}_1=\tilde{\Psi}_2, \tag{2.48}$$

$$\left(\tilde{\Psi}_{1Z}-\tilde{\Psi}_{2Z}\right)+\left[\tilde{\Psi}_1/\left(C-\bar{U}_1\right)\right]\left(\bar{U}_{1Z}-\bar{U}_{2Z}\right)=0, \tag{2.49}$$

$$\begin{bmatrix} \tilde{\Psi}_{1ZZZ} - 3K^2\tilde{\Psi}_{1Z} - \mu_r\tilde{\Psi}_{2ZZZ} + iK\left(C-\bar{U}_1\right)\left(\tilde{\Psi}_{1Z} - \rho_r\tilde{\Psi}_{2Z}\right) \\ +iK\left(\bar{U}_{1Z}\tilde{\Psi}_1 - \rho_r\bar{U}_{2Z}\tilde{\Psi}_2\right) + 3\mu_r K^2\tilde{\Psi}_{2Z} \\ -\tilde{\Psi}_1/\left(C-\bar{U}_1\right)\left[\left(G\left(\rho_r-1\right)\sin\alpha + C_{12} - \mu_r C_{22}\right)2K^2 + i\Gamma K^3\right] \end{bmatrix} = 0\,, \qquad (2.50)$$

$$\left[\tilde{\Psi}_{1ZZ} + K^2\tilde{\Psi}_1\right] + \left(\bar{U}_{1ZZ} - \mu_r\bar{U}_{2ZZ}\right)\tilde{\Psi}_1/\left(C-\bar{U}_1\right) - \mu_r\left[\tilde{\Psi}_{2ZZ} + K^2\tilde{\Psi}_2\right] = 0\,. \qquad (2.51)$$

It may be noted here that for the case of different densities in the two layers there is a hydrostatic force, restoring or destabilizing, when the interface is perturbed. However, this is independent of whether a base velocity field exits or not. Such a hydrostatic term is proportional to gravity and so is absorbed in G and the resulting calculations are presented.

2.5 NUMERICAL ANALYSIS

The coupled O-S system in the Eqs. (2.39) – (2.51) is an eigenvalue problem and is solved numerically to obtain the linear growth rate (KC_i) and the corresponding wavenumber (K) for the unstable modes. In this study, the most accurate D^2 algorithm proposed by Dongarra, et al.,[93] for Chebyshev-tau QZ spectral method is employed to obtain the eigenvalues.[21,94] For this purpose, initially the computational domain is mapped into $(-1, 1)$ for each layer by employing the transformations, $Z_1 = -2Z + 1$, $Z_2 = (2/B-1)Z - (B+1/B-1)$ and $Z_m = (2/D_m)Z + 1$, for the lower, upper, and the porous layer equations, respectively. Thereafter, introducing the variables, $\eta(Z_1) = \tilde{\Psi}_1(Z)$, $\sigma(Z_2) = \tilde{\Psi}_2(Z)$, and $\zeta(Z_m) = \tilde{\Psi}_m(Z)$, the 4th order ODEs (2.39) – (2.41) are transformed into a set of 2nd order ODEs in terms of the variables ξ, λ, and ϑ, employing the differential operators $L_1\eta \equiv \left(4d^2/dZ_1^{\,2} - K^2\right)\eta = \xi$, $L_2\sigma \equiv \left(\left(4/(B-1)^2\right)d^2/dZ_2^{\,2} - K^2\right)\sigma = \lambda$, and $L_m\zeta \equiv \left(\left(4/D^2\right)d^2/dZ_m^{\,2} - K^2\right)\zeta = \vartheta$,

$$L_1\eta - \xi = 0\,, \tag{2.52}$$

$$L_1\xi - iK\bar{U}_1\xi + 2iKC_{11}\eta + iKC\xi = 0\,, \tag{2.53}$$

$$L_2\sigma - \lambda = 0\,, \tag{2.54}$$

$$v_r L_2\lambda - iK\bar{U}_2\lambda + 2iKC_{21}\sigma + iKC\lambda = 0\,, \tag{2.55}$$

$$L_m\zeta - \vartheta = 0\,, \tag{2.56}$$

$$L_m\vartheta - \frac{b}{Da}\vartheta + iKC\vartheta = 0\,. \tag{2.57}$$

The boundary conditions at the porous-solid and liquid-solid boundaries are derived in terms of the transformed variables as,

$$\zeta_{Z_m}(-1) = \zeta(-1) = \sigma_{Z_2}(1) = \sigma(1) = 0. \tag{2.58}$$

The transformed boundary conditions at the porous-liquid interface are,

$$\eta - \zeta = 0\,, \tag{2.59}$$

$$\eta_{Z_1} + \frac{1}{D}\zeta_{Z_m} = 0\,, \tag{2.60}$$

$$K^2\eta + \xi - \frac{K^2}{b}\zeta + \frac{2\chi}{D\sqrt{D_a}}\zeta_{Z_m} - \frac{1}{b}\vartheta = 0\,, \tag{2.61}$$

$$\begin{bmatrix} iKC_{12}\eta + 2\left(2K^2 + iK\bar{U}_1\right)\eta_{Z_1} - 2\xi_{Z_1} + \dfrac{2}{bD}\left[2K^2 + \dfrac{b}{Da}\right]\zeta_{Z_m} \\ -\dfrac{2}{bD}\vartheta_{Z_m} - C\left(2iK\eta_{Z_1} + \dfrac{2iK}{bD}\zeta_{Z_m}\right) \end{bmatrix} = 0\,. \tag{2.62}$$

The transformed boundary conditions at the liquid-liquid interface are,

$$\eta - \sigma = 0\,, \tag{2.63}$$

$$\begin{bmatrix} C\left(2\eta_{Z_1} + (2/B - 1)\sigma_{Z_2}\right) - \left((2C_{11} + C_{12}) - (2C_{21} + C_{22})\right)\eta \\ -2\bar{U}_1\eta_{Z_1} - \left(2\bar{U}_1/B - 1\right)\sigma_{Z_2} \end{bmatrix} = 0\,, \tag{2.64}$$

$$\begin{bmatrix} C\left(2K^2\eta+\xi-2\mu_r K^2\sigma-\mu_r\lambda\right)+2\left(\left(C_{11}-\mu_r C_{21}\right)-\bar{U}_1 K^2\right)\eta \\ -\bar{U}_1\xi+2\mu_r\bar{U}_1 K^2\sigma+\mu_r\bar{U}_1\lambda \end{bmatrix}=0, \tag{2.65}$$

$$\begin{gathered} C^2\left(2iK\eta_{Z_1}+\left(2iK\rho_r/B-1\right)\sigma_{Z_2}\right)+ \\ C\begin{pmatrix} -iK\left(2C_{11}+C_{12}\right)\eta-4\left(iK\bar{U}_1+K^2\right)\eta_{Z_1}+2\xi_{Z_1}+iK\rho_r\left(2C_{21}+C_{22}\right)\sigma \\ -\left(4/B-1\right)\left(\mu_r K^2+iK\rho_r\bar{U}_1\right)\sigma_{Z_2}+\left(2\mu_r/\left(B-1\right)\right)\lambda_{Z_2} \end{pmatrix} . \\ +\begin{bmatrix} \left[2\left(\left(2C_{11}+C_{12}\right)-\mu_r\left(2C_{21}+C_{22}\right)\right)K^2+iK\bar{U}_1\left(2C_{11}+C_{12}\right)+i\Gamma K^3\right]\eta \\ +2\left(2\bar{U}_1 K^2+iK\bar{U}_1^{\,2}\right)\eta_{Z_1}-2\bar{U}_1\xi_{Z_1}-iK\bar{U}_1\rho_r\left(2C_{21}+C_{22}\right)\sigma \\ +\left(2/\left(B-1\right)\right)\left[2\mu_r\bar{U}_1 K^2+iK\rho_r\bar{U}_1^{\,2}\right]\sigma_{Z_2}-\left(2\mu_r\bar{U}_1/\left(B-1\right)\right)\lambda_{Z_2} \end{bmatrix}=0 \end{gathered} \tag{2.66}$$

The subscripts Z_1, Z_2, and Z_m in these equations denote ordinary differentiation. The transformed ODEs are then expanded in terms of Chebyshev polynomials $T_n(z)$. For N Chebyshev polynomials, the eigenvalues are obtained from a ($6N$+12) × ($6N$+12) matrix corresponding to six second order ODEs and twelve boundary conditions. The accuracy of the eigenvalues is tested by varying the number of polynomials and in the process the spurious eigenvalues are eliminated. For the sake of accuracy, the eigenvalues are also cross verified by solving the set of equations (2.39) – (2.51) employing spectral collocation method with enhanced accuracy as proposed by Weideman and Reddy.[95] The eigenvectors reported are obtained employing the spectral collocation method.

Figure 2.3 shows the linear growth rate (KC_i) vs. wavenumber (K) plot for a PPFPM where the circles (solid lines) correspond to the collocation (Chebyshev-tau QZ) method. Plot (a) shows the existence of the finite wavenumber shear mode when μ_r = 1 from both the numerical methods. The eigenvalues predicted from both the methods are in exact agreement. In plot (b), we show that both the methods are able to predict the coexistence of long-wave interfacial modes (curve 'i') and the finite-wavenumber shear flow mode (curve 's'). Again, the eigenvalues for both interfacial and shear modes match exactly.

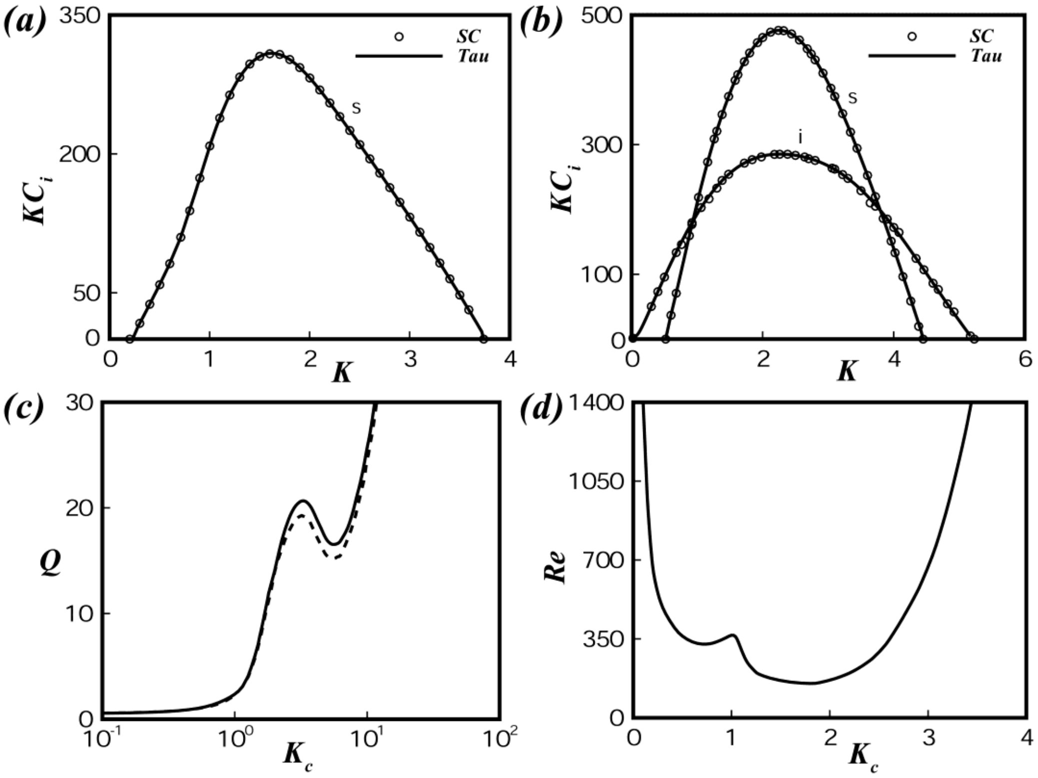

Figure 2.3: Plots (a) and (b) show the variation of growth rate (KC_i) with wavenumber (K). The circles (solid lines) correspond to the spectral collocation (Chebyshev-tau) method. The curves 'i' and 's' represent the interfacial and the shear modes. In the plots (a) and (b) μ_r = 1 and μ_r = 10, when ρ_r = 1, b = 0.9, D_m = 1, h_r = 1, χ = 0.1, Γ = 16000 (γ = 0.016 N/m) and Da = 0.01. Plot (c) shows the variation in the flow rate (Q) with the critical wavenumber (K_c). The solid line represents b = 0.01and D_m = 0.01, broken line represents b = 0.5 and D_m = 1. The other parameters for the plot (c) are ρ_r = 0.84, h_r = 0.66, χ = 0.0, Γ = 1.2, Da = 0.001, and G = 168. Plot (d) shows the variation in the Reynolds number (Re) with K_c when b = 0.78, D_m = 5, ρ_r = 0, μ_r = 0, χ = 0, Γ = 0, Da = 0.0175, and G = 0.

The interfacial modes have a long-wave characteristic, which means as $K \rightarrow 0$ the growth rate $KCi \rightarrow 0$. In contrast, the shear mode is identified as $KCi > 0$ in between a pair of finite wavenumbers K_1 & $K_2 \neq 0$. Further, the real part of the phase speed of the eigenvalue of the interfacial mode is equal to the base state velocity of the liquid-liquid interface. Thus, if two modes of instabilities are present at a particular wavenumber (K), we first obtained the eigenvalues in terms of the phase speed C having a real part (C_r) and imaginary part (C_i). The positive growth rate (KC_i) verses wavenumber (K) gives the information about the modes that are unstable whereas the magnitude of the real part (C_r) provides the information on the speed of the travelling mode.

The curves confirm that both the numerical methods are equally accurate in predicting the eigenvalues. However, the Chebyshev-tau QZ spectral method is employed for further discussions because of its known superiority in predicting the accurate eigenvalues over the collocation method. The accuracy of the Chebyshev-tau QZ spectral code is also validated against the available results in the literature. For example, the eigenvalues for the two-layer flow on a porous medium can asymptotically be reduced to the two-layer PPF confined by impervious substrates in the limit when the porous layer is very thin.

Table 2.1: The dimensionless parameters employed to generate the data are, $Da = 0.001$, $D_m = 0.1$, $b = 0.0005$, $\chi = 0.0$, $\mu_r = 0.01$, $\rho_r = 0.5$, Q = 2, $\Gamma = 5/(h_r+1)$, $K = 0.001/(h_r+1)$.

h_r	β	G	Tilley et al.[14]	Present work
2	0	1	0.25306349 + 0.00012602286 i	0.253086483328 + 0.00013200144 i
2	1	1	0.29693846 + 0.00012364057 i	0.296965762902 + 0.00012687577 i
2	1	10	0.69181321 + 0.00005630771 i	0.691879267549 + 0.00008853360 i
1/3	0	1	6.218724 + 0.001810619 i	6.218576184520 + 0.00183698835 i
1/3	1	1	6.118392 + 0.0017395518 i	6.118223044750 + 0.00175378532 i
1/3	1	10	5.215409 + 0.000966382 i	5.215044820371 + 0.00110899624 i

In Table 2.1, we show the eigenvalues obtained in that limit and compare them with the eigenvalues reported by Tilley, et al.,[14,15] for the PPF. The table shows that the eigenvalues predicted in this study are very close to the same obtained by Tilley, et al.,[14,15] In some of the cases we find the predictions from this analysis differ, which can be attributed to the presence of the very thin but finite porous layer underneath the two-layer flow. In Figure 2.3(c), the neutral stability plots obtained by Tilley, et al.,[14,15] is reproduced in the limit where the porous layer is almost impervious. The solid and the dotted line show the influence of porosity in such a situation. Figure 2.3(d) shows another asymptotic case where we reproduce the neutral stability diagram of the instability of a single layer confined between a rigid and a porous substrate, recently obtained by Hill and Straughan.[86] Figure 2.3 together with Table 2.1 corroborate the accuracy of the Chebyshev-tau QZ spectral code employed for this analysis.

2.6 RESULTS AND DISCUSSION

Previous studies[12] show that a pressure driven two-layer PPF can be unstable either because of the interfacial mode when $\mu_r > h_r^2$ or because of the shear mode when $\mu_r < h_r^2$ or can be neutrally stable when $\mu_r = h_r^2$, when the liquid layers have equal density. In order to highlight the influence of permeability, porosity, and thickness of the porous layer, the instabilities of the PPFPM are discussed around these conditions. It may be noted here that all the results are reported in terms of upper to lower viscosity (μ_r) and thickness (h_r) ratios. The typical magnitudes of the physical properties employed to generate the results are, ρ_j ~ 1000 kg/m^3, μ_j ~ 0.001− 0.01 Pa s, d_j ~ 0.0001 – 0.1 m, γ ~ 0.02 N/m, and x-directional velocity ~ 10^{-4} – 0.1 m/s.

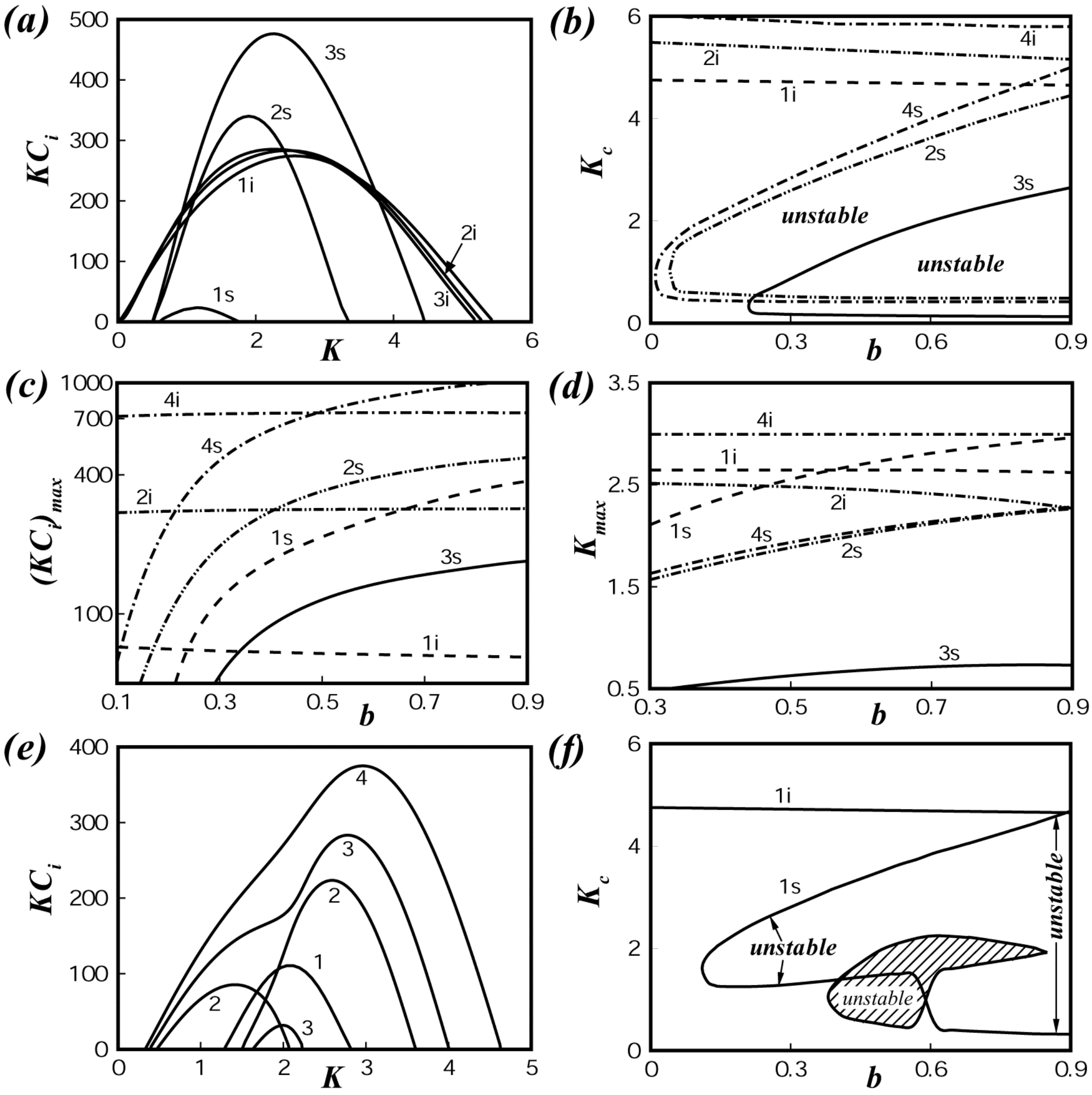

Figure 2.4: The plots show the influence of porosity (b). The curves 'i' and 's' represent the interfacial and shear modes. Plot (a) shows the variation of KC_i with K when $h_r = 1$. The curves (1) – (3) represents $b = 0.1$, 0.5, and 0.9, respectively. Plots (b) – (d) show the variations of K_c, $\left(KC_i\right)_{max}$, and K_{max} with b, respectively. The curves (1) – (3) represent $h_r = 0.1$, 1, and 10, respectively, and curve 4 represents $h_r = 1$ and $\alpha = \pi/4$. Plot (e) shows the variation of KC_i with K when $h_r = 0.1$ where curves (1) – (4) represents $b = 0.3$, 0.52, 0.66, and 0.9, respectively and $\alpha = 0$. Plot (f) shows the variation of K_c with b for same case shown in plot (e). The other parameters for the plots are $\mu_r = 10$, $\rho_r = 1$, $\chi = 0.1$, $D_m = 1$, $\alpha = 0$ and $Da = 0.01$.

The resulting parameter space ensures that the analysis is able to uncover both macroscopic and microscopic features of PPFPM. Base states volumetric flow rate (Q) and pressure (P_0) are correlated by the expression shown in the Appendix A22. To find these parameters, first we fix maximum velocity U_{max}, then calculate Q employing the Eq. 2.38 and then calculate the base state pressure P_0 from Eq. A22. The Reynolds number ($Re = u_{\max} \rho_1 h_0 / \mu_1$) based on the maximum velocity of the base flow of the non-inclined cases is fixed to 1500 for all the figures, unless and otherwise mentioned. The channel volumetric flow rate has a cumbersome relation with this Reynolds number, which is not provided with the text.

In the Figures 2.4, 2.6 – 2.10, the plot (a) shows the variation of the linear growth coefficient, KC_i, with the wavenumber, K. The dominant growth coefficient, $(KC_i)_{max}$, is obtained by identifying the global maxima of KC_i. Plots (b), (c), and (d) show the variations of the critical wavenumber, K_c, the dominant growth coefficient, $(KC_i)_{max}$, and the dominant wavenumber (K_{max}), respectively. The dominant wavenumber (K_{max}) corresponding to $(KC_i)_{max}$, is related to the dominant wavelength (Λ_{max}) by the relation, $K_{max} = 2\pi / \Lambda_{max}$. The critical wavenumber K_c corresponds to the neutral stability condition ($KC_i = 0$). The curves with the symbols ‘i’ (‘s’) represent the interfacial (shear) mode of instability.

2.6.1 Effect of porosity

Figures 2.4 – 2.6 summarize the influence of porosity (b) on the unstable modes. All the plots in Figure 2.4 correspond to a constant $\mu_r = 10$. Plot (a) shows when the condition $\mu_r > h_r^2$ is met and the porous layer is of very low porosity (b = 0.1) the PPFPM can be unstable because of a dominant interfacial mode (curve 1i). This observation for PPFPM is quite similar to PPF as previously shown by Yiantsios and Higgins.[12] The only difference to be seen for PPFPM is an additional subdominant shear mode of instability (curve 1s). Further, as b is increased (curves 2 and 3) the shear mode becomes the dominant mode of instability even when the condition $\mu_r > h_r^2$ is maintained. The base state velocity profiles in plot (b) indicate that increase in the porosity causes a stronger flow in porous medium, which in turn induces a strong slippage at the porous-liquid interface. The reduced frictional influence at the liquid layers due to this slippage causes the shear mode to gain dominance over the interfacial mode when the porous layer has higher porosity. Interestingly, the interfacial mode remains dormant to these influences because the destabilization due to the viscosity stratification does not magnify as the density, viscosity, and thickness ratios of the liquid layers are kept unaltered. The neutral stability plots in plots (b) and (f) show that the span of unstable wavenumbers corresponding to the interfacial mode (curve 1i and 2i) does not significantly vary with b whereas for the shear mode (curve 1s and 2s) the span of unstable wavenumbers increases especially in the large wavenumber (shorter wavelength) regime. Clearly, the reduced frictional influence destabilizes the modes with the shorter waves as b is increased.

The curves 1 and 2 in plot (c) show the transition points of the dominant mode of instability from the interfacial to shear mode with increase in b. The curves 1i and 1s confirm that for a PPFPM with $\mu_r > h_r^2$ and $h_r < 1$, the interfacial (shear) mode is dominant (sub-dominant) mode of instability at the smaller values of b. Beyond a threshold b, the shear mode starts dominating with reducing viscous resistance at the lower layer. The curves 2i and 2s show that when $h_r = 1$ and $\mu_r > h_r^2$, the transition from dominant interfacial to dominant shear mode takes place at a higher value of *b*. In this case, stronger viscous resistance in a relatively thinner lower layer enforces the frictional influence to adequately reduce at a higher porosity. Interestingly, when the condition $\mu_r < h_r^2$ is met the interfacial mode vanishes and only the unstable shear mode is present (curve 3s) as it happens in case of PPF. The curves 4i and 4s show that the gravitational influence in the inclined case can lead to a stronger interfacial and shear flow instabilities in PPFPM. A comparison between the curves 2 and 4 concludes that as the interfacial-mode grows stronger for the inclined case the transition from dominant interfacial to dominant shear mode is further delayed. Plot (d) shows that with increase in *b*, Λ_{max} for the shear mode shifts towards shorter wavelength (larger K_{max}) regime. The figure also shows that Λ_{max} corresponding to the interfacial mode either remains constant (curve 1i) or shifts to the longer wavelength regime (curve 2i) because of the extra slippage encountered at the porous-liquid interface with the increase in *b*. The curve 4 in the plots (b) – (d) show that for the inclined PPFPM, the additional gravity driven flow fuels up the strengths of both the modes. As compared to the non-inclined case, for the inclined case the wavelength of the interfacial mode (curves 2i and 4i) is more influenced by the gravity driven flow as compared to the shear mode (curves 2s and 4s) and shifts towards shorter wavelength regime due to larger destabilizing influence.

The plots (e) and (f) show a special case where we observe multiple shear modes. Curve 1 in plot (e) displays a single shear mode at a lower *b*. At a little higher value of *b*, the pair of curves marked 2 signify the presence of twin shear modes with one of them being dominant. With further increase in *b*, these two modes merge to form a stronger shear mode in addition to the emergence of a subdominant shear mode as shown by the pair of curves marked 3. At very high porosity the subdominant shear mode vanishes whereas the dominant shear mode gains further strength as shown by the curve 4. The neutral stability plots corresponding to these twin-modes are shown in the plot (f). The hatched unstable zone depicts the weaker shear mode that appears beyond threshold porosity and then vanishes later whereas the non-hatched neutral stability plot represents the dominant shear mode. The plots clearly depict that at lower values of *b*, the flow is only unstable by a single shear mode. However, beyond a threshold value of *b*, twin modes are observed in which the new mode belongs to rather longer wavelength regime. Further, at higher values of *b* (~ 0.6), the dominant shear mode undergoes an abrupt increase in the span of unstable wavenumbers (non-hatched region) and the subdominant shear mode undergoes a rapid shrinkage in the unstable span of wavenumbers (hatched region), as previously predicted in the plot (e). The latter vanishes with increasing *b* in plot (f), as found previously in the plot (e). Interestingly, similar to the observation reported here for PPFPM, the twin shear modes are also found to exist for a single layer flow over a porous medium.[83-85]

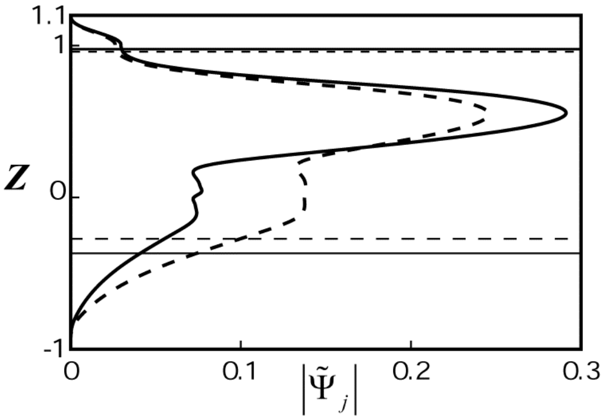

Figure 2.5: Eigenfunction plots for the stronger (solid line) and weaker (broken line) shear modes when $K = 2$, $b = 0.6$, $h_r = 0.1$, $\mu_r = 10$, $\rho_r = 1$, $\chi = 0.1$, $D_m = 1$, $\alpha = 0$ and $Da = 0.01$.

We further investigate the origin of the twin modes from the eigenfuctions related to the eigenvalues. In Figure 2.5, we show the absolute values of the perturbed streamfunction ($\left|\tilde{\Psi}_j\right|$) corresponding to the eigenvalues obtained for both the shear modes. Interestingly, the critical layers ($U = C_r$) are found to be situated either in the lower layer or in the porous layer.

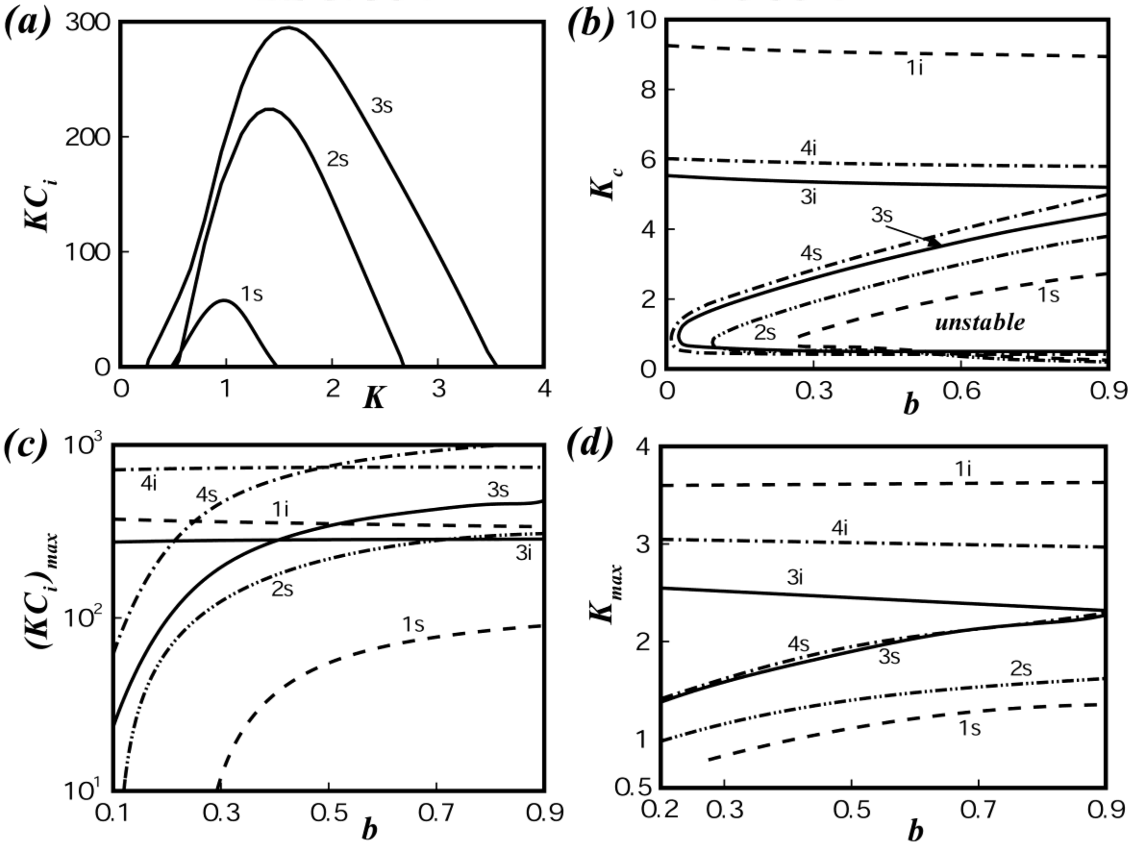

Figure 2.6: The plots show the influence of porosity (b). Plot (a) shows the variation of KC_i with K when μ_r = 1, curves (1) – (3) represent b = 0.1, 0.5, and 0.9, respectively. Plots (b) – (d) show the variations of K_c, $\left(KC_i\right)_{max}$, and K_{max} with b, respectively. The curves (1) – (3) represent μ_r = 0.1, 1, and 10, respectively, and curve 4 represents μ_r = 10 and $\alpha = \pi/4$. The other parameters for the plots are ρ_r = 1, h_r = 1, χ = 0.1, D_m = 1, and Da = 0.01.

For the stronger mode (solid line) a sharp variation in $|\tilde{\Psi}_j|$ is observed ear liquid-liquid interface but at the lower layer. Near the other critical layer in the porous medium the variation in $|\tilde{\Psi}_j|$ is not that significant. In comparison, for the weaker shear mode (broken line) a couple of sharp variations in $|\tilde{\Psi}_j|$ takes place near the critical layers at the lower liquid layer as well as at the porous layer.

In Figure 2.6, h_r is fixed to a constant value and the variation with b at different μ_r is studied. Plot (a) shows that beyond a threshold value of b the PPFPM can develop shear mode of instability even when the condition $\mu_r = h_r^2$ is met where PPF is found to show neutral stability.[12] Again, the reduced frictional influence at the liquid layers due to the presence of the porous medium plays a decisive role in fuelling up the shear mode. The curves (1) – (3) in the plots (b) – (d) highlight the presence of either a dominant or a subdominant shear mode for all combinations of h_r and μ_r. The curves also show that except for the condition $\mu_r = h_r^2$, the interfacial mode can be present for any other combination of h_r and μ_r. The curves 1i and 1s in plot (c) show that when $\mu_r < h_r^2$ the interfacial mode is always the dominant mode of instability in presence of a subdominant shear mode of instability for all values of b. The curve 2s in this plot show that when $\mu_r = h_r^2$ only the shear mode can destabilize the system, as previously observed in plot (a). The curves 3i and 3s show that when $\mu_r > h_r^2$, at lower values of b the interfacial (shear) mode is the dominant (subdominant) mode whereas at higher values of b the shear (interface) mode becomes the dominant (subdominant) mode. The curves 4i and 4s show that the gravitational influence imparts strengths to both the modes and pushes the wavelength of the interfacial mode towards shorter wavelength regime.

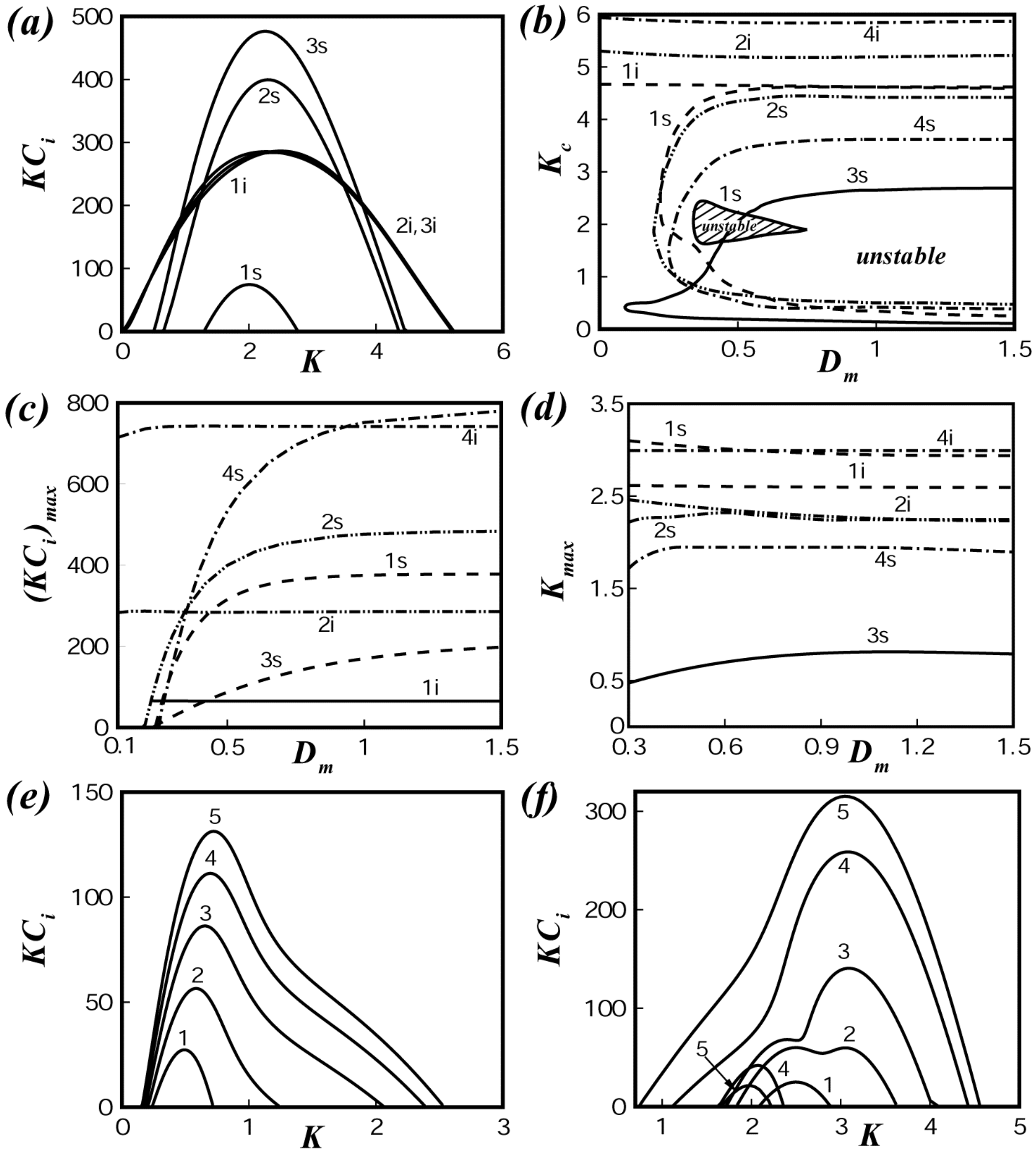

Figure 2.7: The plots show the influence of porous medium thickness (D_m). Plots (a), (c), and (d) show the variation of KC_i with K. plot (a) show when h_r = 1, the curves (1) – (3) represent D_m = 0.225, 0.5, and 1, respectively. Plots (b), (c), and (d) show the variations of K_c, $(KC_i)_{max}$, and K_{max} with D_m, respectively. The curves (1) – (3) represent h_r = 0.1, 1, and 10, respectively, and curve 4 represent h_r = 1 and $\alpha = \pi/4$. The curves (1) – (5) in plot (e) represent D_m = 0.3, 0.4, 0.5, 0.6, and 0.7, respectively, when h_r = 10. The curves (1) – (5) in plot (f) represent D_m = 0.22, 0.26, 0.3, 0.4, and 0.5, respectively, when h_r = 1.1. The other parameters for the plots are μ_r = 10, ρ_r = 1, b = 0.5, χ = 0.1, and Da = 0.01.

Concisely, the Figures 2.4 – 2.6 together highlight a number of key instability features of PPFPM that are in general not observed for the PPF.

2.6.2 Effect of porous layer thickness

Figures 2.7 and 2.8 summarize the influence of the porous layer thickness (D_m) on the unstable modes. Figure 2.7 shows the influence of D_m at different h_r at a constant μ_r. Plot (a) shows that when $h_r = 1$ and $\mu_r > h_r^2$, unlike PPF, both the interfacial and shear modes coexist in a PPFPM and with the increase in D_m shear mode emerges stronger (curves 1s – 3s) whereas the growth rate of the interfacial mode remains almost the same (curves 1i – 3i).

Increase in thickness allows for more flow inside the porous layer, which in turn allows the lower layer to slip on the porous media more strongly. A weaker frictional resistance at the lower layer due to this can be expected in the less viscous lower layer over a thicker porous layer. Plot (b) shows that the shear mode of instability is present for all conditions beyond a critical value D_m whereas the interfacial mode makes appearance only when $\mu_r > h_r^2$. The unusual shapes of the curves 1s and 3s in this plot can be explained from the plots (e) and (f). The curves 1 – 5 in plot (e) show that only a small span of wavenumbers is unstable under the shear mode at low D_m. However, beyond a threshold value of D_m, the span of unstable wavenumbers increased rapidly which leads to the sudden expansion in the curve 3s in plot (b). At larger values of D_m, the span of unstable wavenumbers saturates. Plot (f) shows another interesting situation, where with increase in the D_m, again the twin shear modes makes appearance. The hatched region in the neutral stability plot (b) for the curve 1s shows the region of existence of this extra mode at moderate values of D_m. Plot (f) shows the existence of only one shear mode at low D_m

(curve 1) and with increase in D_m the dispersion curve becomes bimodal (curve 2). Further with increase in D_m, as the shear mode becomes stronger (curve 3), a subdominant shear mode appears (curves marked 4), which diminish as D_m is increased further (curves marked 5).

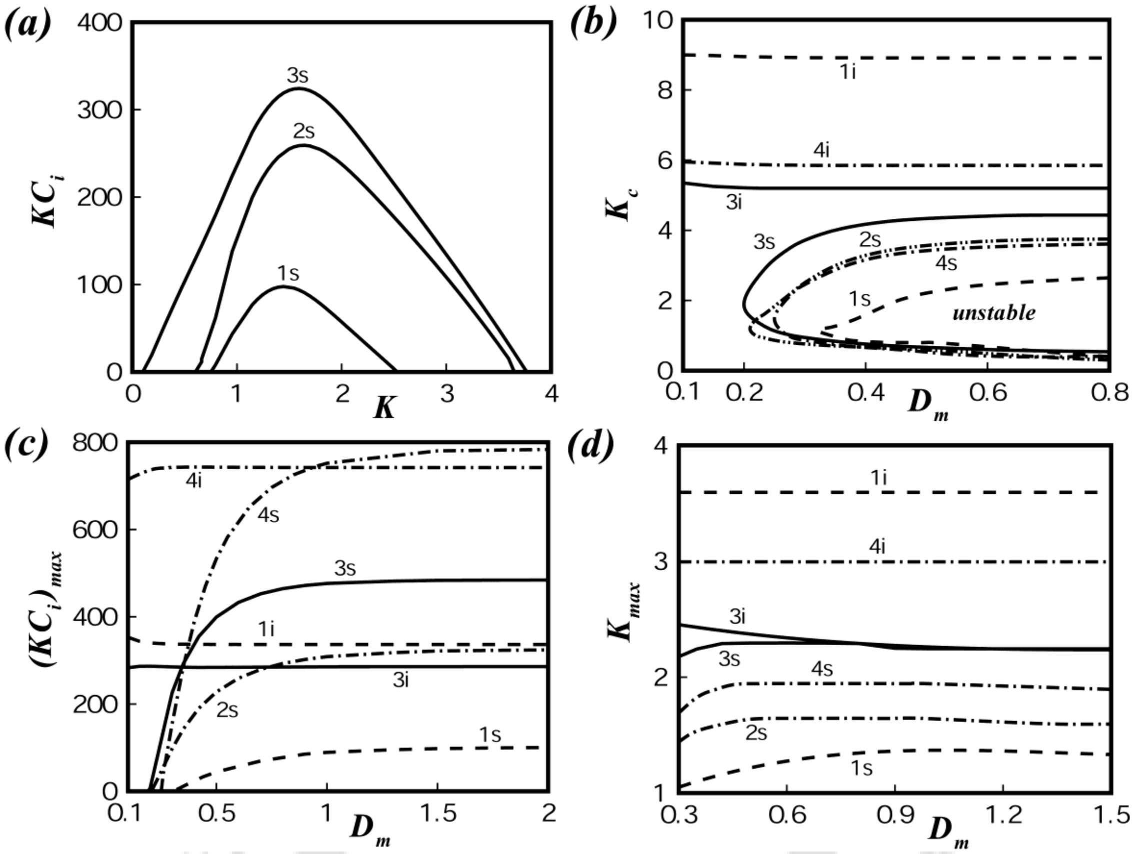

Figure 2.8: The plots show the influence of porous medium thickness (D_m). Plot (a) shows the variation of KC_i with K when μ_r = 1, curves (1) – (3) represent D_m = 0.3, 0.6, and 2, respectively. Plots (b) – (d) show the variations of K_c, $(KC_i)_{max}$, and K_{max} with D_m, respectively. The curves (1) – (3) represent μ_r = 0.1, 1, and 10, respectively, and curve 4 represent μ_r =10 and $\alpha = \pi/4$. The other parameters chosen for the plots are ρ_r = 1, h_r = 1, b = 0.5, χ = 0.1, and Da = 0.01.

At larger values of D_m, the span of unstable wavenumbers saturates with a single shear mode. The curves 1 and 2 in plot (c) shows that when D_m is small, the interfacial (shear) mode is the dominant (sub-dominant) mode for $\mu_r > h_r^2$. However, with progressive increase in the porous layer thickness, beyond a threshold value of D_m the shear mode becomes the dominant mode of instability. The curve 3s shows that when $\mu_r < h_r^2$, the shear mode is the only existing mode beyond a critical value of D_m. In comparison, the shear mode gains strength very rapidly when D_m is small. However, beyond a threshold value of D_m, the shear mode also stops growing as the growth rate saturates to a constant value. The plots confirm that for two-layer PPFPM the growth rate and the wavelength of the shear mode can change until a critical thickness of the porous layer. growth of the inertia driven instabilities are influenced until a critical value of the porous layer thickness as identified previously.[82] The curve 4 in the plots (b) to (d) confirms that for the non-inclined case although the nature of instability remains same, the gravitational influence reduces the time and length scales significantly. Interestingly, this behavior is similar to the single layer PPF over a porous layer where

Figure 2.8 depicts the variations with D_m at different μ_r at a fixed h_r. This figure shows another interesting scenario where the PPFPM is unstable under the condition $\mu_r = h_r^2$ when D_m is varied. The curves 1 and 3 in the plots (b) – (d) show that both interfacial and shear modes of instabilities can be present for the conditions $\mu_r > h_r^2$ and $\mu_r < h_r^2$ whereas the curve 2 suggests that the shear mode can exists even when $\mu_r = h_r^2$. The curves confirm that in a PPFPM, the shear mode can be present under all conditions beyond a critical thickness of the porous medium. The curve 4 in the plots (b) – (d) show that the gravity driven PPFPM shows similar features as observed for the non-inclined case. However, the time scales of the instabilities are found to be much faster and the length scales are relatively smaller for the inclined case. Figures 2.7 and 2.8 together highlight that the instability features of a two-layer PPFPM can be significantly different from the two-layer PPF when the porous layer thickness is varied.

2.6.3 Effect of permeability

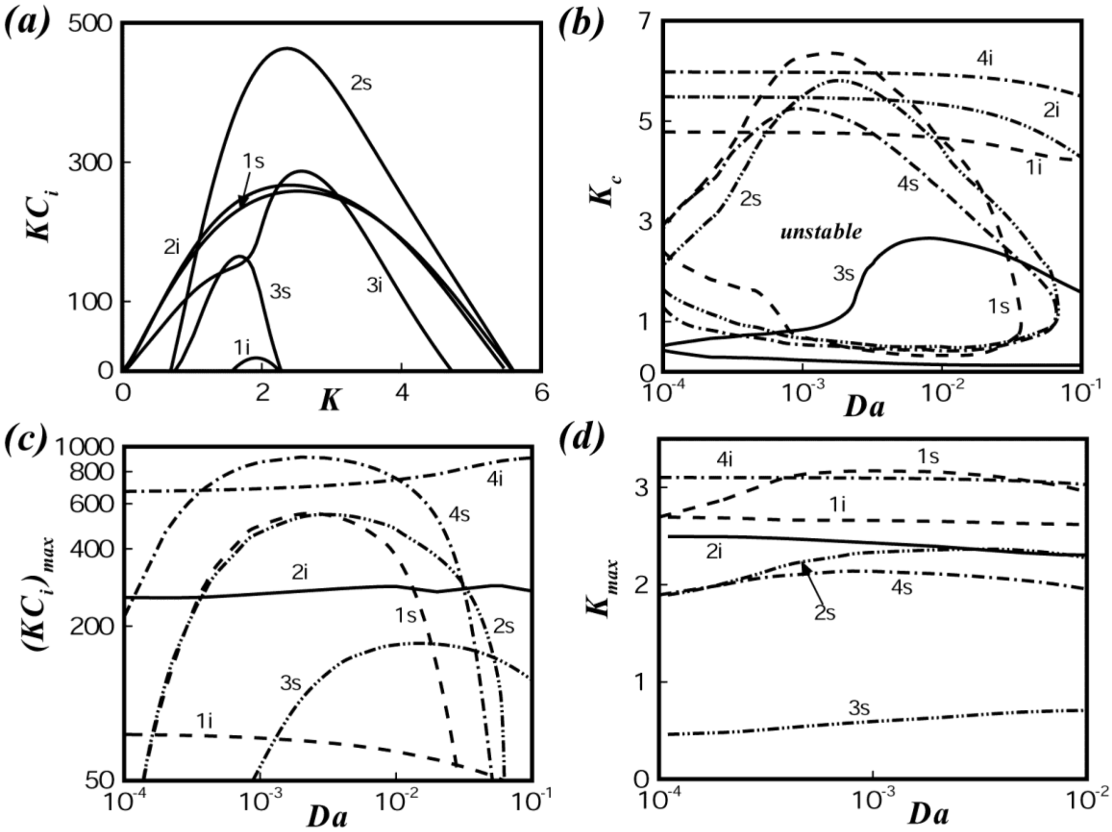

Figure 2.9: The plots show the influence of Darcy Number (*Da*). Plot (a) shows the variation of KC_i with K when h_r = 1. The curves (1) – (3) represent *Da* = 0.00011, 0.001, and 0.05, respectively. Plots (b) – (d) show the variations of K_c, $\left(KC_i\right)_{max}$, and K_{max} with *Da*, respectively. The curves (1) – (3) in the plots represent h_r = 0.1, 1, and 10, respectively, and curve 4 represent h_r = 1 and $\alpha = \pi/4$. The other parameters for the plots are μ_r = 10, ρ_r = 1, b = 0.5, χ = 0.1, and D_m = 1.

Figure 2.9 summarizes the influence of the permeability of the porous layer (*Da*). In Figure 2.9, the influence of *Da* is shown at different h_r at a constant μ_r. It may be noted here that a fully permeable porous medium ($b \rightarrow 1$, $Da \rightarrow \infty$) is the same as a liquid layer, as the Brinkman correction terms drop out from the equations of motion (2.21) and (2.22), and the boundary condition (2.27). Thus, if the pressure drop across the PPFPM is kept constant, at lower permeability, the porous medium may reduce the frictional influence on the liquid films because of larger slippage at the porous-liquid interface. However, at higher permeability it may also reduce the overall flow rate inside the PPFPM by channelizing more liquid into the porous layer, which can reduce the inertial influence inside the liquid films. Curves 1i and 1s in plot (a) show that at very low *Da* the interfacial (shear) mode is dominant (subdominant). Curves 2i and 2s show that, with increase in *Da*, the shear (interfacial) mode becomes the dominant (subdominant) one as the frictional influence at the lower layer reduces. Curves 3i and 3s show with further increase in *Da*, the shear (interfacial) mode again becomes the subdominant (dominant) as the inertial influence reduces with increase in the permeability. Plot (b) show that the span of unstable wavenumbers marginally reduces with *Da* for interfacial mode (curves 1i and 2i) whereas the same initially increases and then diminishes for the shear mode (curves 1s – 3s). The sudden expansions in the plots 1s and 3s again highlight the zones where the slippage due to the porous medium picks up, as discussed previously for the other cases. Plot (c) shows that $\left(KC_i\right)_{max}$ corresponding to the interfacial mode does not change much, whereas $\left(KC_i\right)_{max}$ corresponding to the shear mode initially increases, then reaches a maximum value, and thereafter reduces with *Da*. The variation of the $\left(KC_i\right)_{max}$ corresponding to the shear mode is a clear signature of the variation in the inertial force inside the two-layer PPFPM with *Da*. Plot (d) shows that Λ_{max} also passes through a minimum with increase in *Da* for the shear mode whereas Λ_{max} reduces marginally with *Da* for the interfacial mode. The plots (b) – (d) also confirm that the shear mode is present up to a critical value of *Da* for the conditions μ_r and h_r^2 whereas the interfacial mode is observed only when $\mu_r > h_r^2$. The curves 4i and 4s show that the inclined case also show similar nature as observed for the non-inclined case. However, as previously observed for the porosity and the thickness of the porous layer, the time scale for the inclined case is found to be much smaller than the same in the non-inclined case when *Da* is varied.

2.6.4 Effect of stress jump coefficient

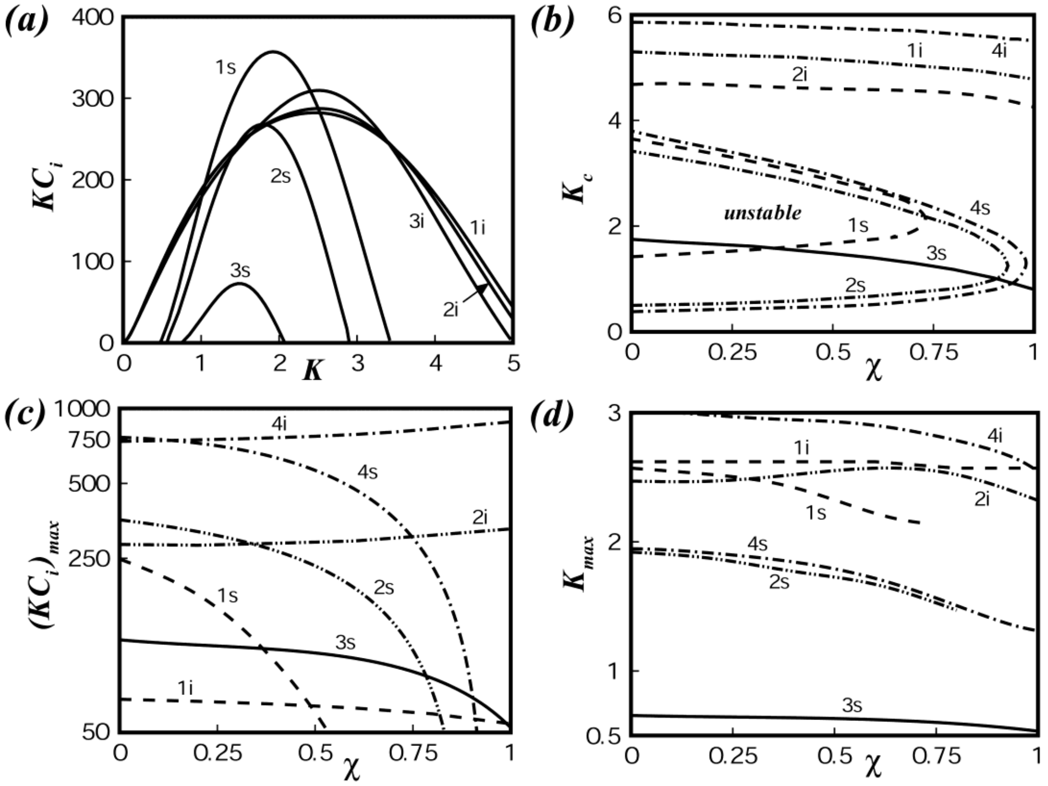

Figure 2.10: The plots show the influence of stress jump coefficient (χ). Plot (a) shows the variation of KC_i with K when h_r = 1. The curves (1) – (3) represent χ = 0, 0.4, and 0.8, respectively. Plots (b) – (d) show the variations of K_c, $(KC_i)_{max}$, and K_{max} with χ, respectively. The curves (1) – (3) in the plots represent h_r = 0.1, 1, and 10, respectively, and curve 4 represent h_r = 1 and α = π/4. The other parameters for the plots are μ_r = 10, ρ_r = 1, b = 0.5, χ = 0.1, D_m = 1, and Da = 0.01.

Figure 2.10 shows the influence of the dimensionless stress jump coefficient (χ) at the porous-liquid interface. The curves 1 – 3 in plot (b) show that χ has more pronounced influence on the shear mode of instability as the span of unstable wavenumbers reduces significantly with progressive increase in χ. In comparison, the interface mode is not much influenced by the change in χ.

The curves 1i (1s) and 2i (2s) in the plot (c) show that when $\mu_r > h_r^2$, at lower values of χ, the shear mode is the dominant mode. However, with progressive increase in χ, as the shear mode becomes stable, the interfacial mode takes over as the dominant mode of instability. In comparison, the curve 3s for $\mu_r > h_r^2$ shows that the shear mode is the only existing unstable mode and $(KC_i)_{max}$ reduces with increase in χ. The curves 1 – 3 in plot (d) show that Λ_{max} for both shear and interfacial mode increases as χ is increased.

2.6.5 Variations in the real part of wave speed

The curve 4 in the plots (a) – (d) shows that for the inclined channels although the salient features of the instabilities remain similar, $(KC_i)_{max}$ and Λ_{max} are comparatively larger as compared to the non-inclined channels. Figure 2.11 show the variation of the real part of the wave speed (C_r) with b, D_m, Da, and χ, respectively. Interestingly, plots (a) and (b) show that the parameters b and D_m hardly influence the wave speed of the interfacial mode whereas the travelling waves for the shear mode moves faster as b and D_m are progressively increased. Plot (a) shows that the wave speed corresponding to the shear mode monotonically increases with b whereas plot (b) shows that the wave speed initially increases with increase in the D_m and then saturates to a constant value.

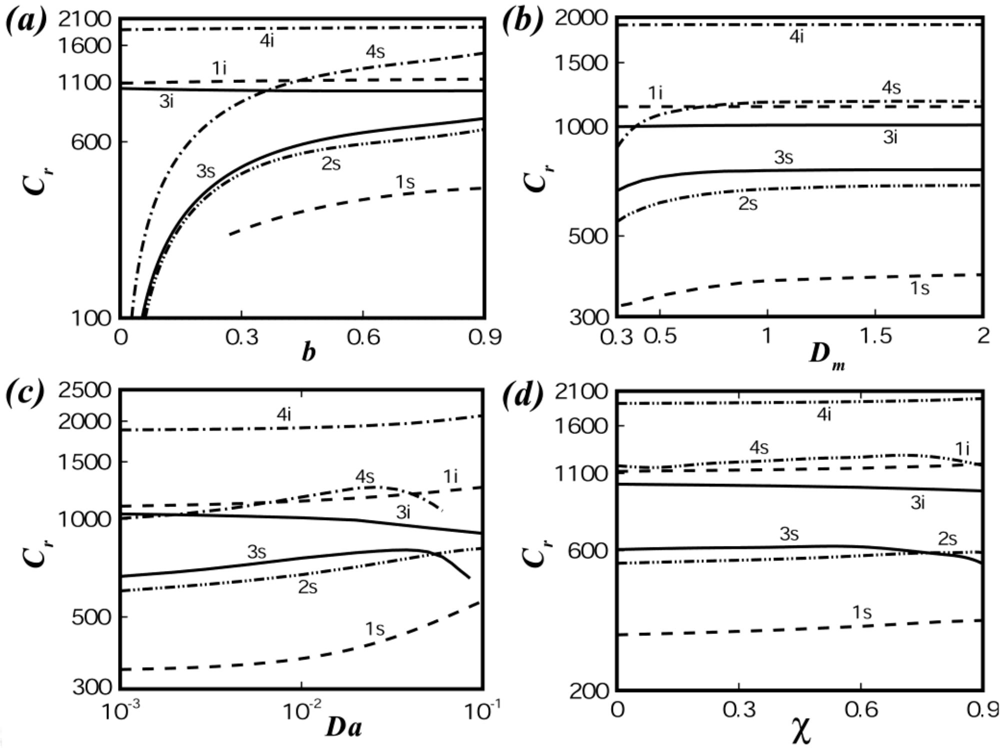

Figure 2.11: The plots (a) – (d) show the influence of real part of wave speed (C_r) with dimensionless porosity (*b*), porous medium thickness (*D*), Darcy Number (*Da*), stress-jump coefficient (χ), respectively. The curves (1) – (3) represent μ_r = 0.1, 1, and 10, respectively, curve 4 represent μ_r =10 and $\alpha = \pi/4$. The other parameters chosen for these plots are ρ_r =1, h_r = 1, b = 0.9, χ = 0.1, D_m = 1, and Da = 0.01.

The larger wave speed at larger b and D_m justifies the lesser frictional influence when the porosity and the thickness of the porous layer are increased. It may be noted here that wave speed corresponding to the interfacial mode is always higher than the shear mode. Curve 1i (3i) in plot (c) shows that for $\mu_r > h_r^2$ ($\mu_r < h_r^2$), the wave speed of the interfacial mode increases (reduces). In comparison, the curves 1s – 3s show that the wave speed for the shear mode always increase with *Da*. Plot (d) shows that the wave speeds of the instability modes are not much influenced by the variation in χ.

2.6.6 Special Features

The marginal stability curves in the (*Re* vs. K_c) plane are plotted in Figure 2.12(a) for both the interfacial and shear modes, when $\mu_r > h_r^2$. The region to the right of the curves (1i − 4i) corresponds to unstable interfacial modes and the region encapsulated by the curves (1s − 4s) corresponding to unstable shear mode. The results show that the unstable interfacial modes occur for all Reynolds numbers. For this mode of instability (curve 1i – 4i), the range of unstable wave numbers increases with increase in the inertial effects. As the permeability (*Da*) or the porosity (*b*) (curves 1i and 4i; curve 1i and 2i) increases, the ranges of unstable wave number decreases. However, there is no significant difference in the range of unstable wave number as the thickness of the porous layer changes (curve 1i and 3i).

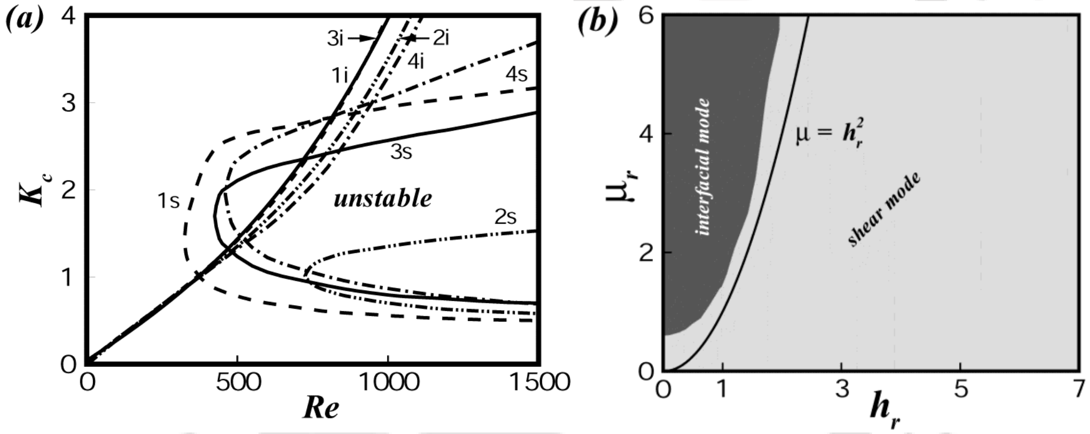

Figure 2.12: The plot (a) shows the variation of K_c with *Re*. The curves (1) – (4) represent b = 0.5, b = 0.1, D_m = 0.1, and Da = 0.001, respectively. The plot (b) show the contour for the dominant mode of instability on the thickness (h_r) and viscosity ratio (μ_r) plane. The other parameters are kept fixed at h_r = 1, μ_r = 10, ρ_r = 1, b = 0.5 , χ = 0.1, D_m = 1), and Da = 0.01.

In the case of shear modes, there exists a critical Reynolds number (for each set of parameter values considered) above which, the shear mode is unstable; this happens for a range of wave numbers $k_1 < k < k_2$ with $k_1 \neq 0$. This critical Reynolds number decreases with increase in porosity/permeability (curves 1s and 2s/curve 1s and 4s) and increase in the thickness (curves 1s and 3s) of the porous layer, This shows that a PPFPM system with thick porous layer, higher porosity and permeability is more unstable than a PPFPM with a thin porous with the same porosity and permeability. From Figure 2.12(a), it is also observed that in the low Reynolds number region, the unstable modes correspond to only the interfacial modes while in the high Reynolds number region, both the interfacial and shear modes co-exist. The results in this chapter unveil that the PPFPM composed of a pair of immiscible liquids flowing on a porous layer can be unstable when the flow rate is progressively increased in the porous layer. The flow inside the porous layer imparts larger inertial influence to the flow which in turn can lead to the appearance of the different instability modes. Figure 2.12(a) shows the neutral stability curves in the $K_c - Re$ parametric regime for the different instability modes of a PPF on a porous medium. The curves suggest with long-wave ($KC_i \rightarrow 0$ as $K \rightarrow 0$) interfacial mode (numbered with 'i' in the plot) can appear as a consequence of viscosity stratification across the interface even when the *Re* is trivial. The curves also show that that the larger span of unstable wavenumbers at a higher *Re*. Interestingly, when the viscosity stratification across the liquid-liquid interface is tuned by reducing the porosity and permeability of the porous layer the configuration is more stable, as the broken line shows a smaller span of unstable wavenumbers for the 'i' modes. The 's' mode appears at a larger threshold value of *Re* when the relatively stronger inertial effects start alleviating the viscous influences. Again, the broken lines corroborate that inertial forces are stimulated by the augmented slippage at the porous-liquid interface when the porosity and permeability of the porous layer is large. The span of unstable wavenumbers for shear modes grows with the increase in *Re* because of the larger inertial stresses at higher flow rates developed across the shear layers inside the PPFPM. The curves in the Figure 2.11 reflect that if the flow rate in a PPFPM is progressively increased the most dangerous is the interfacial mode, as it appears at the lowest *Re*. In such a situation, the shear mode appears at a higher *Re* and can influence the flow stability in the nonlinear regime, which cannot be unveiled through the present analysis. However, for a given flow rate the instability grows by picking up the dominant mode of instability and the shear mode can be the primary mode when the flow rate is high and the porous layer is sufficiently porous and permeable.

Figure 2.12(b) shows μ_r vs. h_r phase diagram for *Re* = 1500, which compares the results for the two-phase, pressure driven, and non-inclined PPF with PPFPM. The demarcation at $\mu_r = h_r^2$ indicate the domain for ‘interfacial mode’ and ‘shear mode’ of instability for PPF. The figure depict that for a PPF the left side of the solid line is a domain where only the interfacial mode exist whereas for the conditions at the right side of the solid line the shear mode will exist. Near the condition $\mu_r = h_r^2$ the PPF is neutrally stable. The contour plot suggests that , unlike PPF, which is always found to be neutrally stable at or near the condition $\mu_r = h_r^2$, for PPFPM the unstable modes can be found for all the conditions, $\mu_r = h_r^2$, $\mu_r < h_r^2$, and $\mu_r > h_r^2$. Further, the grey scale shows the domain for which interfacial (darker) and shear (lighter) modes are dominant for PPFPM with finite porosity, permeability, and thickness of the porous layer. The darker shade of the grey scale shows the zone where interfacial mode is the dominant whereas the shear mode (lighter gray) is dominant otherwise. Further, for PPFPM the dominant or sub-dominant shear mode is found to be present under any combination of thickness and viscosity ratios beyond a threshold *Re*. Concisely, the phase diagram convey that introduction of the porous layer induces larger instability to PPF and can significantly change the domain of dominance of the shear and interfacial modes.

2.7 SUMMARY

Instabilities of a two-layer Poiseuille flow on a Darcy-Brinkman porous layer have been explored. An O-S system, derived from the linearized governing equations and boundary conditions, is solved numerically to compare and contrast the time and length scales of the different instability modes. The important conclusions are:

(i) The study uncovers the presence of a pair of, long-wave interfacial mode and finite wavenumber shear mode of instabilities, for almost all possible combinations of viscosity (μ_r) and thickness ratios of the liquid layers (h_r). The interfacial mode is found to be absent only under the condition $\mu_r = h_r$. The observation is in stark contrast to the two-layer flow between non-porous plates where the shear (interfacial) mode appear when $\mu_r < h_r^2$ ($\mu_r > h_r^2$) and at $\mu_r = h_r^2$ the flow is neutrally stable. Importantly, the reduced friction at the liquid layers due to the presence of the porous layer in a microchannel can more readily develop instabilities in a two-phase flow as compared to the similar microchannels with smoother walls, which can eventually lead to a larger mixing of phases, heat and mass transfer, and emulsification of the immiscible phases.

(ii) A permeable thick porous layer with high porosity is found to reduce frictional influence at the liquid layers especially when the lower layer is of low viscosity. The study shows that this reduction in frictional influence from the porous layer rapidly fuels up the instability due to the shear mode whereas the interfacial mode remains relatively dormant to these influences. The strength of the shear mode monotonically increases with porosity, initially increases and then becomes constant with porous layer thickness, initially increases and then reduces with the increase in permeability, and reduces with the increase in the stress jump coefficient across the porous-liquid interface. Thus, a dominant (subdominant) interfacial (shear) mode can be observed by tuning the porous media parameters for all possible μ_r and h_r.

(iii) For a fixed set of porous media parameters the shear mode is found to appear beyond a critical *Re* especially when $\mu_r > h_r^2$. Further, the results show that introduction of the porous medium can fuel of multiple shear modes. The eigenfunctions of these modes confirm the location of the critical layers of these shear modes at the porous and the liquid layers.

(iv) The study also shows that the presence of gravity in the inclined channels can act as an additional destabilizing influence and alters the length and the time scales of both the interfacial and the shear modes of the instabilities. Interestingly, the variations in the time and the length scales remain similar to that observed for the non-inclined case. However, the inclination angle plays a crucial role in the transition from dominant interfacial to dominant shear mode of instability when the porous media properties are changed.

(v) The numerical results are validated employing Chebychev-tau spectral and spectral collocation methods. The eigenvalues for the two-layer flow over porous media with infinitesimally thin porous layer are also verified against the existing eigenvalues for the two-layer flow between rigid non-porous substrates (PPF). These exercises endorse the correctness of the results reported.

The study shows that the presence of the porous layer leads to a more unstable PPFPM, which can be of significant importance both micro and macroscopically in enhancing heat and mass transfer, mixing or stirring, and emulsification. The instability bounds and modes for a wide range thickness and viscosity of the liquid layers and porosity, permeability, and thickness of the porous layer can be of use while fabricating microfluidic or microelectronic devices employing two-layer channel flow.

Chapter 3

Instabilities of a Couette two-layer flow on a porous medium

ABSTRACT

We explore the salient features of the different instability modes of a pressure-driven two-layer plane Couette flow confined between a moving wall and a Darcy-Brinkman porous layer. A linear stability analysis of the conservation laws leads to an Orr-Sommerfeld system, which is solved numerically with appropriate boundary conditions to identify the time and length scales of the instability modes. The study reveals that the movement of the confining wall together with the slippage at the porous-liquid interface originating from the flow inside the porous layer can fuel up a pair of finite-wave-number shear modes in addition to the long-wave interfacial mode of instability. The shear modes dominate the interfacial mode especially when the frictional influence at the liquid layers is smaller due to the movement of the confining plate or due to the larger slippage at the porous-liquid interface. The shear modes are found to be present under all combinations of the viscosity μ_r and thickness h_r ratios of the liquid layers. This is in stark contrast to the two-layer flow confined between non-porous plates where the interfacial (shear) mode is observed only when, $\mu_r > h_r^2$ ($\mu_r < h_r^2$). Interestingly, the strength of one of the shear modes is found to increase with the velocity of the bounding moving plate, whereas the other shear mode gains strength in the presence of highly porous, permeable, and thick porous layers. The results reported can be of significant importance in the microscale two-phase flows where the presence of a bounding porous layer or moving wall can expedite the intermixing of layers to improve the multiphase mixing, heat and mass transfer, and emulsification characteristics.

This chapter is published in *Phys. Rev. E*, 87, 063003 (2013).

3.1 INTRODUCTION

In this chapter, the instability of a planar two-layer Couette flow confined between a rigid and a Darcy-Brinkman porous medium (CFPM) is investigated through a detailed Orr-Sommerfeld (O-S) analysis. The study seamlessly compares and contrasts both macro- and microscopic features of the different instability modes of the CFPM. Similar to two-layer plane Poiseuille flow (PPF), the CFPM is found to be unstable through the long-wave interfacial and the finite-wave-number shear modes. Interestingly, we observe the presence of twin shear modes for a CFPM in which one shows its dependence on the velocity of the bounding surface, whereas the other is responsive to the flow inside the porous layer. The strengths of these shear modes are tunable with the thickness, porosity, and permeability of the porous layer together with the plate velocity, whereas the interfacial mode remains rather insensitive to these changes. The shear modes emerge stronger than the interfacial mode when the frictional influence is reduced in the CFPM by increasing the porosity, thickness, and permeability of the porous layer or when the bounding plate velocity is faster. The conditions for the co-existence and dominance of all these modes are explored for a large parameter space, which can be of importance in the studies related to the microscale mixing and heat and mass transfer employing two-layer flows.

This chapter is organized in the following manner. In Sec. 3.2, the details of the governing equations and boundary conditions are shown. Brief outlines of the base state equations and the analysis on the base state velocity profiles are presented in Sec. 3.3. In Sec. 3.4, brief outlines of the linear stability analysis are presented. In Sec. 3.5, the numerical methods to solve the O-S system are discussed and the results are validated against previous investigations. The other results are analyzed in Sec.3.6 before summarizing in Sec 3.7.

3.2 PROBLEM FORMULATION

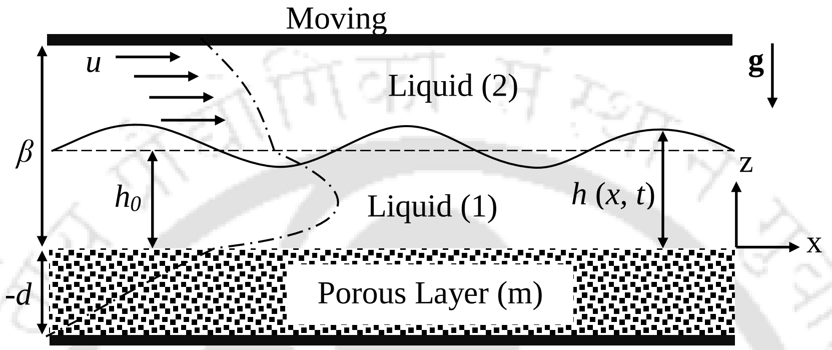

Figure 3.1: Schematic diagram of a two-layer flow inside a channel confined between a porous layer at the bottom and a moving substrate at the top. Where β is composite thickness of the two liquid layers, h_0 is mean thickness of the lower layer, h is variable thickness of the lower layer, *d* thickness of the porous media, *u* is the upper plate velocity and **g** is acceleration due to gravity.

Figure 3.1 schematically shows a typical pressure-driven two-layer CFPM. The liquid films are assumed to be of Newtonian, immiscible, incompressible (constant density ρ_j), and constant viscosity μ_j. The subscripts *1*, 2, and *m* of the variables represent the upper, lower, and porous layers, respectively. A two-dimensional Cartesian coordinate system is employed for the formulation along the *x*- and *z*- directions. The continuity and the equations of motion for the fluid layers (*j* = *1* and *2*) are,

$$\nabla \cdot \mathbf{u}_j = 0, \tag{3.1}$$

$$\rho_j \left[\dot{\mathbf{u}}_j + \left(\mathbf{u}_j \cdot \nabla \right) \mathbf{u}_j \right] = -\nabla p_j + \mu_j \nabla^2 \mathbf{u}_j + \rho_j \mathbf{g}. \tag{3.2}$$

Here $\mathbf{g}$, $\mathbf{u}_j\left\{u_j, w_j\right\}$, and p_j represent acceleration due to gravity, velocity vector, and pressure for the j^{th} layer, respectively. The over-dots represent the time derivative. The continuity and the equations of motion for the Darcy-Brinkman porous medium [80-88,91,92] are

$$\nabla\cdot\mathbf{u}_m = 0, \tag{3.3}$$

$$\frac{\rho_1}{b}\dot{\mathbf{u}}_m = -\nabla p_m + \mu_e\nabla^2\mathbf{u}_m - \frac{\mu_1}{\kappa}\mathbf{u}_m + \rho_1\mathbf{g}. \tag{3.4}$$

The porous medium has the effective viscosity, μ_e, porosity, $b = \mu_1/\mu_e$, permeability, κ, and thickness, *d*. At the porous-solid ($z = -d$), no-slip and impermeability boundary conditions ($\mathbf{u}_m$ = 0) are enforced. The impermeable upper plate ($w_2 = 0$) moves with a finite velocity ($u_2 = u_p$) at the liquid-solid interface ($z = \beta$). The continuity of velocities ($\mathbf{u}_1 = \mathbf{u}_m$), normal stresses balance ($-p_m + 2\mu_e w_{mz} = -p_1 + 2\mu_1 w_{1z}$), and tangential stress jump ($\mu_e u_{mz} - \mu_1 u_{1z} = \xi u_m/\sqrt{\kappa}$) are enforced as boundary conditions at the rigid-lower-layer-porous medium interface ($z = 0$). Here the symbol ξ is the stress-jump coefficient.[80,92] The tangential ($\mathbf{t}\cdot\overline{\boldsymbol{\tau}}_2\cdot\mathbf{n} = \mathbf{t}\cdot\overline{\boldsymbol{\tau}}_1\cdot\mathbf{n}$) and normal ($\mathbf{n}\cdot\overline{\boldsymbol{\tau}}_2\cdot\mathbf{n} - \mathbf{n}\cdot\overline{\boldsymbol{\tau}}_1\cdot\mathbf{n} = \gamma\nabla\cdot\mathbf{n}$) stress balances, the continuity of the velocities $\mathbf{u}_1 = \mathbf{u}_2$, and the kinematic condition $\dot{h} = -u_1\left(\partial h/\partial x\right) + w_1$ are enforced as boundary conditions at the deformable liquid-liquid interface ($z = h$). Here γ represents the interfacial tension of the liquid-liquid interface and, $\overline{\boldsymbol{\tau}}_j = \mu_j\left(\nabla\mathbf{u}_j + \nabla\mathbf{u}_j^T\right)$, is the Newtonian stress tensor. The symbols $\mathbf{n}$ and $\mathbf{t}$ represent the outward normal vector $\left(-h_x\big/\sqrt{1+h_x^2}, 1\big/\sqrt{1+h_x^2}\right)$ and the corresponding tangent vector

$\left(1\big/\sqrt{1+h_x^2},\, h_x\big/\sqrt{1+h_x^2}\right)$, respectively. The subscripts *x* and *z* denote the partial derivatives of the respective variable.

The governing equations (3.1) – (3.4) and the boundary conditions are transformed into non-dimensional forms employing the thickness of the lower layer h_0 as length scale and the viscous time scale $\rho_1 h_0^2 / \mu_1$. The other dimensionless variables employed for this purpose are $X = x / h_0$, $Z = z / h_0$, $H = h / h_0$, $T = t\mu_1 / \rho_1 h_0^2$, $\mathbf{U}_j = \mathbf{u}_j \rho_1 h_0 / \mu_1$, $V = u_p h_0 \rho_1 / \mu_1$, $\rho_r = \rho_2 / \rho_1$, $\mu_r = \mu_2 / \mu_1$, $B = \beta / h_0$, $h_r = B - 1$, $D_m = d / h_0$, $G = g h_0^3 \rho_1^2 / \mu_1^2$, and $P_j = p_j h_0^2 \rho_1 / \mu_1^2$. The resulting dimensionless continuity equations for the liquid layers (*i* = 1 and 2) and the porous medium (*i* = *m*) are,

$$\nabla \cdot \mathbf{U}_i = 0. \tag{3.5}$$

The dimensionless equations of motions for the liquid layers and the porous layer are

$$\dot{\mathbf{U}}_1 + \mathbf{U}_1 \cdot \nabla \mathbf{U}_1 = -\nabla P_1 + \nabla^2 \mathbf{U}_1 + \mathbf{G}, \tag{3.6}$$

$$\rho_r \left(\dot{\mathbf{U}}_2 + \mathbf{U}_2 \cdot \nabla \mathbf{U}_2 \right) = -\nabla P_2 + \mu_r \nabla^2 \mathbf{U}_2 + \rho_r \mathbf{G}, \tag{3.7}$$

$$(1/b)\dot{\mathbf{U}}_m = -\nabla P_m + (1/b)\nabla^2 \mathbf{U}_\mathbf{m} - (1/Da)\,\mathbf{U}_\mathbf{m} + \mathbf{G}. \tag{3.8}$$

The unperturbed lower, upper, and porous layers occupy the domains, $0 \le Z \le H$, $H \le Z \le B$, and $-D_m \le Z \le 0$, respectively. The dimensionless no-slip and impermeability boundary conditions, ($\mathbf{U}_m = 0$), are enforced at the porous-solid interface, $(Z = -D_m)$. The impermeable plate, ($W_2 = 0$), at the upper liquid-solid interface, (*Z* = *B*), moves with a uniform dimensionless velocity, $U_2 = V$. The continuity of velocities, ($\mathbf{U}_1 = \mathbf{U}_m$), normal, [$P_1 - P_m + 2\left(W_{mZ}/b - W_{1Z}\right) = 0$], and shear stress jumps, [$U_{mZ}/b - U_{1Z} - \left(\chi/\sqrt{Da}\right)U_m = 0$], are enforced at the liquid-porous interface $\left(Z=0\right)$. The continuity of velocities, ($\mathbf{U}_1=\mathbf{U}_2$), the kinematic equation, $\dot{H}=-U_1H_X+W_1$, the normal,

$$P_2-P_1+\frac{2}{\left[1+H_X^2\right]}\left\{\begin{array}{l}\left[\left(\left(1-H_X^2\right)W_{1Z}-H_X\left(W_{1X}+U_{1Z}\right)\right)\right]\\-\mu_r\left[\left(1-H_X^2\right)W_{2Z}-H_X\left(W_{2X}+U_{2Z}\right)\right]\end{array}\right\}=\frac{\Gamma H_{XX}}{\left[1+H_X^2\right]^{\frac{3}{2}}},$$

and the shear

$$\left[\left(U_{1Z}+W_{1X}\right)\left(1-H_X^2\right)+2H_X\left(W_{1Z}-U_{1X}\right)\right]=\mu_r\left[\left(U_{2Z}+W_{2X}\right)\left(1-H_X^2\right)+2H_X\left(W_{2Z}-U_{2X}\right)\right]$$

stress balances are enforced at the liquid-liquid interface $\left(Z=H\right)$. The subscripts *X* and *Z* in the expressions denote partial derivatives. In what follows, the formulations and discussion are carried out in terms of non-dimensional variables such as the Darcy number, $Da=\kappa/h_0^2$, represents permeability; $\chi=\xi/\mu_1$, which represents the stress-jump coefficient; $b=\mu_1/\mu_e$, which represents porosity; $D_m=d/h_0$, which represents the thickness of the porous layer; $G=gh_0^{\ 3}\rho_1^2/\mu_1^2$ is the Galileo number; and $\Gamma=\gamma h_0/\rho_1\nu_1^2$, is the capillary number.

3.3 BASE STATE ANALYSIS

The governing equations are solved for the unperturbed interface [$H=1, \bar{W}_j=0$, and $U_j=\bar{U}_j(Z)$ (*j* = *1*, *2*, and *m*)] and the following base state solutions of the *x*-directional flow are obtained:

$$\bar{U}_1=C_{11}Z^2+C_{12}Z+C_{13}, 0\le Z\le 1, \tag{3.9}$$

$$\bar{U}_2=C_{21}Z^2+C_{22}Z+C_{23},\ 1\le Z\le B, \tag{3.10}$$

$$\bar{U}_m=C_{m1}\,\mathrm{e}^{MZ}+C_{m2}\,\mathrm{e}^{-MZ}+C_{m3}, -D_m\le Z\le 0. \tag{3.11}$$

The global constraint that the volumetric flow rate $Q = \int_{-D_m}^{0} \bar{U}_m + \int_{0}^{1} \bar{U}_1 + \int_{1}^{B} \bar{U}_2$ in the channels is correlated to the base state pressure gradient by the cumbersome relation (Eq. 3.12) Here the velocities with over-bars $\bar{U}_1$, $\bar{U}_2$, and $\bar{U}_m$ represent the base state solutions at the lower, upper, and porous layers, respectively. The constants C_{ij} (i = 1, 2, and m; j = 1, 2, and 3) in expressions (3.9) – (3.11) are determined from the base state governing equations and boundary conditions as presented in the Appendix B and $M = \sqrt{b/Da}$.

$$P_{0X} = \frac{\begin{array}{l} 6G^{*}\left(-4Da\left(F_{+}-1\right)^{2} F_{-}\mu_r + M\left(\left(B-1\right)^{2}-\mu_r\right)a_2\right)a_3 + 6M\mu_r a_1^{2}\left(2\,V\mu_r + G^{*}\rho_r a_5\right) \\ +3G^{*}\left(-2\left(F_{+}-1\right)^{2} F_{-}\mu_r + M\left(\left(B-1\right)^{2}-\mu_r\right)\phi\right)a_4 \\ +a_1\left(\begin{array}{l} 2M\left(-6\left(Q+V-BV\right)\mu_r + G^{*}\left(3-6B+3B^{2}-\mu_r+6DDa\mu_r+2\left(B-1\right)^{3}\rho_r\right)\right)a_3 \\ -6G^{*}M\mu_r a_4 + 3\left(2\left(F_{+}-1\right)^{2} F_{-}\mu_r + M\left(-\left(B-1\right)^{2}+\mu_r\right)\phi\right)\left(2V\mu_r + G^{*}\rho_r a_5\right) \end{array}\right) \end{array}}{\left[\begin{array}{l} -2\left(\begin{array}{l} 12Da\left(F_{+}-1\right)^{2} F_{-}\mu_r + M\left(-1+\left(3-2B\right)B^{2}+\mu_r-6DDa\mu_r\right)a_1 \\ +3M\left(-\left(B-1\right)^{2}+\mu_r\right)a_2 \end{array}\right) \\ a_3 + 3\left(2\left(F_{+}-1\right)^{2} F_{-}\mu_r + M\left(-\left(B-1\right)^{2}+\mu_r\right)\phi + 2M\mu_r a_1\right)\left(a_1 a_5 - a_4\right) \end{array}\right]} \text{(3.12).}$$

Figure 3.2 shows the non-dimensional base state velocity profiles for a CFPM under varied conditions.

Figure 3.2(a) shows the influence of the velocity of the confining plate at the top V of the flow profiles. The curves clearly indicate that the CFPM is under the coupled influence of the slippage at the porous-liquid interface originating from the flow inside the underlying porous layer together with the motion of the confining plate. The location of the maximum velocity in the profile is observed in the lower layer because the viscosity of the upper layer is considered higher (solid line). The dashed lines suggest that with an increase in the plate velocity the relative strength of the inertial force become stronger than the viscous resistance.

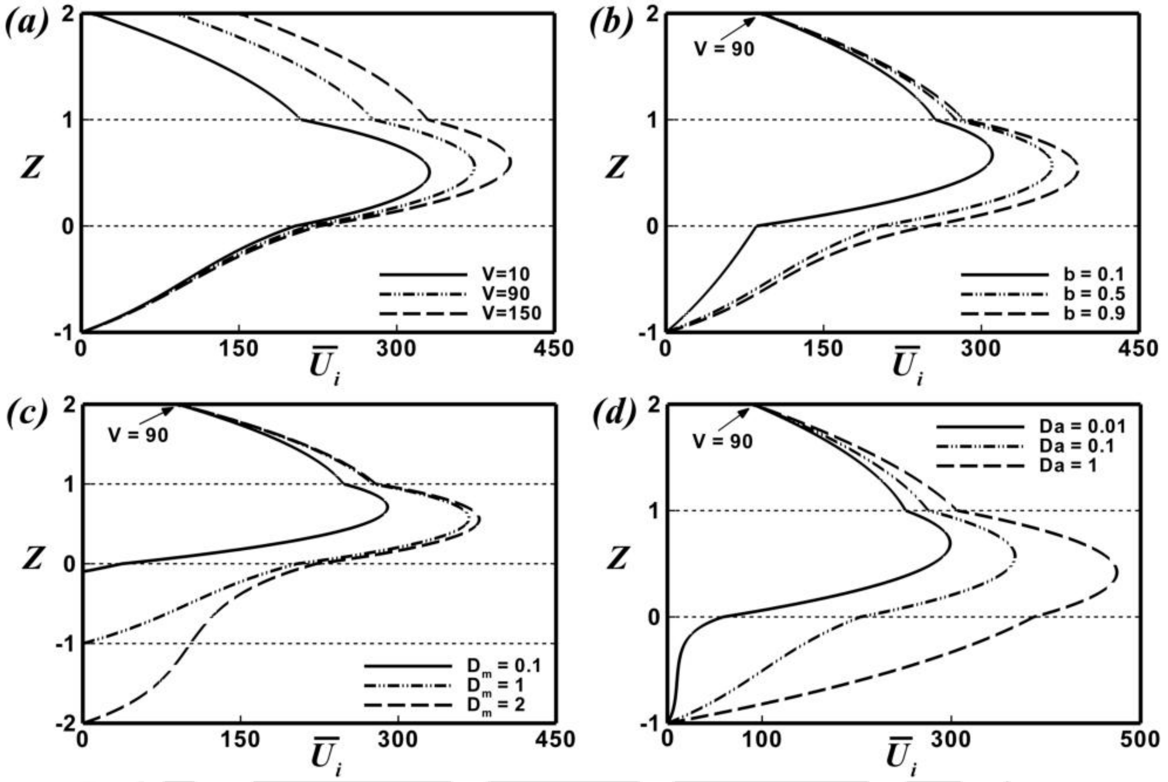

Figure 3.2: Plots showing the non-dimensional base state velocity $\bar{U}_i$ profiles across the width of the channel Z for corresponds to $\mu_r = 5$, $\rho_r = 1$, $h_r = 1$, $b = 0.5$, $\chi = 0.1$, $Da = 0.1$ and $D_m = 1$.

In such situations, the flow rate at the highly viscous upper layer becomes faster and the location of the maximum velocity at the lower layer progressively moves towards the upper layer. Figures 3.2(b) – 3.2(d) together show that when V is kept constant, an increase in the porosity b, permeability Da, and thickness of the porous layer D_m can cause a stronger flow inside the porous layer, which in turn can impart a stronger slippage at the porous-liquid interface. Thus, for a confined CFPM, a moving boundary and the presence of a bounding porous surface can lead to a stronger flow inside the channel, which in turn can induce instabilities by suppressing the frictional resistance.

3.4 LINEAR STABILITY ANALYSIS

The non-dimensional governing equations and the boundary conditions are linearized by imposing small amplitude perturbations to the base state, $U_j = \bar{U}_j + U'_j$, $W_j = W'_j$, and $P_j = \bar{P}_j + P'_j$, where *j* = *1*, *2*, and *m*. The over-bars indicate the base state and the primes denote perturbed quantities. The equations for velocity perturbations are then transformed in terms of the stream functions as, $U'_j = \partial\Psi_j / \partial Z$ and $W'_j = -\partial\Psi_j / \partial X$. The resulting governing equations and the boundary conditions are linearized by employing the normal linear modes $\Psi_j\left(X,Z,T\right) = \tilde{\Psi}_j\left(Z\right)e^{\mathbf{i}K(X-CT)}$, $P'_j\left(X,Z,T\right) = \tilde{P}_j\left(Z\right)e^{\mathbf{i}K(X-CT)}$, and $H\left(X,Z,T\right) = 1 + \tilde{H}e^{\mathbf{i}K(X-CT)}$ to obtain the following dimensionless coupled O-S equations for the liquid layers and the porous medium,

$$\left(D^2 - K^2\right)^2 \tilde{\Psi}_1 = \mathbf{i}K\left[\left(\bar{U}_1 - C\right)\left(D^2 - K^2\right) - D^2\bar{U}_1\right]\tilde{\Psi}_1, \tag{3.13}$$

$$\nu_r\left(D^2 - K^2\right)^2 \tilde{\Psi}_2 = \mathbf{i}K\left[\left(\bar{U}_2 - C\right)\left(D^2 - K^2\right) - D^2\bar{U}_2\right]\tilde{\Psi}_2, \tag{3.14}$$

$$\left(D^2 - K^2\right)^2 \tilde{\Psi}_m = \left(b / Da - \mathbf{i}KC\right)\left(D^2 - K^2\right)\tilde{\Psi}_m. \tag{3.15}$$

The notation *D* represent the differentiation d / dZ, $\nu_r \left(= \mu_r / \rho_r\right)$, K is the wavenumber, and *C* $(= C_r + \mathbf{i}C_i)$ is the phase speed, with C_r and KC_i the wave speed and the growth rate of the perturbation, respectively. Here C_r and C_i are the real and imaginary parts of the wave speed, respectively. The linearized non-dimensional boundary conditions at the porous-solid and liquid-solid boundaries are

$$\tilde{\Psi}_{mZ}(-D_m) = \tilde{\Psi}_m(-D_m) = \tilde{\Psi}_{2Z}(B) = 0, \tilde{\Psi}_2(B) = V. \tag{3.16}$$

At the porous-liquid interface (*Z* = 0),

$$\tilde{\Psi}_1 = \tilde{\Psi}_m, \tag{3.17}$$

$$\tilde{\Psi}_{1Z} = \tilde{\Psi}_{mZ}, \tag{3.18}$$

$$\frac{1}{b}\tilde{\Psi}_{mZZ} - \tilde{\Psi}_{1ZZ} = \frac{\chi}{\sqrt{Da}}\tilde{\Psi}_{mZ}, \tag{3.19}$$

$$\begin{aligned} & iK\bar{U}_{1Z}\Psi_1 + \left[-3K^2 + iK\left(C-\bar{U}_1\right)\right]\Psi_{1Z} + \Psi_{1ZZZ} \\ & = \frac{1}{b}\left[-3K^2 - \frac{b}{Da} + iKC\right]\tilde{\Psi}_{mZ} + \frac{1}{b}\tilde{\Psi}_{mZZZ} \end{aligned}. \tag{3.20}$$

At the liquid-liquid interface (*Z*= 1),

$$\tilde{\Psi}_1 = \tilde{\Psi}_2, \tilde{H} = \tilde{\Psi}_1 / \left(C-\bar{U}_1\right), \tag{3.21}$$

$$\left(\tilde{\Psi}_{1Z} - \tilde{\Psi}_{2Z}\right) + \left[\tilde{\Psi}_1 / \left(C-\bar{U}_1\right)\right]\left(\bar{U}_{1Z} - \bar{U}_{2Z}\right) = 0, \tag{3.22}$$

$$\begin{aligned} & \tilde{\Psi}_{1ZZZ} - 3K^2\tilde{\Psi}_{1Z} - \mu_r\tilde{\Psi}_{2ZZZ} + 3\mu_r K^2\tilde{\Psi}_{2Z} + iK\left(C-\bar{U}_1\right)\left(\tilde{\Psi}_{1Z} - \rho_r\tilde{\Psi}_{2Z}\right) \\ & + iK\left(\bar{U}_{1Z}\tilde{\Psi}_1 - \rho_r\bar{U}_{2Z}\tilde{\Psi}_2\right) - \tilde{\Psi}_1 / \left(C-\bar{U}_1\right)\left[\left(\bar{U}_{1Z} - \mu_r\bar{U}_{2Z}\right)2K^2 + i\Gamma K^3\right] = 0 \end{aligned}, \tag{3.23}$$

$$\left[\tilde{\Psi}_{1ZZ} + K^2\tilde{\Psi}_1\right] + \left(\bar{U}_{1ZZ} - \mu_r\bar{U}_{2ZZ}\right)\tilde{\Psi}_1 / \left(C-\bar{U}_1\right) - \mu_r\left[\tilde{\Psi}_{2ZZ} + K^2\tilde{\Psi}_2\right] = 0. \tag{3.24}$$

3.5 NUMERICAL ANALYSIS

The coupled O-S system in Eqs. (3.13) – (3.24) is an eigenvalue problem and is solved numerically to obtain the linear growth rate KC_i and the corresponding wavenumber *K* for the unstable modes. In this study, the most accurate D^2 algorithm proposed by Dongarra *et al.*[93] for the Chebyshev-tau QZ spectral method is employed to obtain the eigenvalues.[22,94] For this purpose, initially the computational domain is mapped onto $\left(-1, 1\right)$ by employing the transformations, $Z_1 = -2Z + 1$, $Z_2 = \frac{2}{B-1}Z - \frac{B+1}{B-1}$, and $Z_m = \frac{2}{D_m}Z + 1$, for the lower, upper, and porous layer equations, respectively. Thereafter, introducing the variables

$\eta(Z_1)=\tilde{\Psi}_1(Z)$, $\sigma(Z_2)=\tilde{\Psi}_2(Z)$, and $\zeta(Z_m)=\tilde{\Psi}_m(Z)$, the fourth-order ordinary differential equations (ODEs) (3.13) – (3.15) are transformed into the following six 2nd order ODEs in terms of the variables ξ, λ, and π:

$$L_1\eta \equiv \left(4d^2/dZ_1^{\,2}-K^2\right)\eta=\xi\,, \tag{3.25}$$

$$L_1\xi - iK\bar{U}_1\xi + 2iKC_{11}\eta + iKC\xi = 0\,, \tag{3.26}$$

$$L_2\sigma \equiv \left(\left(4/(B-1)^2\right)d^2/dZ_2^{\,2}-K^2\right)\sigma=\lambda\,, \tag{3.27}$$

$$\nu_r L_2\lambda - iK\bar{U}_2\lambda + 2iKC_{21}\sigma + iKC\lambda = 0\,, \tag{3.28}$$

$$L_m\zeta \equiv \left(\left(4/D^2\right)d^2/dZ_m^{\,2}-K^2\right)\zeta=\pi\,, \tag{3.29}$$

$$L_m\pi - \left(b/Da\right)\pi + iKC\pi = 0\,. \tag{3.30}$$

The boundary conditions at the porous-solid and liquid-solid boundaries are derived in terms of the transformed variables as

$$\zeta_{Z_m}(-1)=\zeta(-1)=\sigma_{Z_2}(1)=0,\ \sigma(1)=V. \tag{3.31}$$

The transformed boundary conditions at the porous-liquid interface are

$$\eta-\zeta=0\,, \tag{3.32}$$

$$\eta_{Z_1}+\frac{1}{D}\zeta_{Z_m}=0\,, \tag{3.33}$$

$$K^2\eta+\xi-\frac{K^2}{b}\zeta+\frac{2\chi}{D\sqrt{Da}}\zeta_{Z_m}-\frac{1}{b}\pi=0\,, \tag{3.34}$$

$$\left[\begin{array}{l} iKC_{12}\eta+2\left(2K^2+iK\bar{U}_1\right)\eta_{Z_1}-2\xi_{Z_1}+\dfrac{2}{bD}\left[2K^2+\dfrac{b}{Da}\right]\zeta_{Z_m} \\ -\dfrac{2}{bD}\pi_{Z_m}-C\left(2iK\eta_{Z_1}+\dfrac{2iK}{bD}\zeta_{Z_m}\right) \end{array}\right]=0\,. \tag{3.35}$$

The transformed boundary conditions at the liquid-liquid interface are

$$\eta-\sigma=0, \tag{3.36}$$

$$\left[\begin{matrix} C\left(2\eta_{Z_1}+\left(2/B-1\right)\sigma_{Z_2}\right)-\left(\left(2C_{11}+C_{12}\right)-\left(2C_{21}+C_{22}\right)\right)\eta \\ -2\bar{U}_1\eta_{Z_1}-\left(2\bar{U}_1/B-1\right)\sigma_{Z_2} \end{matrix}\right]=0, \tag{3.37}$$

$$\left[\begin{matrix} C\left(2K^2\eta+\xi-2\mu_r K^2\sigma-\mu_r\lambda\right)+2\left(\left(C_{11}-\mu_r C_{21}\right)-\bar{U}_1K^2\right)\eta \\ -\bar{U}_1\xi+2\mu_r\bar{U}_1K^2\sigma+\mu_r\bar{U}_1\lambda \end{matrix}\right]=0, \tag{3.38}$$

$$\begin{aligned} & C^2\left(2iK\eta_{Z_1}+\left(2iK\rho_r/B-1\right)\sigma_{Z_2}\right) \\ & +C\left(\begin{matrix} -iK\left(2C_{11}+C_{12}\right)\eta-4\left(iK\bar{U}_1+K^2\right)\eta_{Z_1}+2\xi_{Z_1}+iK\rho_r\left(2C_{21}+C_{22}\right)\sigma \\ -\left(4/B-1\right)\left(\mu_r K^2+iK\rho_r\bar{U}_1\right)\sigma_{Z_2}+\left(2\mu_r/\left(B-1\right)\right)\lambda_{Z_2} \end{matrix}\right) \quad . \\ & +\left[\begin{matrix} \left[2\left(\left(2C_{11}+C_{12}\right)-\mu_r\left(2C_{21}+C_{22}\right)\right)K^2+iK\bar{U}_1\left(2C_{11}+C_{12}\right)+i\Gamma K^3\right]\eta \\ -\left(2\mu_r\bar{U}_1/\left(B-1\right)\right)\lambda_{Z_2}+2\left(2\bar{U}_1K^2+iK\bar{U}_1^{\,2}\right)\eta_{Z_1}-2\bar{U}_1\xi_{Z_1} \\ -iK\bar{U}_1\rho_r\left(2C_{21}+C_{22}\right)\sigma+\left(2/\left(B-1\right)\right)\left[2\mu_r\bar{U}_1K^2+iK\rho_r\bar{U}_1^{\,2}\right]\sigma_{Z_2} \end{matrix}\right]=0 \end{aligned} \tag{3.39}$$

The subscripts Z_1, Z_2, and Z_m denote ordinary differentiation. The transformed ODEs are then expanded in terms of Chebyshev polynomials $T_n\left(z\right)$. For N Chebyshev polynomials, the eigenvalues are obtained for a ($6N$+12) × ($6N$+12) matrix corresponding to six-second order ODEs and twelve boundary conditions. The accuracy of the eigenvalues is tested by varying the number of polynomials and in the process the spurious eigenvalues are eliminated. The eigenvalues obtained from the Chebyshev-tau QZ spectral method are validated by solving the set of equations (3.25) – (3.39) employing the spectral collocation method.[95] The eigenvectors reported here are found using the spectral collocation method. The numerical results are also validated against a number of configurations available in the literature. Figure 3.3(a) shows the variation in the linear growth coefficient KC_i vs. wavenumber K plotted from the collocation method (circles) and Chebyshev-tau QZ method (solid line). The plots confirm that both numerical methods predict the same eigenvalues for the CFPM.

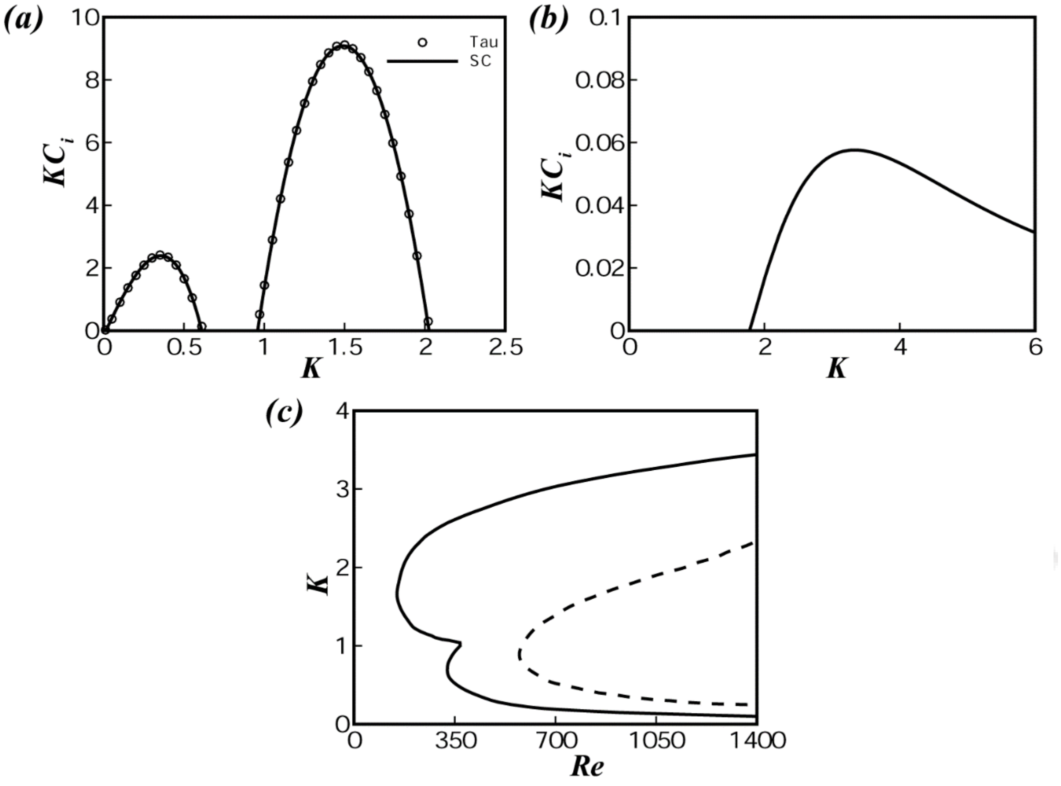

Figure 3.3: Plot (a) & (b) show the variation of growth rate KC_i with wavenumber K. Plot (a) corresponds to b = 0.5, D_m = 1, h_r = 1, ρ_r = 1, μ_r = 5, χ = 0.1, Γ = 16000, and Da = 0.01. The solid line (dots) shows the result from the Chebyshev-tau QZ (collocation) method. Plot (b) corresponds to b = 0, D_m = 0.01, h_r = 6, ρ_r = 1, μ_r = 2, χ = 0, Γ = 0, Da = 0.0001, and G = 0. Plot (c) shows neutral stability diagram for the critical Reynolds number Re as a function of critical wavenumber K_c. The line solid line (dashed) corresponds to h_r = 0.3 (h_r = 0.5).The other parameters are b = 0.78, ρ_r = 0, μ_r = 0, χ = 0, Γ = 0, Da = 0.0175, and G = 0.

Figure 3.3(b) reproduces a KC_i vs. K plot for a two-layer CF[23] in the limit where the porous layer is almost impervious. Further, Figure 3.3(c) shows a neutral stability diagram of a single layer of liquid confined between a rigid and a porous substrate.[86] This plot is obtained from the present analysis in the asymptotic limit where the upper plate velocity is zero and the liquid layers are kept identical. The code is also verified with the available results of the two-layer PPF in the limits where the porous layer is absent and the upper plate is stationary. Concisely, Figure 3.3 corroborates the accuracy of the code at various asymptotic limits.

3.6 RESULTS AND DISCUSSION

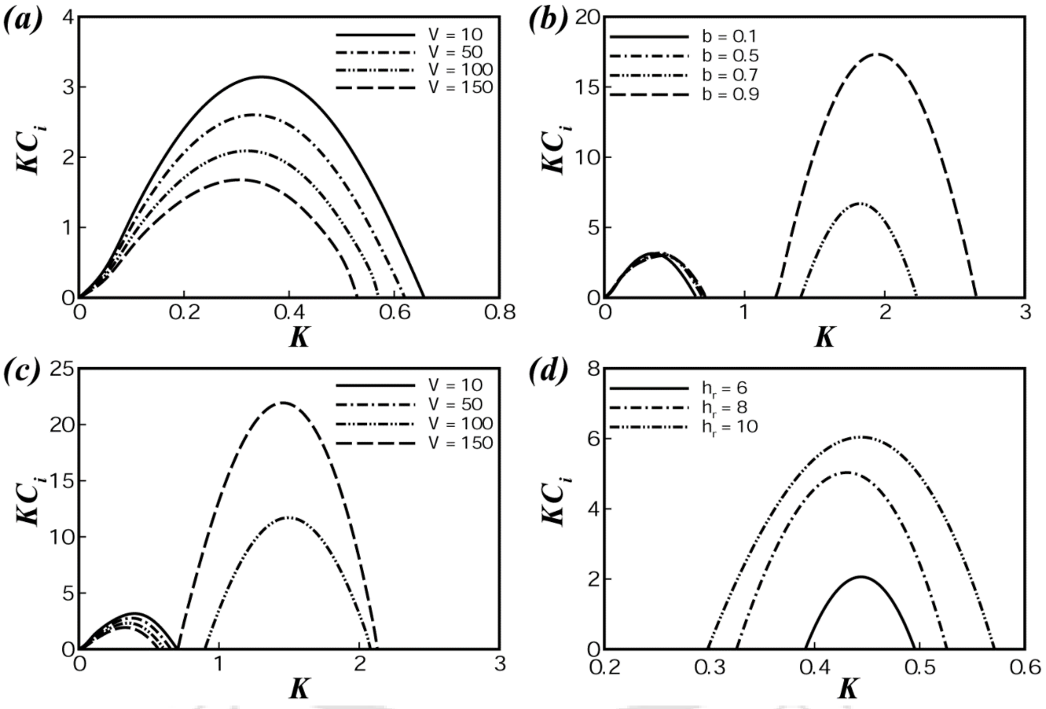

Figure 3.4: Plots show the variation of growth rate (KC_i) with wavenumber (K). Plot (a) corresponds to different V when b = 0.1, D_m = 1, ρ_r = 1, μ_r = 5, h_r = 1, χ = 0.1, and Da = 0.01; Plot (b) corresponds to different b when V = 10, D_m = 1, ρ_r = 1, μ_r = 5, h_r = 1, χ = 0.1, and Da = 0.01; Plot (c) corresponds to different V when b = 0.5, D_m =1, ρ_r = 1, μ_r = 5, h_r = 1, χ = 0.1, and Da = 0.01; Plot (d) corresponds to different h_r when V = 50, b = 0.001, D_m = 0.001, ρ_r = 1, μ_r = 5, χ = 0.0, and Da = 0.000001.

Previous theoretical studies[12] suggest that a two-layer PPF with equal density liquid layers is unstable either because of the long-wave interfacial mode when the condition $\mu_r > h_r^2$ is met or because of the finite-wave-number shear mode when $\mu_r < h_r^2$ or is neutrally stable when $\mu_r = h_r^2$.

The results discussed here highlight the importance of the underlying porous layer or the bounding moving plate of the CFPM largely around these conditions. It may be noted here that the results are reported in terms of upper to lower viscosity μ_r and thickness h_r ratios. To uncover the salient macro- and microscopic features of the CFPM, the following parameter space has been used for the analysis: ρ_j ~ 1000 kg/m^3, μ_j ~ 0.001– 0.01 Pa s, d_j ~ 0.0001 – 0.1 m, γ ~ 0.02 N/m, and x-directional velocity ~ 10^{-4} – 0.5 m/s.

Figure 3.4 shows the presence of different instability modes under varied conditions. Figure 3.4(a) shows that when $\mu_r > h_r^2$, a CFPM on a porous layer with very small porosity and permeability shows only an interfacial mode of instability, as observed previously for the two-layer PPF between rigid and impervious surfaces.[12,23] With an increase in the velocity of the upper plate *V*, the frictional resistance progressively reduces the viscosity stratification across the interface which in turn weakens the interfacial mode of instability. In contrast, the curves in Figure 3.4(b) show that when the porosity *b* of the same configuration is increased, a finite-wave-number shear-mode of instability appears beyond a critical porosity even when $\mu_r > h_r^2$. In this situation, an increase in porosity intensifies the flow inside the porous layer, which induces a larger slippage at the porous-liquid interface and reduces the frictional influence in the liquid layers to induce the shear mode of instability. Figure 3.4(c) shows that for a fixed *b* when *V* is progressively increased, the shear mode also can appear beyond a threshold plate velocity. A larger velocity of the bounding plate escalates the strength of the inertial force, which is the major reason for this shear mode at a larger *V*. Importantly, the shear modes reported in the Figure 3.4(b) and 4(c) are of different nature as compared to the conventional shear mode of two-layer CF or PPF under the condition $\mu_r < h_r^2$, which is shown separately in the Figure 3.4(d). The origin of these twin shear modes in the CFPM can be attributed to, (i) the velocity of the moving plate at the top and (ii) the slippage at the porous-liquid interface due to the stronger flow inside the porous medium. The shear modes are found to coexist with the interfacial mode as dominant or sub-dominant modes even when the condition $\mu_r > h_r^2$ is met. Concisely, Figure 3.4 confirms that movement of the bounding plate and the presence of a bounding porous layer can stimulate an additional shear mode of instabilities in a CFPM.

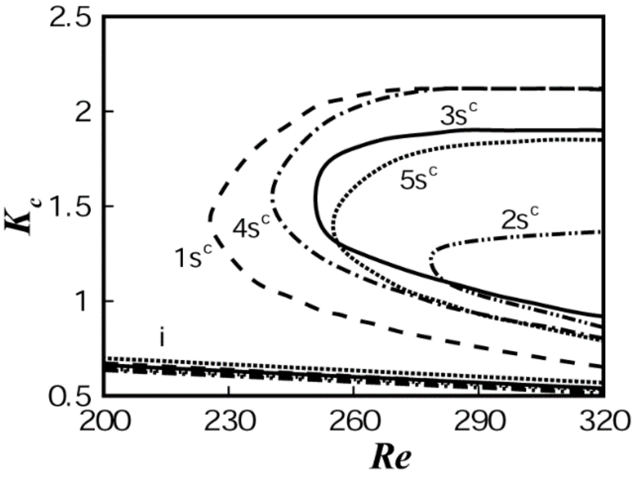

Figure 3.5: Plot showing the neutral stability, which is the variation of K_c with *Re* when the plate velocity *V* is varied. The curves with 'i',and 's^c' represent the interfacial, and shear mode, respectively . Curves (1) – (5) represent b = 0.5, b = 0.3, D_m = 0.7, *Da* = 0.005, and χ = 0.5, respectively. The other parameters are kept fixed at $\mu_r = 5$, $\rho_r = 1$, $h_r = 1$, b = 0.5 (for curves 3 – 5); D_m = 1 (for curves 1, 2, 4, and 5); *Da* = 0.01 (for curves 1 – 3, and 5), and χ = 0.1 (for the curves 1 – 4).

The neutral stability diagrams in Figure 3.5 show more clearly the point of onset of the shear modes under the condition $\mu_r > h_r^2$. It may be noted here that the symbols ‘i’ and ‘s’ in the plots represent the interfacial and shear modes of instability, respectively. For ease of analysis, the shear mode appearing from the movement of the plate (from the porous layer) is denoted by ‘s^c’ (‘s^p’) in the plots. In this figure, *Re* is changed by altering the plate velocity *V*. Curves with the notation ‘i’ suggest the presence of a long-wave interfacial mode of instability under all conditions. In this plot, the progressive reduction in the span of unstable wavenumbers with an increase in the *Re* is due to a reduction in the viscosity stratification across the interface with an increase in *V*. Curve 1s shows that the finite-wave-number shear mode appears beyond a threshold *Re* and can co-exist with the interfacial modes at larger *V*. Curves 2s – 5s show that a reduction in porosity, thickness, and permeability, and an increase in stress-jump coefficient of the porous layer can delay the onset of the shear mode to a larger value of *Re*. The curves also suggest that the span of unstable wavenumbers for the shear mode increases with a progressive increase in *Re*. Figure 3.5 shows that the shear modes associated with the movement of the upper plate or due to the presence of a porous medium appear only beyond a threshold *Re* but can grow stronger as the relative inertial influence increases with *Re*. In Couette flow of two immiscible phases is unstable on a porous layer. In this Figure 3.5, *Re* is changed by altering the plate velocity *V*. In such a situation, we can anticipate the appearance of the different instability modes as the flow inside the configuration becomes stronger by *V* increases. Figure shows the neutral stability curves in the K_c – *Re* parametric regime for the different instability modes of a Couette flow on a porous medium having constant porosity, permeability and thickness. The symbols ‘i’ and ‘s’ in the plot represent the interfacial and shear modes of instability, respectively. The shear mode appearing from the movement of the plate (from the porous layer) is denoted by ‘s^c’ in the plot. The ‘i’ mode confirm the long-wave nature ($KC_i \to 0$ as $K \to 0$). The span of unstable wavenumbers for the ‘s^c’ shear modes grows with the increase in *Re*. The shear mode destabilizes shorter wavelength mode as compared to the interfacial mode. In micro- channel mixing experiments if we create a porous media underneath and movement of the bounding plate. The system is readily develop the shear mode of instabilities, which can eventually lead to a larger mixing, heat and mass transfer, and emulsification of the immiscible phases.

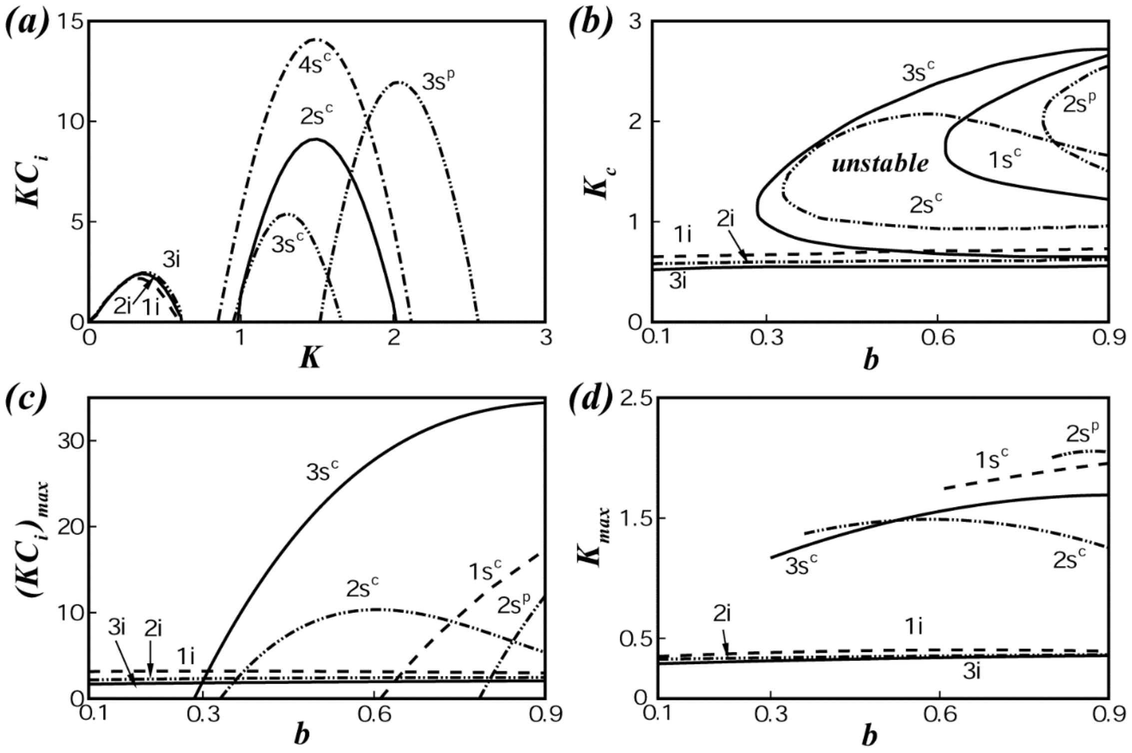

Figure 3.6: Plots showing the influence of porosity *b*. The curves with ‘i’ and ‘s’ represent the interfacial and shear modes, respectively. Plot (a) shows the variation of KC_i with K when V = 90 with curves (1) – (3) representing b = 0.1, 0.5, and 0.9, respectively. Curve 4 represents V = 110 and b = 0.5. Plots (b) – (d) show the variations of K_c, $(KC_i)_{max}$, and K_{max} with b, respectively with curves (1) – (3) representing V = 10, 90, and 150, respectively. The other parameters are μ_r = 5, ρ_r = 1, h_r = 1, χ = 0.1, D_m= 1, and Da = 0.01.

In Figures 3.6 and 3.8 – 3.10, plot(a) shows the variation of KC_i with K and plots (b) – (d) show the neutral stability plots of $(KC_i)_{max}$ and K_{max}, respectively, with the porous-media parameters. The dominant growth coefficient $(KC_i)_{max}$ and wavenumber K_{max} are the global maxima from the KC_i vs K plots and the dominant wavelength is $\Lambda_{max} = 2\pi / K_{max}$. The critical wavenumber K_c is obtained by enforcing the neutral stability condition $KC_i = 0$.

Figure 3.6 shows the influence of the porosity *b* of the porous layer on the inception and the growth of the different modes of the instabilities. Figure 3.6(a) shows that when $\mu_r > h_r^2$ and the porous layer is nearly impervious (small *b*), the CFPM can be unstable by only the long-wave interfacial mode (curve 1i). An increase in *b* allows a stronger flow inside the porous layer, which empowers the inertia force to subdue the viscous resistance at the lower layer. Consequently, a finite-wave-number shear mode of instability (curve 2s^c) appears alongside the interfacial mode (curve 2i). With an increase in *b*, the shear mode progressively becomes the dominant mode (curve 2s^c). Interestingly, at higher values of *b*, the presence of multiple shear modes (curves 3s^c and 3s^P) is observed. In such a situation, the shear mode that appeared at intermediate values of *b* becomes subdominant (curve 3s^c), whereas the newly appeared mode becomes the dominant mode (curve 3s^P) at very high values of *b*. Importantly, when *b* is kept constant and *V* is increased (curves 2s^c and 4s^c) the shear mode originating due to the movement of the plate becomes stronger. The neutral stability in Figure 3.6(b) shows the conditions for the onset and coexistence of the different instability modes. Curves 1 – 3 in this plot represent different velocities; curve 2 was already discussed in Figure 3.6(a). Curve 1 in Figure 3.6(b) conveys that when V = 10, the interfacial mode is the only unstable mode at lower values of b. Beyond a critical value of b_c= 0.614, the frictional influence due to the flow inside the porous layer diminishes in such a manner that the finite-wave-number shear mode (curve 1s^c) appears. With a further increase in b, as the flow empowers the inertial force the span of unstable wavenumbers increases for the shear mode whereas the interfacial mode remains rather insensitive to the change in b. Curve 2 in this plot shows that if V = 90 and other conditions are kept the same, the shear mode appears at a much lower critical porosity b_c= 0.33. Interestingly, in such a situation, when b is progressively increased we observe the appearance of twin shear modes (curves 2s^c and 2s^p), as discussed previously for Figure 3.6(a). The plot also shows that with an increase in b at constant V, the span of unstable wavenumbers reduces for the first mode (curve 2s^c) before the second mode appears (curve 2s^p). Further, the span of unstable wavenumbers for the ‘s^p’ mode is more towards the shorter-wavelength regime as compared to the ‘s^c’ mode. Importantly, curve 3 in Figure 3.6(b) shows that as V is increased to 150, the twin shear modes combine to show a single shear mode (curve 3s^c). Figure 3.6(b) clearly show that an increase in the velocity of the upper plate can significantly reduce the viscous influence in a CFPM, which can expedite the onset of the shear mode of instability at a much lower value of b. Further, as observed in the base state profiles in the Figure 3.2(b), an increase in b induces larger slippage at the porous-liquid interface, which is reflected in the increase in the span of unstable wavenumbers for the shear mode with an increase in b in Figure 3.6b. Curves 1 – 3 in Figure 3.6(c) and 3.6(d) represent V = 10, 90, and 150, respectively. The plots show that with a progressive increase of b and V, as the inertia is empowered, shorter-wavelength shear modes become the dominant mode of instability. Interestingly, as the viscosity stratification across the interface remains unchanged, the interfacial mode (curves 1i – 3i) is insensitive to these influences. The plots highlight that at lower *V* only the ‘s^c’ shear mode exists, at intermediate *V* the coexistence of both ‘s^c’ and ‘s^p’ shear modes is observed, and at higher *V* both the shear modes combine to form again a single ‘s^c’ shear mode of instability. Interestingly, both shear modes are found to gain strength with *V* and *b*, whereas when twin-modes are present the ‘s^p’ (‘s^c’) mode gains (loses) strength with an increase in *b*. Figure 3.6(d) shows that with an increase in *b*, the wavelength of the dominant shear mode progressively move towards the smaller-wavelength regime, whereas the same for the interfacial mode remains constant. It may be recalled here that the CFPM considered in Figure 3.6 meets the criteria $\mu_r > h_r^2$ and $\rho_r = 1$ for which a two-layer PPF is unstable only through the interfacial mode of instability.

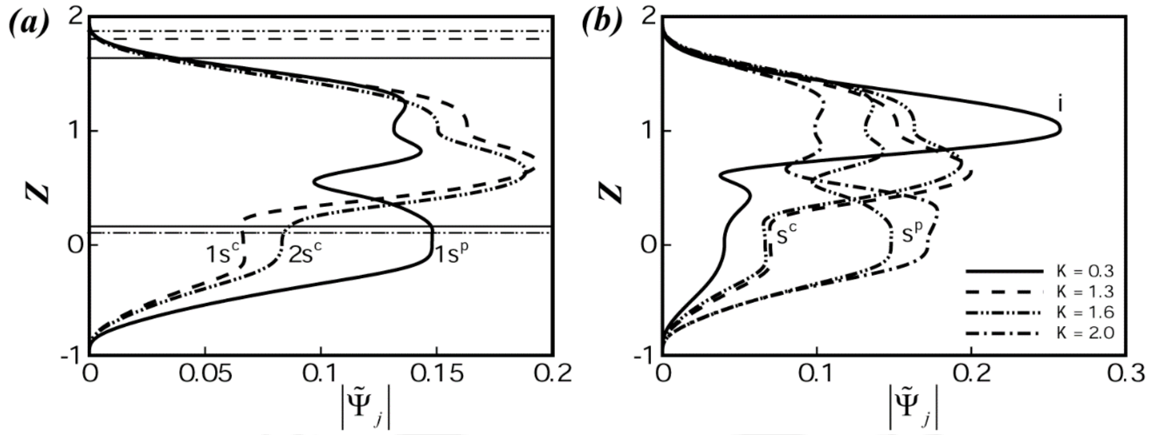

Figure 3.7: The plots show the eigenvectors at different porosities. Curve $1s^p$ and $1s^c$ represent the twin shear modes at $b = 0.9$. Curve $2s^c$ represents the single shear mode at $b = 0.6$. The curve $3s^c$ represent the combined shear mode at $b = 0.9$ and $V = 150$. Plot (b) shows the eigenvector at different *K*. The curves i, s^p, and s^c represent the interface mode and shear modes originating from the porous layer and Couette flow, respectively. The other parameters $\mu_r = 5$, $\rho_r = 1$, $h_r = 1$, $\chi = 0.1$, $D_m = 1$, and $Da = 0.01$.

The figure suggests that the introduction of the underlying porous layer together with movement of the upper plate can reduce the frictional influence and increase the relative strength of the inertia force to develop multiple finite-wave-number shear modes of instability. From the application point of view, the presence of these instability modes can be particularly useful in improving the heat and mass transfer and mixing characteristics especially in the microfluidic devices.

The origin of the twin shear modes is also investigated through an eigenfunction analysis. Figure 3.7 shows the magnitudes of the perturbed stream function $\left|\tilde{\Psi}_j\right|$ corresponding to the eigenvalues obtained for the different modes in Figure 3.6(a). In Figure 3.7 (a) the horizontal dashed, dash-double-dotted, dash-dotted, and solid lines show the locations for the critical layers ($U = C_r$), which are found to be situated in either the upper ($Z > 1$) or the lower layer ($0 < Z < 1$). Interestingly, all three (dashed) curves show three distinct changes in the slope for $\left|\tilde{\Psi}_j\right|$: (i) near the porous-liquid interface, (ii) near the liquid-liquid interface and (iii) at the bulk of the lower layer. However, among these three slope changes in $\left|\tilde{\Psi}_j\right|$ one is found to be predominant. For the case with higher porosity (b = 0.9) two different eigenfunctions corresponding to the two different eigenvalues for the shear modes are analyzed at $V = 90$. The solid line $1s^p$ shows the largest variation in $\left|\tilde{\Psi}_j\right|$ near the porous-liquid interface ($Z = 0$) whereas the dashed curve $1s^c$ shows the same at the lower liquid layer. The dash-double-dotted curve $2s^c$ shows that a reduction in the porosity ($b = 0.6$) leads to an eigenfunction similar to curve $1s^c$. In this case we obtained only one eigenvalue for the shear mode. Further, the dash-dotted curve $3s^c$ shows that a eigenfunction corresponding to the single eigenvalue obtained at $b = 0.9$ and $V = 150$, which again depicts the largest variation in $\left|\tilde{\Psi}_j\right|$ at the lower liquid layer. A comparison between the curves $2s^c$ and $1s^p$ confirms that the change in $\left|\tilde{\Psi}_j\right|$ near the porous-liquid interface gains strength when the porosity is increased. In contrast, the same happens to $\left|\tilde{\Psi}_j\right|$ at the lower layer when the upper plate moves faster (curves $1s^c$, $2s^c$, and $3s^c$). In Figure 3.7(b) the eigenfunctions obtained at different values of K are shown. The plot corresponds to curve 3 in Figure 3.6(a) (b = 0.9), which showed the existence of the interfacial mode at lower K, the appearance (disappearance) of a Couette shear mode (interfacial mode) at moderately higher K, the co-existence of both shear modes at higher values of K, and the existence of only the porous-medium mode at higher K. Following this trend, the Figure 3.7(b) shows the largest variation in $\left|\tilde{\Psi}_j\right|$ at the liquid-liquid interface (curve i) at lower values of K(= 0.3), which corresponds to the interfacial mode of instability. At moderately higher values of K (= 1.3), $\left|\tilde{\Psi}_j\right|$ shows sharp variation in the lower layer (dashed line) when there exists only the Couette flow shear mode of instability. At K = 1.6, the coexistence of both Couette and porous-medium modes is observed, as shown by the dash-double-dot lines with the marker s^c and s^p. In this case, the change of slope of $\left|\tilde{\Psi}_j\right|$ for the s^p mode takes place near the porous-liquid interface whereas the same for the s^c mode occurs at the lower liquid layer. At higher values of K (= 2.0), we observe only the presence of the porous-medium mode as shown by the dash-dotted line with the marker s^p. Clearly, the eigenfunction plots shown in Figure 3.7 connect the origin of the s^c and s^p modes with the movement of the plate at the top and the slippage at the porous-liquid interface, respectively. Apart from the porosity of the porous layer, the thickness of the porous layer D_m can be an alternative parameter to reduce the frictional influence in a CFPM, as evident in Figure 3.8.

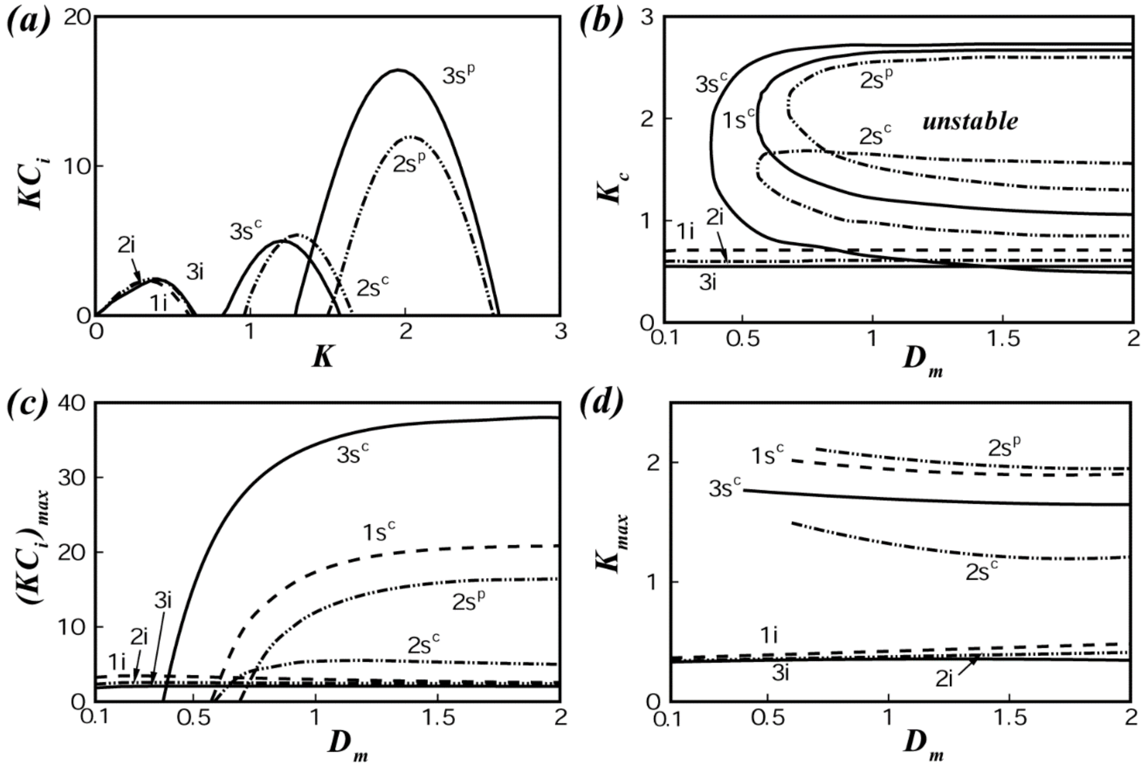

Figure 3.8: The plots show the influence of porous-medium thickness D_m. The curves with ‘i’ and ‘s’ represent the interfacial and shear modes, respectively. Plot (a) shows the variation of KC_i with K when V = 90. Curves (1) – (3) represent D_m = 0.1, 1, and 2, respectively. Plots (b) – (d) show the variations of $K_c, \left(KC_i\right)_{max}$, and K_{max} with D_m, respectively. Curves (1) – (3) represent V = 10, 90, and 150, respectively. The other parameters are $\mu_r = 5$, $\rho_r = 1$, $h_r = 1$, $b = 0.9$, $\chi = 0.1$, and $Da = 0.01$.

Figure 3.8(a) shows that when $\mu_r > h_r^2$ and D_m is very small, the CFPM can be unstable only through the interfacial mode (curve 1i). An increase in D_m allows flow inside the porous layer, which expedites the slippage at the porous-liquid interface developing a pair of finite-wave-number shear modes (curves 2s^c and 2s^p) alongside the interfacial mode. The s^p mode of instability becomes the dominant mode at moderately high values of D_m. With a further increase in D_m, the s^p mode grows in strength whereas the growth of the interfacial and s^c modes remains invariant. The neutral stability curve 1 in the Figure

3.8(b) conveys that when V = 10, interfacial mode (curve 1i) is the only unstable mode at lower values of D_m and the s^c mode (curve $1s^c$) appears only beyond a critical thickness (D_m= 0.56). With an increase in D_m, initially the span of unstable wavenumbers increases for the shear modes and then becomes constant, whereas the same for the interfacial mode it always remains constant. Curve 2 in the Figure 3.8(b) shows that if V is increased to 90, the 's^c' mode appears at a similar critical thickness of the porous layer (D_m= 0.56). However, a 's^p' shear mode is also observed at an higher thickness of the porous layer (D_m= 0.68). Interestingly, curve 3 shows that at V= 150, the twin shear modes combine to show a single shear mode with a larger span of unstable wavenumbers (curve $3s^c$). Previously, the base state velocity profiles Figure 3.2(c) showed that an increase in D_m induces larger slippage at the porous-liquid interface, which increases the convective influence in the CFPM. However, beyond a threshold D_m the reduction in the frictional influence saturates to a constant value, which is reflected in curves 1 – 3 of the Figures. 3.8(c) and 3.8(d). The plots highlight that at very low D_m the interfacial mode is dominant and the shear mode appears only after a threshold porous layer thickness. With a progressive increase in D_m the shear mode becomes the dominant mode as the frictional influence reduces. However, beyond a threshold D_m as the relative increase in the inertial influence saturates, $(KC_i)_{max}$ reaches a constant value. The behavior of CFPM here resembles a single layer plane Poiseuille flow over a porous medium.[87,88] Briefly, Figure 3.8 suggests that although the inertial influence due to the increase in the porous layer thickness can induce shear modes, the strength of these modes can only be increased until a threshold value of D_m.

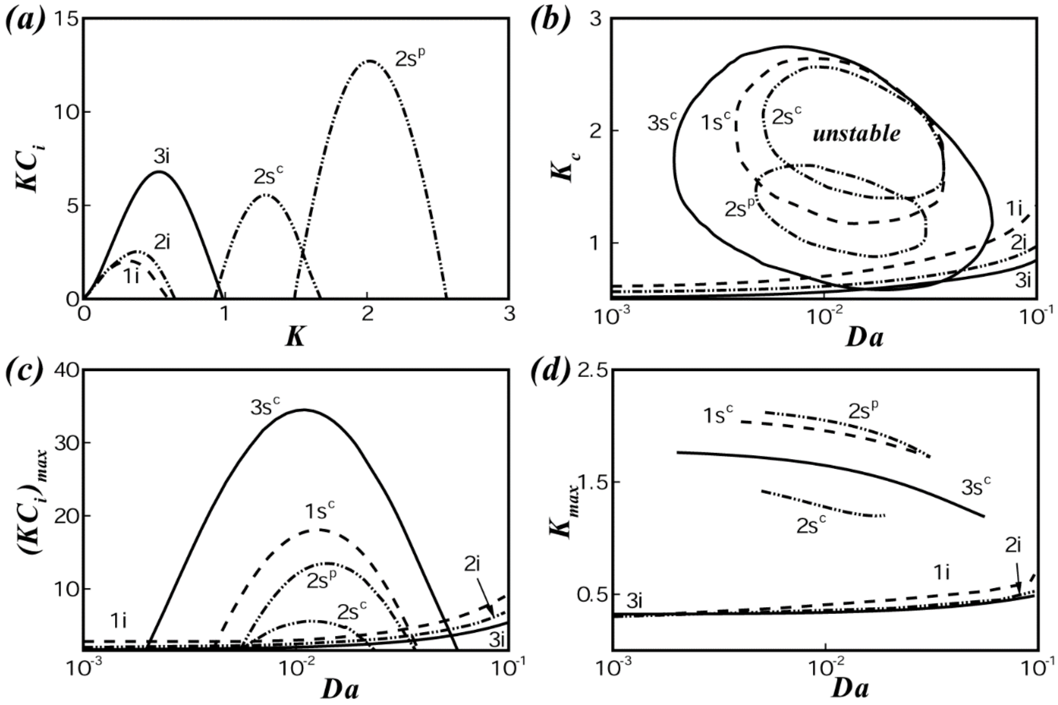

Figure 3.9: The plots show the influence of Darcy Number *Da*. Curves with 'i' and 's' represent the interfacial and shear modes, respectively. Plot (a) shows the variation of KC_i with *K* when *V* = 90. Curves (1) – (3) represent *Da* = 0.001, 0.01, and 0.096, respectively. Plots (b) – (d) show the variations of K_c, $(KC_i)_{max}$, and K_{max} with *Da*, respectively. Curves (1) – (3) represent *V* = 10, 90, and 150, respectively. The other parameters are μ_r = 5, ρ_r = 1, h_r = 1, *b* = 0.9, χ = 0.1, D_m= 1, and *Da* = 0.01.

Figure 3.9 shows that the permeability of the porous layer (*Da*) is another parameter that can influence the onset of shear modes. Curve 1i in Figure 3.9(a) shows that in the presence of an impermeable porous layer only the interfacial mode is present. With a progressive increase in *Da*, as more flow is allowed inside the porous layer we observe the appearance of twin s^c and s^p shear modes of the instabilities. However, beyond threshold permeability, higher flow inside the porous layer weakens the flow in the fluid layers and the strength of the shear mode is found to decay. A CFPM on a highly permeable porous layer is unstable only through the interfacial mode, as shown by curve 3i. The neutral stability diagram in the Figure 3.9(b) confirms the appearance of the shear mode after a lower-threshold value of *Da* and the disappearance of the same beyond an upper-threshold value of *Da*. The plots also support that at lower *V*, only the s^c shear mode is observed whereas at intermediate *V*, both shear modes coexist (curves $2s^c$ and $2s^p$). At higher *V*, the shear mode combines to show the presence of a single shear mode for a larger span of *D*a, as shown by curve $3s^c$. Curves 1 – 3 in the Figure 3.9(c) more clearly show that at low *Da* the interfacial mode is the dominant mode (curves 1i – 3i). With a progressive increase in *Da*, the s^c (s^p) shear mode is the dominant mode at lower (higher) *V*. However, at very high velocities both the shear modes combine to form a single shear mode, as depicted by curve $3s^c$. The strength of the shear modes decay beyond a limiting value of *Da* as the interfacial mode again becomes the dominant mode of instability. Figure 3.9(d) shows that with an increase in *Da*, the shear (interfacial) mode progressively move towards the larger (smaller) wavelength regime. Figure 3.9 shows that the twin shear modes can be observed only for a window of *Da*, while the interfacial mode of instability is the dominant mode for very high or very low *Da*.

Figure 3.10 summarizes the influence of the stress-jump coefficient χ on the different modes of instabilities. Curves 1i – 3i in Figure 3.10(a) show that an increase in χ infuses strength to the interfacial mode of instability. In contrast, the shear modes are only observed at some intermediate values of χ. Further, the shear modes disappear at higher values of χ. The plots clearly suggest that an increase in the stress-jump coefficient increases the frictional influence in the lower layer, which in turn increases the viscosity stratification between the liquid layers. In consequence, the shear modes become weaker as the frictional force dominates over the inertial influence.

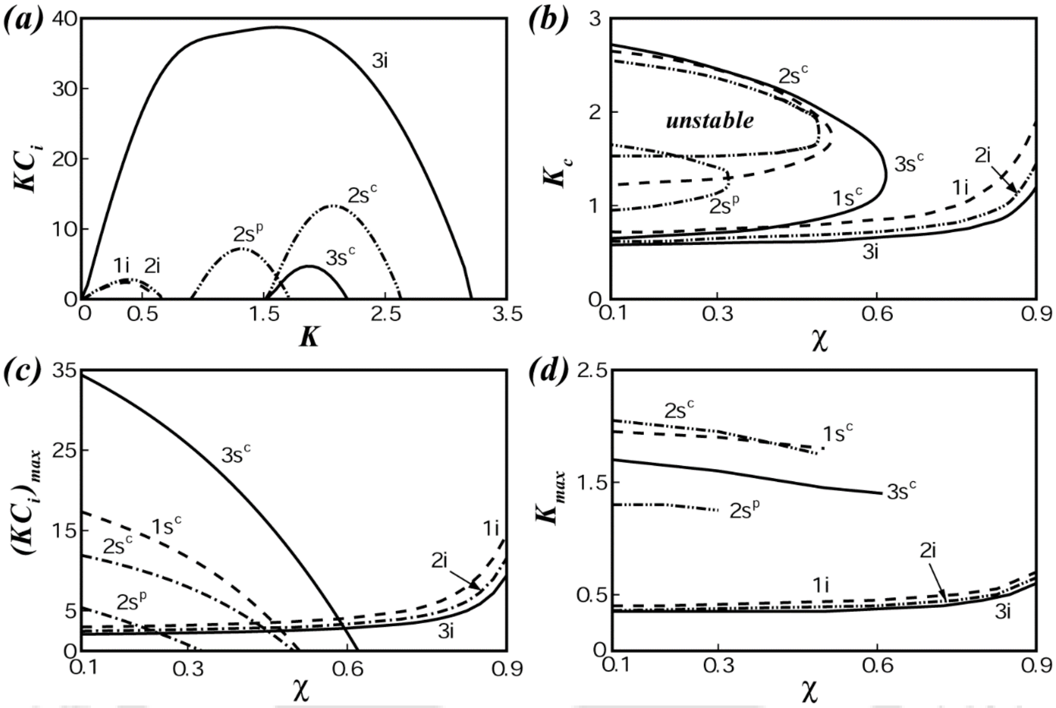

Figure 3.10: Plots show the influence of stress jump coefficient χ. The curves with ‘i’ and ‘s’ represent the interfacial and shear modes, respectively. Plot (a) shows the variation of KC_i with K when V = 90. Curves (1) – (3) represent χ = 0.0, 0.5, and 1, respectively. Plots (b) – (d) show the variations of K_c, $\left(KC_i\right)_{max}$, and K_{max} with χ, respectively. Curves (1) – (3) represent V = 10, 90, and 150, respectively. The other parameters are μ_r = 5, ρ_r = 1, h_r = 1, b = 0.9, χ = 0.1, D_m= 1, and Da = 0.01.

The neutral stability diagrams in Figure 3.10(b) shows more clearly the weakening of the shear modes and insurgence of the interfacial mode with an increase in χ. Curves 1 – 3 in these plots confirm that the span of unstable wave numbers for the shear mode progressively reduces and the same for the interfacial mode gradually increases with an increase in χ. The plot also confirms that at lower V, only the s^c shear mode is observed, whereas at intermediate V, both shear modes coexist (curves 2s^c and 2s^p). At higher V, the shear mode combines to show the presence of a single shear mode with a larger span of unstable wavenumbers, as shown by curve 3s^c. Curves 1 – 3 in the Figure 3.10(c) clearly highlight that at low χ the lesser frictional influence ensures a dominant shear mode of instability for a CFPM with a highly porous layer. However, with an increase in χ the interfacial mode becomes the dominant mode because of the increase in the frictional influence. The plot also suggests that the transition from a dominant shear to a dominant interfacial mode takes place at higher values of χ when V is larger. Figure 3.10(d) shows that with an increase in χ, the shear (interfacial) mode progressively move towards the larger (smaller) wavelength regime.

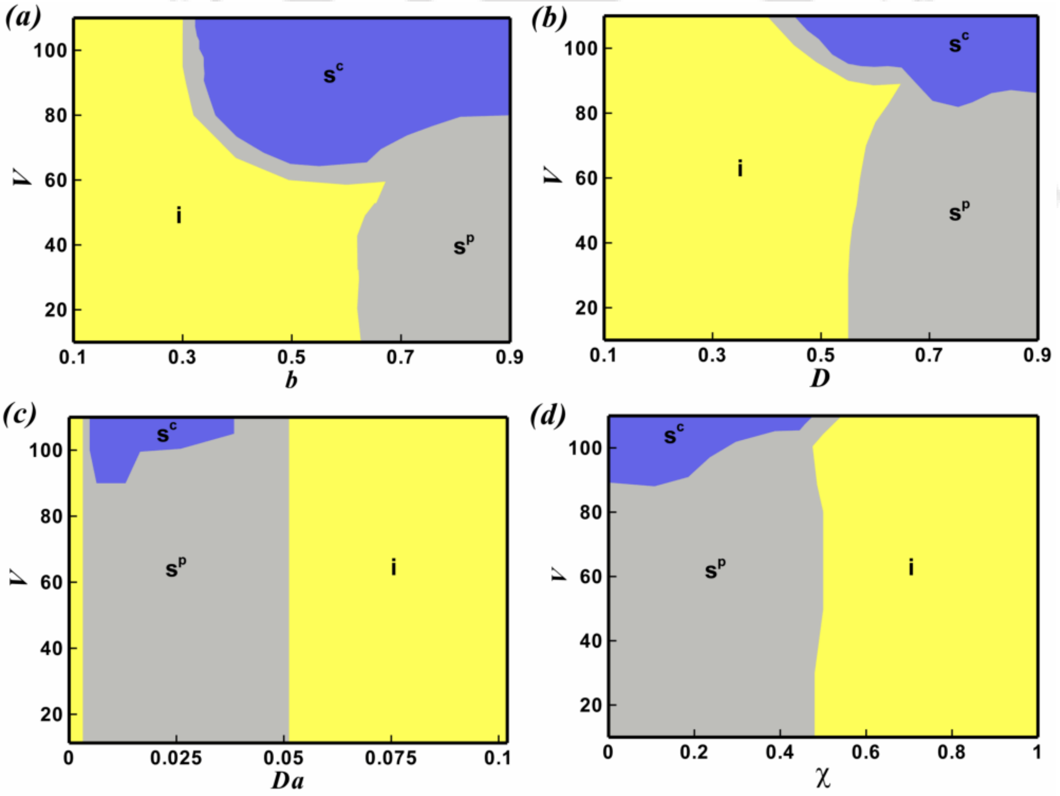

Figure 3.11: Contours plots show the conditions for dominant ‘i’ – interfacial, ‘s^p’/‘s^c’ – shear modes of the instabilities in the phase planes having V and porous medium parameters. Plot (a) – (d) corresponds to different b, D_m, Da, and χ . The other parameters are $\mu_r = 5$, $\rho_r = 1$, $h_r = 1$, $b = 0.9$, $\chi = 0.1$, $D_m = 1$, and $Da = 0.01$.

Figure 3.11(a) – 3.11(d) show phase diagrams for V vs the porous medium parameters b, D_m, Da, and χ. In this figures, we have identified the dominant mode among the interfacial and two shear modes of instabilities under varied conditions. The darker gray zones in the plots clearly depict that the ‘s^c’ mode is the dominant one when the velocity of the top plate is high. Further, the ‘s^p’ mode is found to be the dominant mode when the porous layers are of high porosity or are thick, [Figure 3.11(a) and 3.11(b)]. Figure 3.11(c) shows that at moderately high *Da*, the ‘s^p’ mode is the dominant mode, but at high *Da* the shear mode diminishes to make the interfacial mode as the dominant mode of instability, as observed previously in Figure 3.9. Figure 3.11(d) shows that although the ‘s^p’ mode is the dominant mode at lower values of χ, at the higher values where the frictional influence increases, the interfacial mode becomes the dominant mode. Figure 3.11 provides an overall idea of the dominance of the different unstable modes for a wide range of parameters.

3.7 SUMMARY

Instabilities of a pressure-driven two-layer plane Couette flow on a Darcy-Brinkman porous layer have been explored. An O-S analysis has been carried out by linearizing the governing equations and the boundary conditions. The O-S system is solved numerically by employing two different methods to obtain the accurate eigenvalues, which are also validated against the results of the asymptotic cases that are available in the literature. The following are the important conclusions.

The study uncovers that apart from the conventional long-wave interfacial mode and finite-wave-number shear mode of instabilities of a two-layer CF, the CFPM may develop at least two additional finite-wave-number shear modes because of the movement of the bounding plate and the flow inside the porous layer. Thus, for a CFPM, beyond a critical velocity of the moving plate or beyond some threshold values of the physical properties of the porous layer, a finite-wave-number shear mode(or modes) can be observed for almost all possible combinations of viscosity μ_r and thickness ratios of the liquid layers h_r. Conditionally, we also observe the presence of twin shear modes, one of which grows with bounding plate velocity, whereas the other grows with the increased slippage at the porous-liquid interface. A permeable thick porous layer with high porosity is found to reduce frictional influence in the liquid layers especially when the lower layer is of low viscosity. The study shows that the influence of the porous layer affects the shear mode than the interfacial mode. The shear mode is more unstable at high porosity, whereas a porous layer with constant porosity and permeability can only increase the strength of the shear mode until a threshold thickness. The strength of the shear mode is found to increase and then decreases with the increase in permeability. The increased frictional influence with the increase in the stress-jump coefficient causes the reduction in strength of the shear modes and increase in strength of the interfacial modes. The analysis confirms that a transition from a dominant interfacial to a dominant shear mode can be performed only by tuning the velocity of the moving plate and the porous layer parameters for all possible μ_r and h_r. Concisely, the study shows that the CFPM can be more unstable than conventional pressure-driven two-layer CF or PPF due to the flow inside the underlying porous layer coupled with the movement of the bounding plate. The augmented inertia (reduced friction) due to the presence of the porous layer or due to the movement of the bounding plate can more readily develop the shear modes of instabilities, which can eventually lead to a larger mixing, heat and mass transfer, and emulsification of the immiscible phases. The reported parameter bounds for the various unstable modes of the porosity, permeability, and thickness of the porous layer can be of importance in future studies related to the two-layer channel flow inside microfluidic devices.

Chapter 4

Instabilities of free bilayer flow on an inclined porous medium

ABSTRACT

The instabilities of an inclined free bilayer flowing over a Darcy-Brinkman porous layer have been explored. The bilayer is composed of a pair of liquid films with coupled deformable liquid-liquid interface and liquid-air free-surface. An Orr-Sommerfeld analysis of the governing equations and boundary conditions uncover that this configuration can be unstable by pair of long-wave interfacial modes at the free-surface and the interface together with a pair of finite wavenumbers shear modes originating from the inertial influences at the liquid layers. The study shows that similar to the bilayers on impervious surfaces all these modes appear only beyond a critical flow rate. In particular, one of the shear modes originate from the augmented inertial influence of the porous layer and is found to be the dominant mode even at moderately high values of porosity, permeability, and thickness of the porous layer. The porous media specific shear mode, (i) gains strength with increase in porosity, (ii) gains strength with increase in thickness of the porous layer before saturating to a constant value, and (iii) initially gains strength with increase in permeability and then loses its strength at higher permeability. Further, increase in flow rate and the ratios (upper to lower) of the thicknesses and viscosities of the liquid layers also could profoundly increase the strength of the porous media mediated shear mode. Interestingly, interfacial modes and the conventional shear mode specific to a bilayer on an impervious surface are found to be dormant to the change in the porous layer parameters. Although the changes in the in the ratios of thickness of the films, film viscosities and the flow rate in the bilayers causes larger destabilization to the other modes, the porous media shear mode dominate the instability of a bilayer flowing down an inclined porous medium. Briefly, the study highlights that the additional inertial influence originating from the flow inside porous media can further destabilize a free bilayer flow

on an inclined plane, which can be of importance to improve, mixing, emulsification, and heat and mass transfer characteristics in the microscale devices.

The manuscript on this chapter is currently under review.

4.1 INTRODUCTION

The hydrodynamic instabilities of a free bilayer on an inclined porous medium (Figure 4.1) is another interesting configuration, which is yet to be explored in detail. In the present work, with the help of an Orr-Sommerfeld (O-S) analysis of the governing equations and boundary conditions, the instabilities of a free bilayer on a inclined Darcy-Brinkman porous medium have been studied. Previous studies indicate that a free bilayer can be unstable by twin interfacial modes at the liquid-air free-surface and at the liquid-liquid interface. In this work, we highlight the influences of the porous layer properties on these two modes together with we identify additional modes of instabilities that can originate from the amplified inertia from the underlying porous layer. In order to ensure the accuracy of the results, the O-S system is solved employing two different numerical techniques and verified with the available asymptotic cases in the literature. An eigenfunction analysis is also performed to identify the critical layers and the location of the finite wavenumber modes of the instabilities. Interestingly, the analysis uncovers that for a fixed Reynolds number, thickness, and viscosity ratios, the porous medium parameters can fuel up an entirely new finite wavenumber shear mode of instability while the other interfacial and shear modes remain dormant to these influences. The strength of the newly found shear mode increases with, (i) increase in porosity, (ii) initially increase and then becomes constant with increase in the thickness, and (iii) initially increase and then reduce with the increase in permeability. In comparison, when the Reynolds number, viscosity ratio, and the thickness ratio are varied, the porous layer is found to influence the strength of the interfacial and the shear modes that are in general present for a free bilayer flowing on an impervious surface. The newly obtained porous media mode shows a conditional dominance in the regime where the slippage at the porous-liquid interface is high. The results discussed here can be of importance especially in improving the mixing, heat and mass transfer, emulsification, and phase separation of free bilayers flows.

The chapter is organized in the following manner: Sec. 4.2 shows the problem formulation in which the governing equations and boundary conditions are discussed. The base state velocity profiles are discussed in the Sec. 4.3. In the Sec. 4.4 and 4.5, the linear stability analysis and the numerical methods to solve the O-S system are discussed. The results are analyzed in the Sec.4.6 followed by the summary in the Sec 4.7.

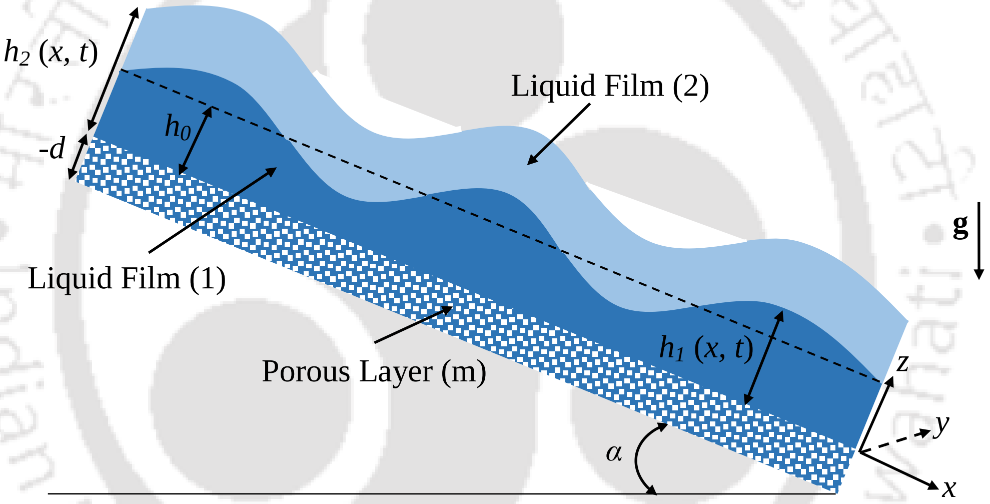

Figure 4.1: Schematic diagram of a two-layer flow over an inclined porous medium. Where d is thickness of the porous medium, h_0 is mean thickness of the lower layer, h_1 is variable thickness of the lower layer, h_2 variable composite thickness of the upper layer, α is angle of inclination, and **g** is acceleration due to gravity.

4.2 PROBLEM FORMULATION

Figure 4.1 schematically show the free bilayer configuration considered in this work. In the formulation, the origin is fixed at the porous-liquid interface $(z=0)$ and the unit vectors ($\mathbf{e_x}$, $\mathbf{e_z}$) for the two-dimensional (2-D) flow are directed along the x- and z-

directions. The variables for the lower (upper) liquid layers are denoted by the subscripts *1* (*2*) and the variable for the porous medium can be identified from the subscript *m*. The films are assumed to be Newtonian, isothermal, incompressible, and immiscible. The films are also considered to possess constant density (ρ_j) and viscosity (μ_j). The bilayer flows over a Darcy-Brinkman porous medium of porosity δ, permeability κ, and thickness *d*. The continuity and the equations of motions for the for the films (*j* = *1* and *2*) in the vector form are,

$$\nabla \cdot \mathbf{u}_j = 0, \tag{4.1}$$

$$\rho_j \left[\dot{\mathbf{u}}_j + \left(\mathbf{u}_j \cdot \nabla \right) \mathbf{u}_j \right] = -\nabla p_j + \mu_j \nabla^2 \mathbf{u}_j + \rho_j \mathbf{g}. \tag{4.2}$$

The mass and momentum balance for the Darcy-Brinkman porous medium[81,82] are,

$$\nabla \cdot \mathbf{u}_m = 0, \tag{4.3}$$

$$\frac{\rho_1}{\delta} \dot{\mathbf{u}}_m = -\nabla p_m + \mu_e \nabla^2 \mathbf{u}_m - \frac{\mu_1}{\kappa} \mathbf{u}_m + \rho_1 \mathbf{g}. \tag{4.4}$$

In the Eqs. (4.1) – (4.4), the notations, **g**, $\mathbf{u}_j \left\{ u_j, w_j \right\}$, and p_j represent the acceleration due to gravity, the velocity vector, and the pressure for the layers j = *1*, *2*, and *m*, respectively. The over-dots represent the time derivative and the porosity is defined as the ratio of the lower layer viscosity to the effective viscosity of the porous layer ($\delta = \mu_1 / \mu_e$). No-slip and non-permeability conditions are applied as boundary conditions at the porous-solid interface ($z = -d$),

$$\mathbf{u}_m = 0. \tag{4.5}$$

The continuity of normal stress, jump in the tangential stress, and equality of the velocities are enforced as boundary conditions at the porous-liquid interface ($z = 0$),

$$\mathbf{u}_1 = \mathbf{u}_m , \tag{4.6}$$

$$-p_m + 2\mu_e w_{mz} = -p_1 + 2\mu_1 w_{1z} , \tag{4.7}$$

$$\mu_e u_{mz} - \mu_1 u_{1z} = \frac{\xi}{\sqrt{\kappa}} u_m . \tag{4.8}$$

Here the jump coefficient ξ is the measure of spatial heterogeneity at the porous-liquid interface[34] and the subscripts *x* and *z* denote partial derivatives. The normal and tangential stress balances and the continuity of the velocities are enforced as boundary conditions at the liquid-liquid interface ($z = h_1$),

$$\mathbf{n}_1 \cdot \bar{\boldsymbol{\tau}}_2 \cdot \mathbf{n}_1 - \mathbf{n}_1 \cdot \bar{\boldsymbol{\tau}}_1 \cdot \mathbf{n}_1 = \gamma_1 \left(\nabla \cdot \mathbf{n}_1 \right), \tag{4.9}$$

$$\mathbf{t}_1 \cdot \bar{\boldsymbol{\tau}}_2 \cdot \mathbf{n}_1 = \mathbf{t}_1 \cdot \bar{\boldsymbol{\tau}}_1 \cdot \mathbf{n}_1 , \tag{4.10}$$

$$\mathbf{u}_1 = \mathbf{u}_2 . \tag{4.11}$$

Here h_1 represents thickness of the lower layer, γ_1 represents the interfacial tension of the liquid-liquid interface, $\boldsymbol{\tau}_j$ is the stress tensor, ∇ is gradient operator, $\mathbf{n}_i \left[\left(-h_{ix} \Big/ \sqrt{\left(1+h_{ix}^2\right)}, 1 \Big/ \sqrt{\left(1+h_{ix}^2\right)} \right) \right]$ and $\mathbf{t}_i \left[\left(1 \Big/ \sqrt{\left(1+h_{ix}^2\right)}, h_{ix} \Big/ \sqrt{\left(1+h_{ix}^2\right)} \right) \right]$ are the outward normal and tangent vectors, respectively. The location of the liquid-liquid interface $\left(y = h_1 \right)$ is defined by the kinematic condition,

$$\dot{h}_1 = -u_1 \left(\partial h_1 / \partial x \right) + w_1 . \tag{4.12}$$

At free surface ($z = h_2$), the normal and tangential stress balances and the kinematic condition are enforced as boundary conditions,

$$\mathbf{n}_2 \cdot \bar{\boldsymbol{\tau}}_2 \cdot \mathbf{n}_2 = \gamma_2 \left(\nabla \cdot \mathbf{n}_2 \right), \tag{4.13}$$

$$\mathbf{t}_2 \cdot \bar{\boldsymbol{\tau}}_2 \cdot \mathbf{n}_2 = 0, \tag{4.14}$$

$$\dot{h}_2 = -u_2 \left(\partial h_2 / \partial x \right) + w_2 . \tag{4.15}$$

Here h_2 represents the combined thickness of the liquid layers, γ_2 represents the surface tension of the liquid-air interface.

Eqs. (4.1) – (4.15) are transformed into non-dimensional forms employing the base state lower film thickness (h_0) as length scale and $\rho_1 h_0^2 / \mu_1$ as the time scale. The resulting set of dimensionless variables are, $X = x / h_0$, $Z = z / h_0$, $D_m = d / h_0$, $H_1 = h_1 / h_0$, $H_2 = h_2 / h_0$, $T = t\mu_1 / \rho_1 h_0^2$, $\mathbf{U}_j = \mathbf{u}_j \rho_1 h_0 / \mu_1$, $\rho_r = \rho_2 / \rho_1$, $\mu_r = \mu_2 / \mu_1$, $h_r = \left(h_2 / h_1 \right) - 1$, $G = g h_0^3 / \nu_1^2$, $\Gamma_1 = \gamma_1 h_0 / \rho_1 \nu_1^2$, $\Gamma_2 = \gamma_2 h_0 / \rho_1 \nu_1^2$, $\Gamma_r = \Gamma_2 / \Gamma_1$ and $P_j = p_j h_0^2 \rho_1 / \mu_1^2$. In the following equations, the subscripts X and Z denote partial derivatives. At the base state, the lower, upper, and porous layers occupy, $0 \le Z \le H_1$, $H_1 \le Z \le H_2$ and $-D_m \le Z \le 0$, where H_1 and H_2 are the dimensionless positions of the liquid-liquid and liquid-air interfaces. The dimensionless continuity equations for the films and the porous layer are as follows,

$$U_{1X} + W_{1Z} = 0, \tag{4.16}$$

$$U_{2X} + W_{2Z} = 0, \tag{4.17}$$

$$U_{mX} + W_{mZ} = 0. \tag{4.18}$$

The *X*- and *Z*- components of the dimensionless momentum motions for the liquid and porous layers are,

$$\dot{U}_1 + U_1 U_{1X} + W_1 U_{1Z} = -P_{1X} + \left(U_{1XX} + U_{1ZZ} \right) + G \sin\alpha, \tag{4.19}$$

$$\dot{W}_1 + U_1 W_{1X} + W_1 W_{1Z} = -P_{1Z} + \left(W_{1XX} + W_{1ZZ} \right) - G \cos\alpha, \tag{4.20}$$

$$\rho_r\left(\dot{U}_2 + U_2 U_{2X} + W_2 U_{2Z}\right) = -P_{2X} + \mu_r\left(U_{2XX} + U_{2ZZ}\right) + \rho_r G\sin\alpha\,, \tag{4.21}$$

$$\rho_r\left(\dot{W}_2 + U_2 W_{2X} + W_2 W_{2Z}\right) = -P_{2Z} + \mu_r\left(W_{2XX} + W_{2ZZ}\right) - \rho_r G\cos\alpha\,, \tag{4.22}$$

$$\left(1/\delta\right)\dot{U}_m = -P_{mX} + \left(1/\delta\right)\left(U_{mXX} + U_{mZZ}\right) - \left(1/Da\right)U_m + G\sin\alpha\,, \tag{4.23}$$

$$\left(1/\delta\right)\dot{W}_m = -P_{mZ} + \left(1/\delta\right)\left(W_{mXX} + W_{mZZ}\right) - \left(1/Da\right)W_m - G\cos\alpha\,. \tag{4.24}$$

The no-slip and impermeability boundary conditions at the porous-solid interface $\left(Z = -D_m\right)$,

$$U_m = W_m = 0\,, \tag{4.25}$$

The continuity of *X*- and *Z*- components of velocities, the stress jump condition, and the normal stress balance at the porous-liquid interface $\left(Z = 0\right)$ are,

$$U_1 = U_m\,, \tag{4.26}$$

$$W_1 = W_m\,, \tag{4.27}$$

$$\left(1/\delta\right)U_{mZ} - U_{1Z} - \left(\chi/\sqrt{Da}\right)U_m = 0\,, \tag{4.28}$$

$$P_1 - P_m + 2\left(\left(1/\delta\right)W_{mZ} - W_{1Z}\right) = 0\,. \tag{4.29}$$

The continuity of velocities, normal and tangential stress balances, and the kinematic equation at the liquid-liquid interface $\left(Z = H_1\right)$ are,

$$U_1 = U_2\,, \tag{4.30}$$

$$W_1 = W_2\,, \tag{4.31}$$

$$P_2 - P_1 + \frac{2}{\left[1 + H_{1X}^2\right]}\left\{\begin{matrix}\left[\left(\left(1 - H_{1X}^2\right)W_{1Z} - H_{1X}\left(W_{1X} + U_{1Z}\right)\right)\right] - \\ \mu_r\left[\left(1 - H_{1X}^2\right)W_{2Z} - H_{1X}\left(W_{2X} + U_{2Z}\right)\right]\end{matrix}\right\} = \frac{\Gamma H_{1XX}}{\left[1 + H_{1X}^2\right]^{\frac{3}{2}}}\,, \tag{4.32}$$

$$\begin{bmatrix} \left[\left(U_{1Z}+W_{1X}\right)\left(1-H_{1X}^{2}\right)+2H_{1X}\left(W_{1Z}-U_{1X}\right)\right]- \\ \mu_r\left[\left(U_{2Z}+W_{2X}\right)\left(1-H_{1X}^{2}\right)+2H_{1X}\left(W_{2Z}-U_{2X}\right)\right] \end{bmatrix}=0, \tag{4.33}$$

$$\dot{H}_1=-U_1H_{1X}+W_1. \tag{4.34}$$

The normal and tangential stress balances, and the kinematic condition at the liquid-air interface $\left(Z=H_2\right)$ are,

$$-P_2+\frac{2\mu}{\left[1+H_{2X}^{2}\right]}\left\{\left[\left(\left(1-H_{2X}^{2}\right)W_{2Z}-H_{2X}\left(W_{2X}+U_{2Z}\right)\right)\right)\right]\right\}=\frac{\Gamma_2 H_{XX}}{\left[1+H_{2X}^{2}\right]^{\frac{3}{2}}}, \tag{4.35}$$

$$\left[\left(U_{2Z}+W_{2X}\right)\left(1-H_{X}^{2}\right)+2H_{X}\left(W_{2Z}-U_{2X}\right)\right]=0, \tag{4.36}$$

$$\dot{H}_2=-U_2H_{2X}+W_2. \tag{4.37}$$

In Eqs. (4.16) – (4.37), the parameters $Da=\kappa/h_0^2$, $\chi=\xi/\mu_1$, G, and $\Gamma_j=\gamma_j h_0/\rho_1\nu_1^2$ denote Darcy number, dimensionless stress jump coefficient, Galileo number, and Capillary number, respectively. In the following sections, unless mentioned the discussions are carried out in terms of the non-dimensional variables.

4.3 BASE STATE

The governing equations and the boundary conditions are simplified with the following variables for the unperturbed interfaces to obtain the base state solutions of the *x*-directional flow,

$$H_1=1,\ H_2=\bar{H}_2, \bar{W}_j=0 \text{ and } U_j=\bar{U}_j(Z)\ (j = 1, 2, \text{and } m). \tag{4.39}$$

The over-bars indicate base state solutions.

The expressions for the velocity profiles for the base state are,

$$\bar{U}_1=C_{11}Z^2+C_{12}Z+C_{13},\quad 0\le Z\le 1, \tag{4.40}$$

$$\bar{U}_2 = C_{21} Z^2 + C_{22} Z + C_{23}, \quad 1 \le Z \le H_2 , \tag{4.41}$$

$$\bar{U}_m = C_{m1}\, \mathrm{e}^{MZ} + C_{m2}\, \mathrm{e}^{-MZ} + C_{m3}, \quad -D_m \le Z \le 0 . \tag{4.42}$$

Here $\bar{U}_1$, $\bar{U}_2$, and $\bar{U}_m$ represent the base state velocities at the lower, upper, and porous layers, respectively, and $M = \sqrt{\delta / Da}$. A brief derivation of the base state equations and the expressions for the constants C_{ij} (i = *1*, *2* and *m*; j = *1*, *2*, and *3*) in the equations (4.40) – (4.42) are shown in the Appendix C.

Figure 4.2 summarizes the base state velocity profiles under varied conditions. The plot (a) shows with increase in porosity (δ), the flow in the porous layer becomes stronger, which in turn induces a larger slippage at the porous-liquid interface. In consequence, the liquid layers flows at a faster rate as compared to the free bilayers on a non-slipping and impervious substrate. Plot (b) shows that the thickness of the porous layer can also impart slippage to the porous-liquid interface until a threshold thickness. The curves corresponding to D_m = 1.0 and 2.0 show that beyond a threshold value, the flow in the liquid layers is hardly influenced by the increase in the porous layer thickness. Permeability in the porous layer is another parameter that can enhance the inertial influence to the liquid layers, as shown by the image (c). The curves in this figure show that the flow inside the porous layer becomes stronger with an increase in *Da*. The plots (a) – (c) clearly indicate that for the free bilayers with equal density and with less viscous fluids adjacent to the porous media the presence of an underlying porous layer can enhance the inertial influence, which can significantly expedite the flow rate in the liquid layers.

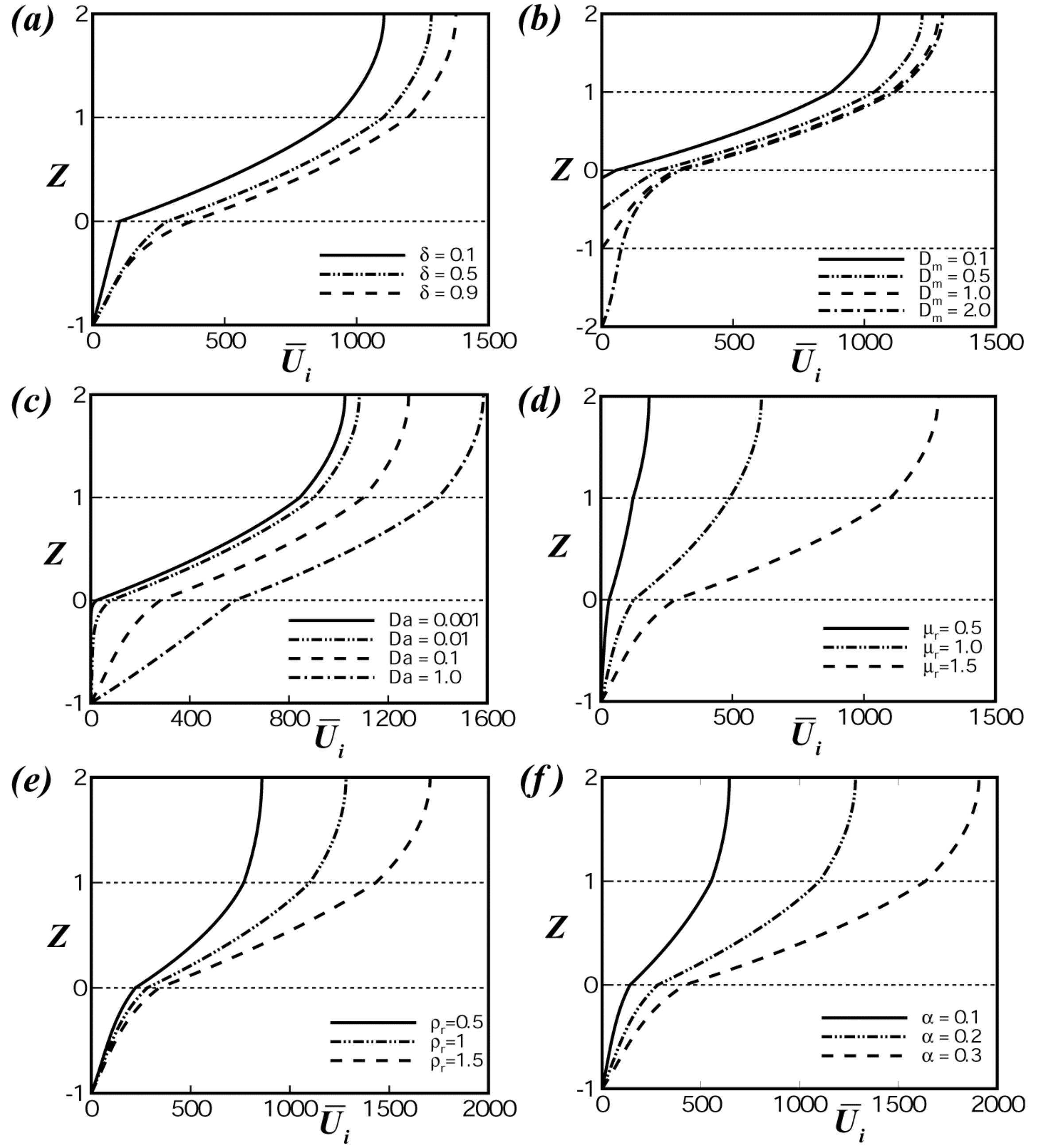

Figure 4.2: Plots show the non-dimensional base state velocity ($\bar{U}_i$) profiles across the width of the channel (Z) when $h_r = 1$. The curves in plots (a) – (f) correspond to different δ, D_m, Da, μ_r, ρ_r and α, respectively. The other parameters are kept fixed at $\delta = 0.5$, $D_m = 1$, $Da = 0.1$, $\rho_r = 1$, $\mu_r = 1.5$, $\Gamma_1 = 8 \times 10^3$, $\Gamma_2 = 15 \times 10^3$ and $\alpha = 0.2$.

The plots (d) and (e) show that when the density of the liquid layer are kept the same, the flow rate in the liquid and porous layers are more when a less viscous fluid is adjacent to the porous layer than when a more viscous fluid is near the porous layer. Also, the flow rate is more when the lower liquid layer close to porous layer has less density and less viscosity than the upper fluid layers, as shown in plot (e). It may be noted here that for free bilayers, the location of maximum velocity is always at the liquid-air interface, even when the bilayer is composed of a denser or a more viscous upper layer (solid lines). Plot (f) shows that increase in the angle of inclination can intensify the flow inside the porous and liquid layers. Again, the plots (d) – (f) confirm that the presence of porous layer always strengthens the slippage at the porous-liquid interface even when the porous layer properties are kept fixed and the viscosity or density ratio or the angle of inclination is increased. Importantly, the slippage at the porous-liquid interface is found to be larger when the lower layer has less density and viscosity. The observations on the base state velocity profiles with various parameters will be of help while discussing the results in the following sections.

4.4 LINEAR STABILITY ANALYSIS

The Eqs. (4.16) – (4.37) are linearized using following perturbations to the base state solutions, $U_j = \bar{U}_j + U'_j$, $W_j = W'_j$, and $P_j = \bar{P}_j + P'_j$. The primes denote perturbed quantities in which the velocity perturbations are transformed into the stream functions as, $U'_j = \partial\Psi_j/\partial Z$ and $W'_j = -\partial\Psi_j/\partial X$. The normal modes, $\Psi_j(X,Z,T) = \tilde{\Psi}_j(Z)e^{\mathbf{i}K(X-CT)}$, $P'_j(X,Z,T) = \tilde{P}_j(Z)e^{\mathbf{i}K(X-CT)}$, and $H_j(X,Z,T) = 1 + \tilde{H}_j e^{\mathbf{i}K(X-CT)}$, are employed to linearize the governing equations to obtain the following coupled O-S equations for the films and the porous layer,

$$\left(D^2 - K^2\right)^2 \tilde{\Psi}_1 = \mathbf{i}K\left[\left(\bar{U}_1 - C\right)\left(D^2 - K^2\right) - D^2\bar{U}_1\right]\tilde{\Psi}_1, \qquad (4.43)$$

$$\nu_r \left(D^2 - K^2\right)^2 \tilde{\Psi}_2 = \mathbf{i}K\left[\left(\bar{U}_2 - C\right)\left(D^2 - K^2\right) - D^2\bar{U}_2\right]\tilde{\Psi}_2, \tag{4.44}$$

$$\left(D^2 - K^2\right)^2 \tilde{\Psi}_m = \left(\delta / Da - \mathbf{i}KC\right)\left(D^2 - K^2\right)\tilde{\Psi}_m. \tag{4.45}$$

Here the notation D and subscript Z represent the differentiation d/dZ, $\nu_r\left(= \mu_r / \rho_r\right)$, and K is the wavenumber, and C $(= C_r + \mathbf{i}C_i)$ is the phase speed. The variables C_r and C_i are the real and imaginary parts of the phase speed, respectively. The linearized boundary conditions at the porous-solid boundary are,

$$\tilde{\Psi}_{mZ}(-D_m) = \tilde{\Psi}_m(-D_m) = 0. \tag{4.46}$$

The linearized boundary conditions at the porous-liquid interface (Z = 0) are,

$$\tilde{\Psi}_1 = \tilde{\Psi}_m, \tag{4.47}$$

$$\tilde{\Psi}_{1Z} = \tilde{\Psi}_{mZ}, \tag{4.48}$$

$$\frac{1}{\delta}\tilde{\Psi}_{mZZ} - \tilde{\Psi}_{1ZZ} = \frac{\chi}{\sqrt{Da}}\tilde{\Psi}_{mZ}, \tag{4.49}$$

$$\begin{aligned} &iK\bar{U}_{1Z}\tilde{\Psi}_1 + \left[-3K^2 + iK\left(C - \bar{U}_1\right)\right]\tilde{\Psi}_{1Z} + \tilde{\Psi}_{1ZZZ} \\ &= \frac{1}{\delta}\left[-3K^2 - \frac{\delta}{Da} + iKC\right]\tilde{\Psi}_{mZ} + \frac{1}{\delta}\tilde{\Psi}_{mZZZ}\ . \end{aligned} \tag{4.50}$$

The expressions for the linearized boundary conditions at the liquid-liquid interface (Z = 1) are given by,

$$\tilde{H}_1 = \tilde{\Psi}_1 / \left(C - \bar{U}_1\right), \tag{4.51}$$

$$\tilde{\Psi}_1 = \tilde{\Psi}_2, \tag{4.52}$$

$$\left(\tilde{\Psi}_{1Z} - \tilde{\Psi}_{2Z}\right) + \left[\tilde{\Psi}_1 / \left(C - \bar{U}_1\right)\right]\left(\bar{U}_{1Z} - \bar{U}_{2Z}\right) = 0, \tag{4.53}$$

$$\begin{aligned}&\tilde{\Psi}_{1ZZZ}-3K^2\tilde{\Psi}_{1Z}-\mu_r\tilde{\Psi}_{2ZZZ}+3\mu_r K^2\tilde{\Psi}_{2Z}+iK\left(C-\bar{U}_1\right)\left(\tilde{\Psi}_{1Z}-\rho_r\tilde{\Psi}_{2Z}\right)\\&+iK\left(\bar{U}_{1Z}\tilde{\Psi}_1-\rho_r\bar{U}_{2Z}\tilde{\Psi}_2\right)-\tilde{\Psi}_1/\left(C-\bar{U}_1\right)\left[\left(\bar{U}_{1Z}-\mu_r\bar{U}_{2Z}\right)2K^2+i\Gamma K^3\right]=0,\end{aligned}\tag{4.54}$$

$$\left[\tilde{\Psi}_{1ZZ}+K^2\tilde{\Psi}_1\right]+\left(\bar{U}_{1ZZ}-\mu_r\bar{U}_{2ZZ}\right)\tilde{\Psi}_1/\left(C-\bar{U}_1\right)-\mu_r\left[\tilde{\Psi}_{2ZZ}+K^2\tilde{\Psi}_2\right]=0.\tag{4.55}$$

The linearized boundary conditions at the free-surface $\left(Z=H_2\right)$ are obtained as,

$$\tilde{H}_2=\tilde{\Psi}_2/\left(C-\bar{U}_2\right),\tag{4.56}$$

$$\begin{bmatrix}3\mu_r K^2\tilde{\Psi}_{2Z}-\mu_r\tilde{\Psi}_{2ZZZ}-iK\rho_r\left[\bar{U}_{2Z}\tilde{\Psi}_2+\tilde{\Psi}_{2Z}\left(C-\bar{U}_2\right)\right]\\+\tilde{\Psi}_2/\left(C-\bar{U}_2\right)\left[ik^3\Gamma_2+2\mu_r K^2\bar{U}_{2Z}\right]\end{bmatrix}=0,\tag{4.57}$$

$$\left[\tilde{\Psi}_{2ZZ}+K^2\tilde{\Psi}_2\right]+\left(\bar{U}_{2ZZ}\right)\tilde{\Psi}_2/\left(C-\bar{U}_2\right)=0.\tag{4.58}$$

4.5 NUMERICAL METHOD

The eigenvalue problem in Eqs. (4.43) – (4.58) is solved numerically to obtain the linear growth rate (KC_i) and wavenumber (K) for the unstable modes. The accurate D^2 algorithm for Chebyshev-tau QZ spectral method is employed to obtain the eigenvalues.[22,93,94] To implement this method the computational domain is mapped into (-1, 1) using the transformations $Z_1=-2Z+1$, $Z_2=\dfrac{2}{H_2-1}Z-\dfrac{H_2+1}{H_2-1}$, and $Z_m=\dfrac{2}{D_m}Z+1$, for the lower, upper, and the porous layers, respectively. Thereafter, the 4th order ODEs (4.43) – (4.45) are transformed into six 2nd order ODEs for ξ, λ, and ϑ with $\eta\left(Z_1\right)=\tilde{\Psi}_1\left(Z\right)$, $\sigma\left(Z_2\right)=\tilde{\Psi}_2\left(Z\right)$, and $\zeta\left(Z_m\right)=\tilde{\Psi}_m\left(Z\right)$ where $L_1\eta\equiv\left(4d^2/dZ_1^{\,2}-K^2\right)\eta=\xi$, $L_2\sigma\equiv\left(\left(4/(H_2-1)^2\right)d^2/dZ_2^{\,2}-K^2\right)\sigma=\lambda$,and $L_m\zeta\equiv\left(\left(4/D^2\right)d^2/dZ_m^{\,2}-K^2\right)\zeta=\vartheta$. The equation are obtained are,

$$L_1\eta-\xi=0, \tag{4.59}$$

$$L_1\xi-iK\bar{U}_1\xi+2iKC_{11}\eta+iKC\xi=0, \tag{4.60}$$

$$L_2\sigma-\lambda=0, \tag{4.61}$$

$$\nu_r L_2\lambda-iK\bar{U}_2\lambda+2iKC_{21}\sigma+iKC\lambda=0, \tag{4.62}$$

$$L_m\zeta-\vartheta=0, \tag{4.63}$$

$$L_m\vartheta-\frac{\delta}{Da}\vartheta+iKC\vartheta=0. \tag{4.64}$$

The boundary conditions at the porous-solid boundaries in terms of the above variables,

$$\zeta_{Zm}(-1)=\zeta(-1)=0. \tag{4.65}$$

and the boundary conditions at the porous-liquid interface are,

$$\eta-\zeta=0, \tag{4.66}$$

$$\eta_{Z1}+\frac{1}{D}\zeta_{Zm}=0, \tag{4.67}$$

$$K^2\eta+\xi-\frac{K^2}{\delta}\zeta+\frac{2\chi}{D\sqrt{Da}}\zeta_{Zm}-\frac{1}{\delta}\vartheta=0, \tag{4.68}$$

$$\begin{bmatrix} iKC_{12}\eta+2\left(2K^2+iK\bar{U}_1\right)\eta_{Z1}-2\xi_{Z1}+\dfrac{2}{\delta D}\left[2K^2+\dfrac{\delta}{Da}\right]\zeta_{Zm} \\ -\dfrac{2}{\delta D}\vartheta_{Zm}-C\left(2iK\eta_{Z1}+\dfrac{2iK}{\delta D}\zeta_{Z1}\right) \end{bmatrix}=0. \tag{4.69}$$

At the liquids-liquid interface,

$$\eta-\sigma=0, \tag{4.70}$$

$$\begin{bmatrix} C\left(2\eta_{Z1}+\left(2/H_2-1\right)\sigma_{Z2}\right)-\left(\left(2C_{11}+C_{12}\right)-\left(2C_{21}+C_{22}\right)\right)\eta \\ -2\bar{U}_1\eta_{Z1}-\left(2\bar{U}_1/H_2-1\right)\sigma_{Z2} \end{bmatrix}=0, \tag{4.71}$$

$$\begin{bmatrix} C\left(2K^2\eta+\xi-2\mu_r K^2\sigma-\mu_r\lambda\right)+2\left(\left(C_{11}-\mu_r C_{21}\right)-\bar{U}_1K^2\right)\eta \\ -\bar{U}_1\xi+2\mu_r\bar{U}_1K^2\sigma+\mu_r\bar{U}_1\lambda \end{bmatrix}=0\,, \tag{4.72}$$

$$\begin{aligned} & C^2\left(2iK\eta_{Z1}+\left(2iK\rho_r/H_2-1\right)\sigma_{Z2}\right) \\ & +C\begin{pmatrix} -iK\left(2C_{11}+C_{12}\right)\eta-4\left(iK\bar{U}_1+K^2\right)\eta_{Z1}+2\xi_{Z1}+iK\rho_r\left(2C_{21}+C_{22}\right)\sigma \\ -\left(4/H_2-1\right)\left(\mu_r K^2+iK\rho_r\bar{U}_1\right)\sigma_{Z2}+\left(2\mu_r/\left(H_2-1\right)\right)\lambda_{Z2} \end{pmatrix} \\ & +\begin{bmatrix} \left[2\left(\left(2C_{11}+C_{12}\right)-\mu_r\left(2C_{21}+C_{22}\right)\right)K^2+iK\bar{U}_1\left(2C_{11}+C_{12}\right)+i\Gamma K^3\right]\eta \\ +2\left(2\bar{U}_1K^2+iK\bar{U}_1^{\,2}\right)\eta_{Z1}-2\bar{U}_1\xi_{Z1}-iK\bar{U}_1\rho_r\left(2C_{21}+C_{22}\right)\sigma \\ +\left(2/\left(H_2-1\right)\right)\left[2\mu_r\bar{U}_1K^2+iK\rho_r\bar{U}_1^{\,2}\right]\sigma_{Z2}-\left(2\mu_r\bar{U}_1/\left(H_2-1\right)\right)\lambda_{Z2} \end{bmatrix}=0 \end{aligned} . \tag{4.73}$$

and the boundary conditions at the liquid-air interface are,

$$C\left(\lambda+2K^2\sigma\right)-\bar{U}_2\lambda+2\left(\bar{U}_2K^2-C_{21}\right)\sigma=0\,, \tag{4.74}$$

$$\begin{aligned} & C^2\left(-2iK\rho_r/\left(H_2-1\right)\right)\sigma_{Z2} \\ & +C\begin{pmatrix} -iK\rho_r\left(2BC_{21}+C_{22}\right)\sigma+\left(\left(4\mu_r K^2+2iK\rho_r\bar{U}_2\right)2/\left(H_2-1\right)\right)\sigma_{Z2} \\ -2\mu_r/\left(H_2-1\right)\lambda_{Z2} \end{pmatrix} \\ & +\begin{bmatrix} \left(\left(iK\rho_r\bar{U}_2+2\mu_r K^2\right)\left(2H_2C_{21}+C_{22}\right)+iK^3\Gamma_2\right)\sigma \\ -\left[\left(iK\rho_r\bar{U}_2^{\,2}+4\mu_r\bar{U}_2K^2\right)2/\left(H_2-1\right)\right]\sigma_{Z2}+\left(2\mu_r\bar{U}_2/\left(H_2-1\right)\right)\lambda_{Z2} \end{bmatrix}=0 \end{aligned} . \tag{4.75}$$

The subscripts *Z*1, *Z*2, and *Zm* denote ordinary differentiation. The Eqs. (4.59) – (4.75) are then expanded in terms of Chebyshev polynomials $T_n(z)$. For a Chebyshev polynomial with *N* terms, the eigenvalues are obtained from a (6*N*+12) × (6*N*+12) matrix corresponding to six ODEs and twelve boundary conditions. The accuracy of the eigenvalues is ensured by increasing the number of polynomials and then eliminating the spurious eigenvalues. The eigenvalues are verified by solving Eqs. (4.59) – (4.75) employing spectral collocation method with enhanced accuracy.[95] Figure 4.3(a) shows the typical linear growth rate (KC_i) vs. wavenumber (*K*) plot for a free bilayer where the eigenvalues are predicted with equal accuracy by both spectral collocation and Chebyshev-tau QZ algorithm.

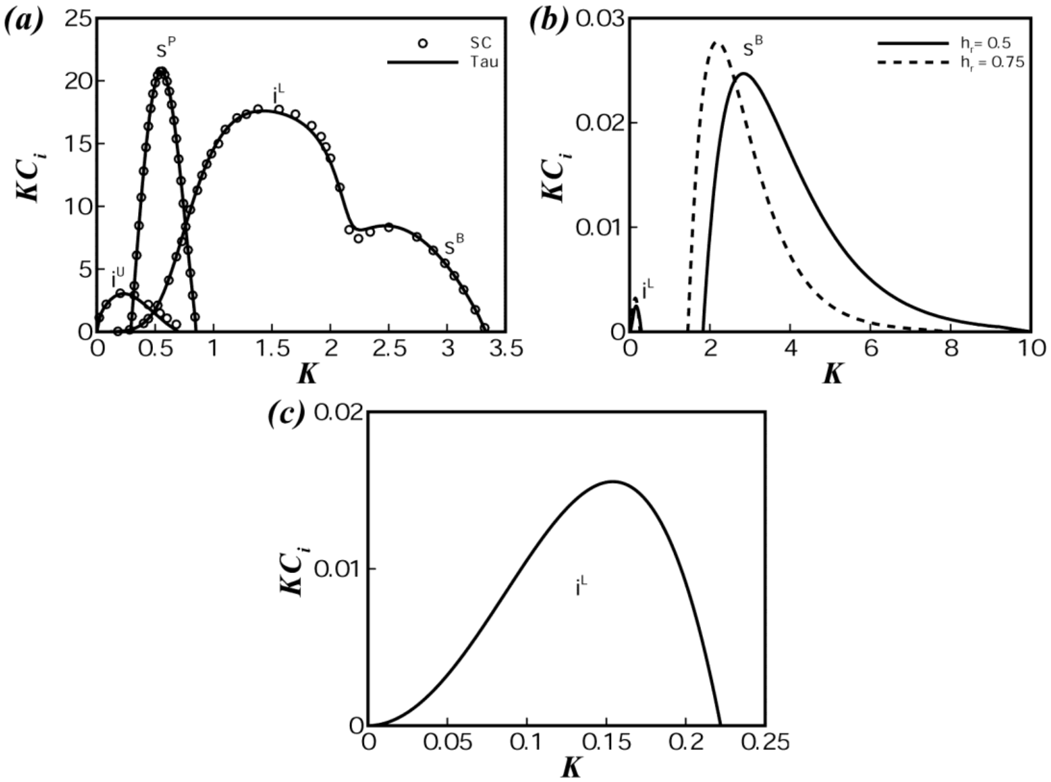

Figure 4.3: Plot (a) shows the variation of growth rate (KC_i) with wavenumber (K).In plot (a) δ = 0.5, D_m= 1, Da = 5×10^{-3}, h_r = 1.5, ρ_r = 1, μ_r = 0.9, Γ_1 = 8 × 10^3, Γ_2 = 15 × 10^3, and α=0.2. The solid line (dots) shows the result from the Chebyshev-tau QZ (spectral collocation) method. The curve i^U represents the surface mode at free-surface. i^L represents the interfacial mode at liquid-liquid interface, s^P represents porous media shear mode, and s^B represents shear mode. Plot (b) gives growth rate for different h_r when μ_r = 2.5, ρ_r =1, δ = 0.01, D_m = 0.01, Da = 0.1, Γ_1 = 0, Γ_2 = 0,and α=0.2.For plot (c) δ = 0.3, D_m= 0.3, Da = 0.2, h_r = 0.05, ρ_r = 1, μ_r = 1, Re = 1,and cot α= 1.

In Figure 4.3(b), we reproduce a pair of linear growth rate (KC_i) vs. wavenumber (K) plot for a free bilayer flowing on a nearly non-slipping and impervious substrate[51] in the limit where the effects of the porous layer is rather trivial. In Figure 4.3(c), we asymptotically recover a KC_i vs. K plot for single layer flow over porous medium under similar conditions.[74] Figure 4.3 corroborates the accuracy of the codes employed to predict the eigenvalues employed in this study. In what follows, we employ the Chebyshev-tau QZ algorithm to report the results under varied conditions. The eigenfunctions corresponding to the eigenvalues are obtained employing the spectral collocation method.

4.6. RESULTS AND DISCUSSION

Figure 4.1 schematically shows a thin free bilayer flowing on an inclined porous medium. In absence of the porous layer, the interfaces in a free bilayer flow over an impervious substrate can be unstable by interfacial modes originating from the viscosity and density stratifications across the twin liquid-liquid and liquid-air interfaces.[48-53]

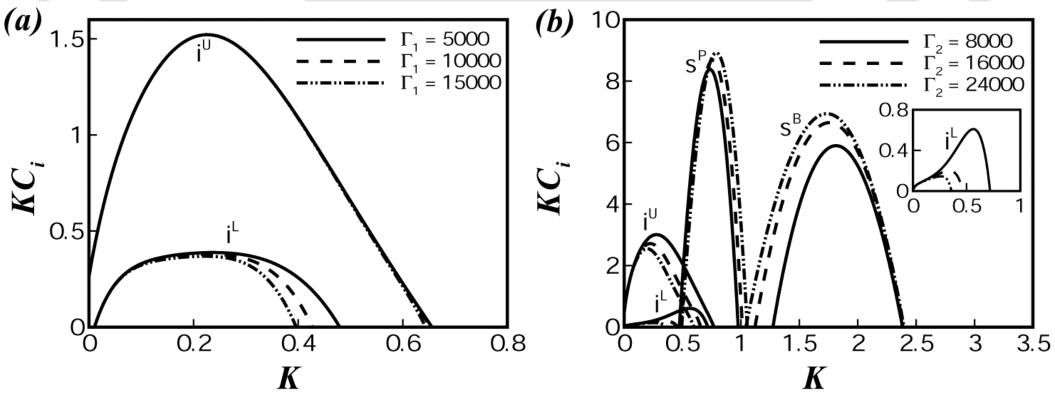

Figure 4.4: Plots show the variations of growth rate (KC_i) with wavenumber (K). The curve i^U represents the interfacial mode at free surface. i^L represents the interfacial mode at liquid-liquid interface, s^P represents porous media shear mode, and s^B represents shear mode. The curves in plot (a) corresponds to different Γ_1 when μ_r = 0.5 and $\Gamma_2 = 15 \times 10^3$. The curves in plot (b) corresponds to different values of Γ_2 when μ_r = 0.9 and $\Gamma_1 = 8 \times 10^3$. The other parameters are kept fixed at δ = 0.5, $D_m = 1$, $Da = 5\times10^{-3}$, $\rho_r = 1$, $h_r = 1$, and $\alpha = 0.2$.

At higher flow rates, the increasing influence of the inertial forces can also engender finite-wavenumber shear modes.[20] In what follows, we discuss the fate of these modes under the influence of porous layer parameters. We also explore the possibility of new unstable modes that are specific to the presence of the porous layer. The coupled deformable free-surface and interface of a bilayer can show twin interfacial modes of instabilities under the influence of small amplitude perturbation. Depending on the magnitude of the surface (interfacial) tension at the free-surface (interface) the wavelengths of these modes can vary. Further, the strongly coupled interfaces can evolve in a single wavelength whereas a weak coupling between the interfaces can engender different wavelengths of interfacial deformations. The growth rate (KC_i) vs. wavenumber (K) plots in Figure 4.4 indicate the presence of multiple interfacial modes, i^L and i^U. Here the superscripts 'L' and 'U' correspond to the interfacial mode corresponding to lower liquid-liquid and upper liquid-air interface. The interfacial modes are differentiated based on the phase speed of the unstable interfacial modes corresponding to the base state velocities at the interfaces.[50-59] Plot (a) shows that when the more viscous film is adjacent to the wall the bilayer is unstable by a dominant i^U mode and a sub-dominant i^L mode. Interestingly, the curves in this plot also show that at a fixed Γ_2, increase in Γ_1 leads to the reduction in the growth coefficient and increase in the wavelength of i^L interfacial mode whereas the i^U mode remains almost insensitive to this change.

The plots also suggest that more the surface and the interfacial tensions are similar a stronger coupling between the interfaces take place as they evolve after attaining a similar wavelength. Plot (b) also shows that the change in the surface tension has profound influence on both the interfacial modes. However, under this condition the dominant wavelength of instability for the interfacial modes are found to be very different signifying a decoupling of the unstable modes. The plot (b) in Figure 4.4 also confirms the presence of a pair of finite wavenumber s^B and s^P shear modes in addition to the interfacial modes in which the surface tension at the free surface is found to have more influence on the s^B mode. The superscripts here identify one conventional shear mode (s^B), which is commonly observed for bilayers on non-porous surfaces and the other one appears (s^P) when the porous layer is present. The origin of these two modes is discussed in the following section through an eigenfunction analysis.

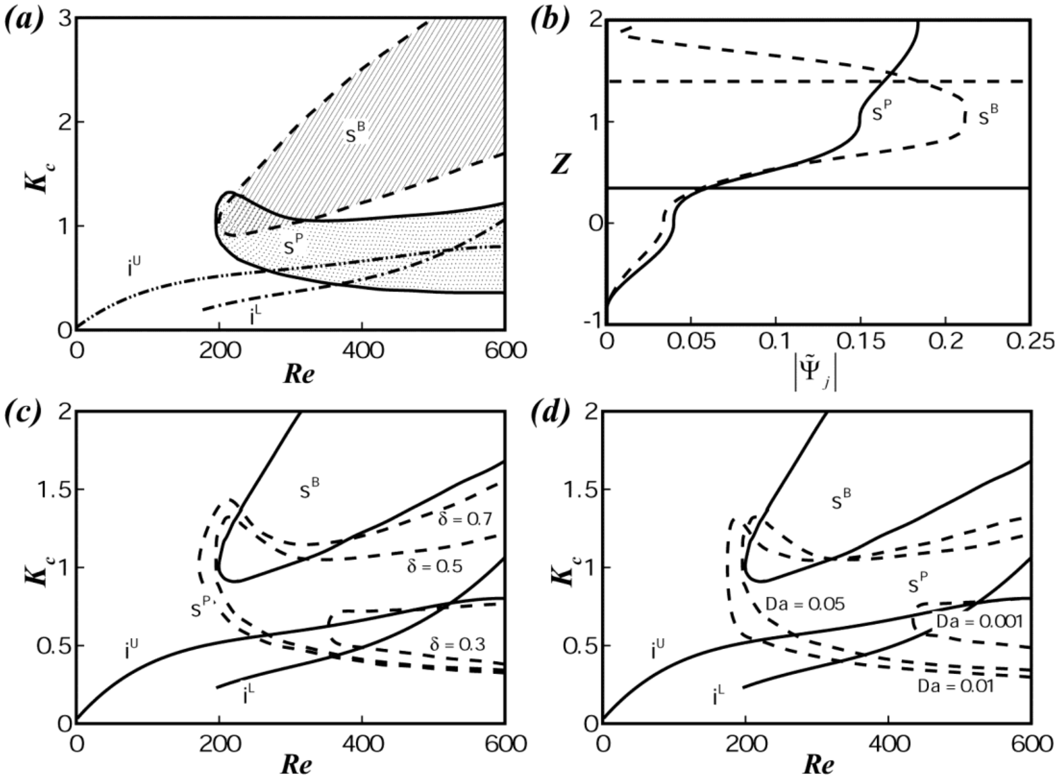

Figure 4.5: The plot (a), (c), and (d) show the neutral stability curves. Plot (b) shows the eigenvectors for the s^P and s^B modes at K = 0.8 and 1.5, respectively, when $\alpha = 0.16$ (Re = 312). The broken curves in the plot (c) shows the neutral stability plots with the variation in porosity (δ) and plot (d) shows the same with the variation in Darcy number (Da). The solid lines in the plots (c) and (d) show the other modes. The other parameters chosen for the plots are, $\delta = 0.5$, $D_m = 1$, $Da = 5\times10^{-3}$, $\rho_r = 1$, $\mu_r = 0.9$, $h_r = 1$, $\Gamma_1 = 8\times10^3$, and $\Gamma_2 = 15\times10^3$.

A free bilayer composed of a pair of immiscible phases such as oil and water can be made unstable on a porous layer when the angle of inclination is progressively increased. In such a situation, we can anticipate the appearance of the different instability modes as the flow inside the configuration becomes stronger as the angle of inclination is increased. Figure 4.5a shows the neutral stability curves in the $K_c - Re$ parametric regime for the different instability modes of a free bilayer flowing on a porous medium having constant porosity, permeability and thickness. In this figure, the area under the curves for the interfacial modes and the shaded area enclosed by the curves for the shear modes show the unstable wavenumbers. The curves suggest that the i^U mode can appear even when the configuration is marginally inclined whereas the i^L mode appears only beyond a critical value of Re = 48. The unevenly broken lines confirm the long-wave nature ($KC_i \rightarrow 0$ as $K \rightarrow 0$) for these interfacial modes, which also shows a larger span of unstable wavenumbers at a higher Re. The hashed (shaded) area encompassed by the evenly broken (solid) curve suggests that the finite-wavenumber s^P (s^B) shear mode can appear at a larger threshold value of Re (for s^P mode Re = 175; s^B mode Re = 207) when the relatively stronger inertial effects start alleviating the viscous influences. The span of unstable wavenumbers for the s^B and s^P shear modes grows with the increase in Re. The s^B mode destabilizes shorter wavelength modes as compared to the other modes. The curves in the Figure 4.5(a) reflect that if the flow rate in an oil-water free bilayer is progressively increased the most dangerous is the i^U mode, as it appears at the lowest Re. All the other modes appear at a higher Re and can influence the flow stability in the nonlinear regime, which cannot be unveiled through the present analysis. However, the experiments on the free bilayer flows on a porous medium can also be performed by coating a pair of polymeric films on a porous surface and then heating them well above the glass transition temperature to stimulate flow. In such a situation, the experiments can be initiated with a fixed angle of inclination before the polymer films start moving due to the external heating and i^L, s^B, and s^P modes can be observed at fixed values of *Re*. Importantly, for a fixed *Re* the primary mode of instability will be the one growing fastest among all the unstable modes.

Figure 4.5(b) helps in identifying the location of the shear modes through the eigenvectors. While the interfacial modes are always expected to reside in the respective interfaces, the horizontal solid and broken lines show the critical layers corresponding to the s^P and s^B modes, respectively. The solid and broken lines showing the eigenfunctions together with the location of the critical layers confirm the place of the s^B mode in the upper layer whereas the same of the s^P mode at the lower layer, near the porous-liquid interface. Previous works on the free bilayers flowing over non-slipping and impermeable surfaces report the presence of i^U, i^L, and s^B modes.[52, 58] The additional s^P mode at the lower layer originates from the larger flow inside the porous layer. Interestingly, the neutral stability plots in Figure 4.5(c) and 4.5(d) show that increase in the porosity (δ) and permeability (*Da*) of the porous medium can only influence the s^P mode to originate at a much lower *Re* while the neutral stability plots for the other modes remain almost invariant. Larger porosity and permeability can allow a stronger flow inside the porous medium even at a smaller inclination (α), which helps the s^P mode to appear at a much lower value of *Re*. The span of unstable wavenumber for the s^P mode is also found to increase with *Re* especially in the shorter wavelength regime.

Briefly, Figures 4.4 and 4.5 confirm the presence of a pair of interfacial and shear modes for a free bilayer flowing over inclined porous medium in which the interfacial modes are located at the interfaces and the shear s^P and s^B modes are located inside the bulk of the lower and upper layers.

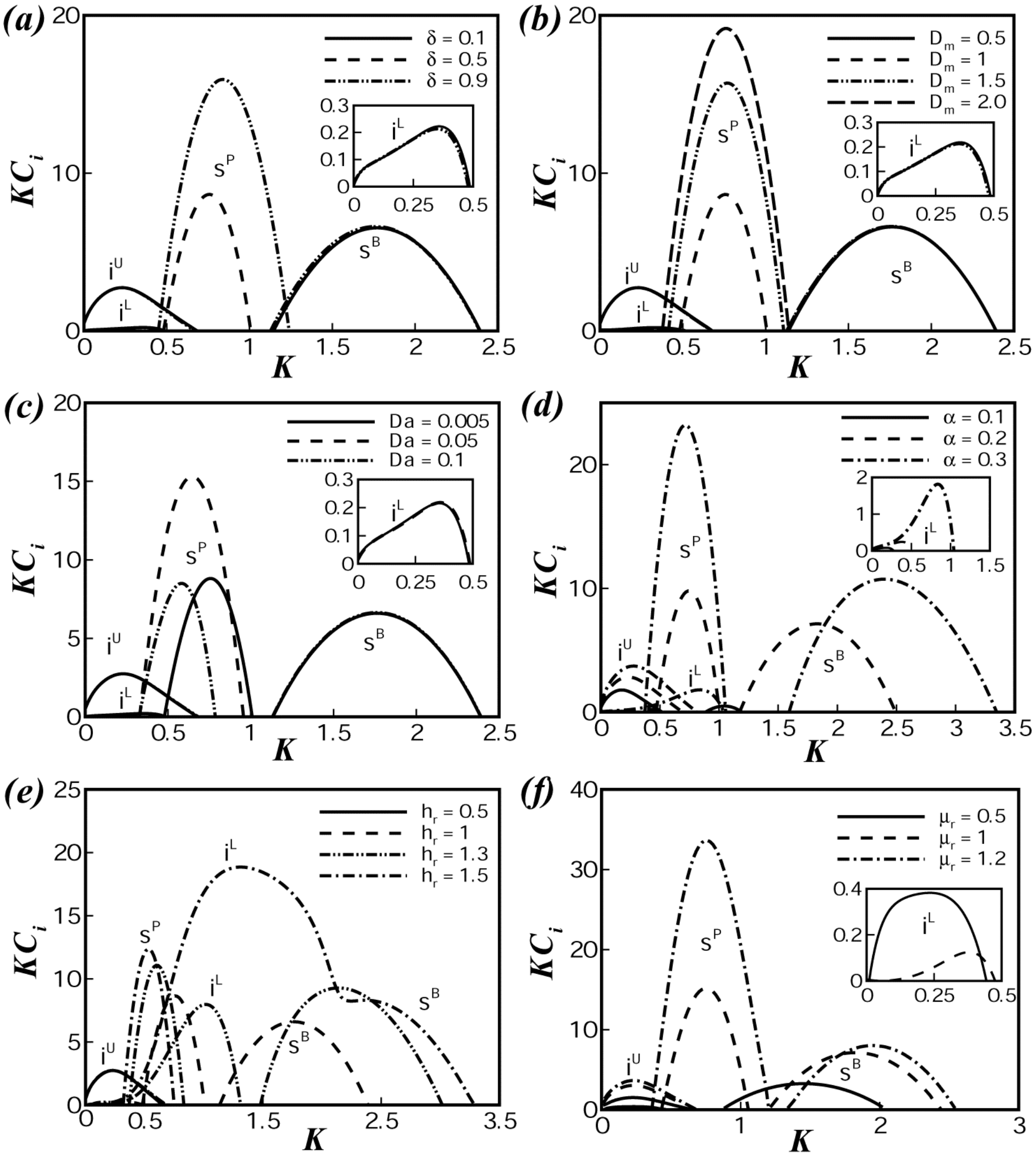

Figure 4.6: Plots show the variation of growth rate (KC_i) with wavenumber (K). The curves in plots (a) – (f) correspond to different δ, D_m, Da, α, h_r and μ_r, respectively. The other parameters are kept fixed at $\delta = 0.5$, $D_m = 1$, $Da = 5\times10^{-3}$, $\rho_r = 1$, $\mu_r = 0.9$, $h_r = 1$, $\Gamma_1 = 8 \times 10^3$, $\Gamma_2 = 15 \times 10^3$ and $\alpha = 0.2$.

The plots suggest that the liquid-air interface is unstable due to the long-wave i^{U} mode even when the free bilayer is marginally inclined. In contrast, the liquid-liquid interface shows an interfacial mode of instability (i^{L} mode) at a much larger inclination owing to the lack of viscosity or density stratification across the interface. The shear modes only appear when the flow inside the liquid layers is much stronger and the frictional influences at the layers are progressively reduced by the relatively larger inertial effects. The s^{B} mode is found to appear at the upper layer near the liquid-air interface because of the weak frictional influence at that location. In comparison, the flow inside porous layer allows a strong slippage at the porous-liquid interface, which promotes an entirely new s^{P} mode at the lower layer. It may be noted here that for a free bilayer on a non-slipping and impermeable surface never shows the s^{P} mode because of the stronger frictional influence on the lower layer from the rigid and impermeable wall. In contrast, the presence of the porous-layer significantly reduces the frictional influence especially at higher values of porosity, thickness and permeability, which stimulates the appearance of the s^{P} mode beyond a critical value of *Re*.

Plots (a) – (f) in Figure 4.6 show the variations in the linear growth coefficient (KC_i) with wavenumber (*K*) at different δ, D_m, *Da*, *α*, h_r, and μ_r, respectively. The solid line in the plot (a) shows that when the porosity is small the bilayer can be unstable by a pair of long-wave interfacial modes (curve i^{U} and curve i^{L} in the inset) together with a finite-wavenumber shear mode (s^{B}). It may be noted here that the free-surface has larger surface tension as compared to the liquid-liquid interface, which ensures that the i^{L} mode shows a maximum at higher wavenumber (smaller wavelength) as compared to the i^{U} mode. Interestingly, the i^{U} mode is the dominant one owing to the lack of density stratification and very low viscosity stratification across the liquid-liquid interface when $\rho_r = 1$, $\mu_r = 0.9$ leads to a very weak i^{L} mode as discussed earlier. The origin of the finite wavenumber shear mode s^{B} can be attributed to the flow inside the bilayer due to the inclination, as discussed in the previous figure. Plot (a) also shows that in such a configuration, when the porosity of the porous layer is progressively increased a new finite-wavenumber s^{P} mode appears (broken curves).

In fact, the s^{P} mode can even be the dominant one when the free bilayer flows over a porous layer with very high porosity. The origin of this new porous-media s^{P} mode can be attributed to the augmented inertia at the liquid layers owing to the larger slippage at the porous-liquid interface, as previously observed in the base state velocity profiles.

The broken lines in the plot (b) show that the s^{P} mode also gains strength with the increase in the porous layer thickness (D_m). However, the influence of the porous layer thickness is limited to a cut-off value beyond which the flow becomes independent of porous layer thickness, as observed previously in the Figure 4.2(b). Interestingly, increase in the permeability of the porous layer (Da) increases the strength of the s^{P} mode until a critical value as shown by the solid and the evenly broken lines in plot (c). However, beyond the critical value a larger flow in the porous layer again decreases the strength of the s^{P} mode, as shown by the evenly and unevenly broken lines in the plot (c). Thus, with the change in permeability the s^{P} mode is found to dominate only for a window of Da and remain sub-dominant or absent otherwise. Plot (d) shows that when the angle of inclination (α) of the substrate increases, all the interfacial and shear modes gain strength. This is in contrast to the plots (a) – (c) where the porous media parameters could only influence the growth coefficient corresponding to the s^{P} mode and other instability modes remained dormant to the same influences. Interestingly, plot (d) uncovers that although increase in α increases the strength of all the i^U , i^L , and s^B but it has more profound impact on the s^P mode, as it is observed to be the dominant mode at higher inclinations even at a moderately high porosity (δ = 0.5). Previously, in Figure 4.2(f) it was shown that the slippage at the porous-liquid interface increases with the increase in α which in turn helps the s^P mode to gain dominance over the other modes especially at the higher values of α. Plot (e) shows another interesting scenario where the ratio of the upper to lower film thickness (h_r) is varied. When the upper layer is thin (solid line) we observe the presence of a dominant i^U mode. With increase in the upper layer thickness the s^B, i^L, and the s^P modes make appearance. The growth of the shear modes can be attributed to the reduction in the frictional influence for the bilayers with thicker upper layer. Interestingly, when the upper is relatively thicker (dash dot line) we observe the appearance of a bimodal plot, in which the smaller wavenumber maximum corresponds to the i^L mode and the larger wavenumber maximum corresponding to the s^B mode. The curves corresponding to h_r = 1.3 and 1.5 together confirm that when the unstable wavenumbers for the i^L and s^B modes are very similar an interference of the unstable wavenumbers gives rise to the bimodality of the curves. The unevenly broken lines in the plot (f) shows that a more viscous upper layer not only destabilizes a free bilayer by fuelling up the i^U and s^B modes but also has a significant influence on the s^P mode even at a moderately high porosity. In such a situation, the additional inertial influence originating from the porous layer stabilizes the i^L mode. In contrast, when $\mu_r \leq 1$ the i^L mode appears and the s^P mode disappears. The observation here is again in commensuration to the base state plots in Figure 4.2(d), where we observed a higher (lower) slippage at the porous-liquid interface when the lower layer had smaller (higher) viscosity leading to a larger (smaller) inertial influence. Concisely, the

Figure 4.6 summarizes that presence of a porous layer underneath a free bilayer can have a lasting destabilizing influence, which can indeed have the potential to expedite the rate of momentum, heat and mass transfer in the microscale devices.

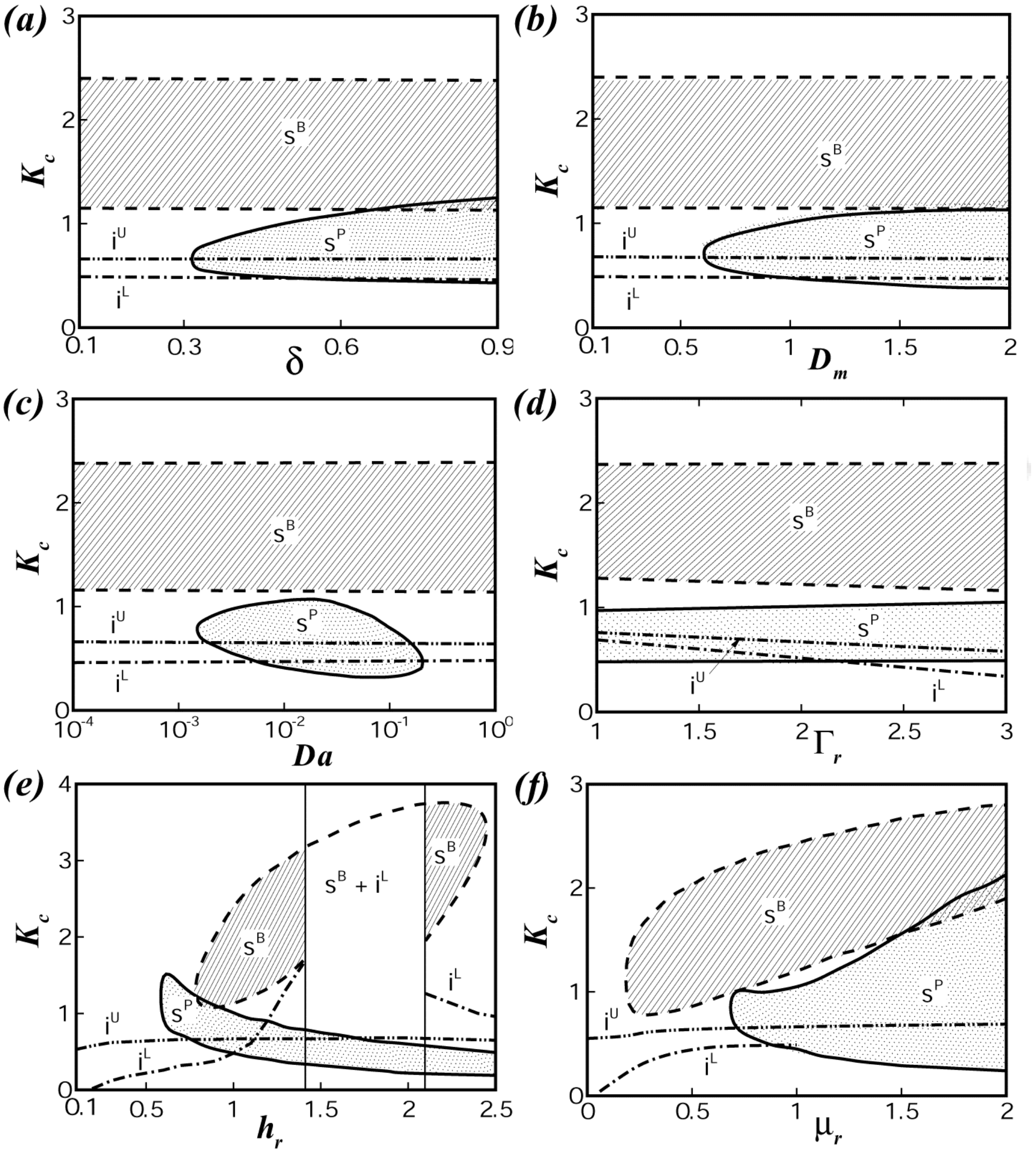

Figure 4.7: The plots (a) – (f) show the neutral stability diagrams, which are the variations of K_c with δ, D_m, Da, Γ_r, h_r and μ_r, respectively. For plot (d) $\Gamma_1 = 8 \times 10^3$ is fixed. The other parameters fixed for the plots are, $\delta = 0.5$, $D_m = 1$, $Da = 5 \times 10^{-3}$, $\rho_r = 1$, $\mu_r = 0.9$, $h_r = 1$, $\Gamma_1 = 8 \times 10^3$, $\Gamma_2 = 15 \times 10^3$ and $\alpha = 0.2$.

Plot (a) – (f) in the Figure 4.7 show the neutral stability plots with the variations in the δ, D_m, Da, Γ_r, h_r, and μ_r, respectively. The plots (a) – (c) show that the s^P mode appears only beyond a critical value of δ, D_m, and Da. Further, the span of unstable wavenumbers for the i^L, i^U and s^B modes remain undisturbed when δ, D_m, and Da are progressively increased. In comparison, the same for the s^P mode (i) always increase with the increase in δ, (ii) initially increase and then become constant with increase in the D_m, and (iii) initially increase to reach a maximum value and then reduce with the increase in Da.

The plots confirm that when the other parameters are fixed the porous media parameters can only influence the s^P mode. In comparison, the plots (d) – (f) show that the span of unstable wavenumbers for all the modes grows with the increase in the Γ_r, h_r, and μ_r, respectively. Plot (d) suggests that the span of unstable wavenumbers for the interfacial mode progressively reduce with increase in Γ_r. Interestingly, plot (e) shows the appearance of the i^L and s^B modes beyond a critical h_r (= 0.8), which progressively merges to a single mode at higher values of h_r (= 1.4), as denoted by the '$s^B + i^L$' zone in the area encompassed by the evenly broken line. It may be noted here that in this region only the bimodal growth coefficient versus wavenumber plots are observed. At higher values of h_r (= 2.1), as the shear mode progressively shifts more to the smaller wavelength regime due to the excess inertial influence, again the independent identities of the i^L and s^B modes are recovered. The plots also shows that the s^P mode makes appearance only beyond a critical h_r (= 0.6) as shown by the dotted region. With increase in the upper layer thickness the span of unstable wavenumbers for the s^P mode progressively shifts towards the longer wavelength regime. Plot (f) shows that a free bilayer with more viscous upper layer can destabilize a larger span of unstable wavenumbers for the s^P mode. The plot clearly shows the domain of presence of the i^L mode for a free bilayer flowing over a porous layer is essentially in the region where $\mu_r \le 1$.

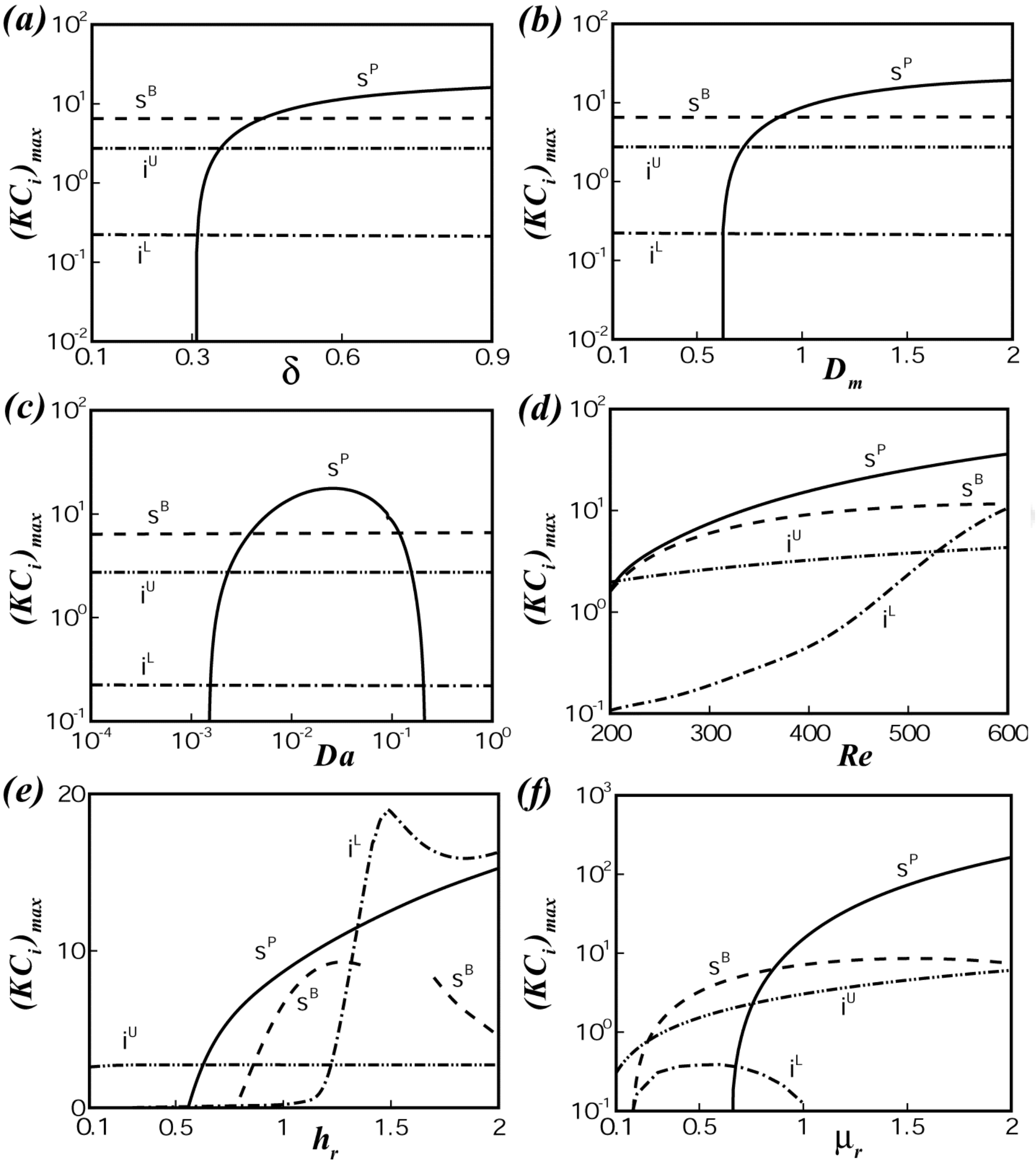

Figure 4.8: The plots (a) – (f) show the variation of $(KC_i)_{max}$ with δ, D_m, Da, Re, h_r and μ_r, respectively. The other parameters are fixed for the plots are, $\delta = 0.5$, $D_m = 1$, $Da = 5 \times 10^{-3}$, $\rho_r = 1$, $\mu_r = 0.9$, $h_r = 1$, $\Gamma_1 = 8 \times 10^3$, $\Gamma_2 = 15 \times 10^3$ and $\alpha = 0.2$.

In Figure 4.8 we find out that which of the instability modes dominate the instability of a free bilayer with the variations in δ, D_m, Da, Re, h_r, and μ_r. The curves in the plots (a) –

(c) show that at smaller values of δ, D_m, and Da the instability characteristics are similar to a free bilayer on an inclined impervious surface as the s^P mode is absent. The solid lines in the plots (a) – (c) also show that although the i^L, i^U and s^B modes remain undisturbed when δ, D_m, and Da are progressively increased, the s^P mode (i) progressively becomes the dominant mode with the increase in δ and D_m, and (ii) becomes the dominant mode only for a span of Da otherwise remains a sub-dominant mode.

The solid lines in the plots (d) – (f) also uncover that even when the porous layer is moderately porous and permeable the s^P mode can be the dominant mode of instability at a reasonably high values of Re, h_r, and μ_r, respectively. The plots also show that a thicker and more viscous upper layer helps in destabilizing the s^P mode to a larger extent and all the other modes are found to become the sub-dominant under such a situation. The discontinuity in the plot (e) for the i^L and s^B mode is associated with the bimodality of the growth coefficient versus wavenumber plots, as previously discussed. Again, plot (f) suggests that the i^L mode is present only when $\mu_r \leq 1$ for a free bilayer flowing on a porous layer. Concisely, the figure depicts that the addition of a porous layer underneath a free bilayer can develop an additional dominant mode of instability even at a reasonable porosity, thickness, and permeability of the porous layer. Figure 4.9 supports the travelling wave nature of all the instability modes for a free bilayer flowing on an inclined porous medium. Plot (a) – (c) suggest that phase speed (C_r) is not much sensitive to the porous media parameters except Da whereas plots (d) – (f) show that the same increases with increase in Re, h_r, and μ_r. Interestingly, the C_r for the s^P mode is always found to be smaller than the other modes, which can be explained from the location of the critical layers, as shown in the Figure 4.5(b).

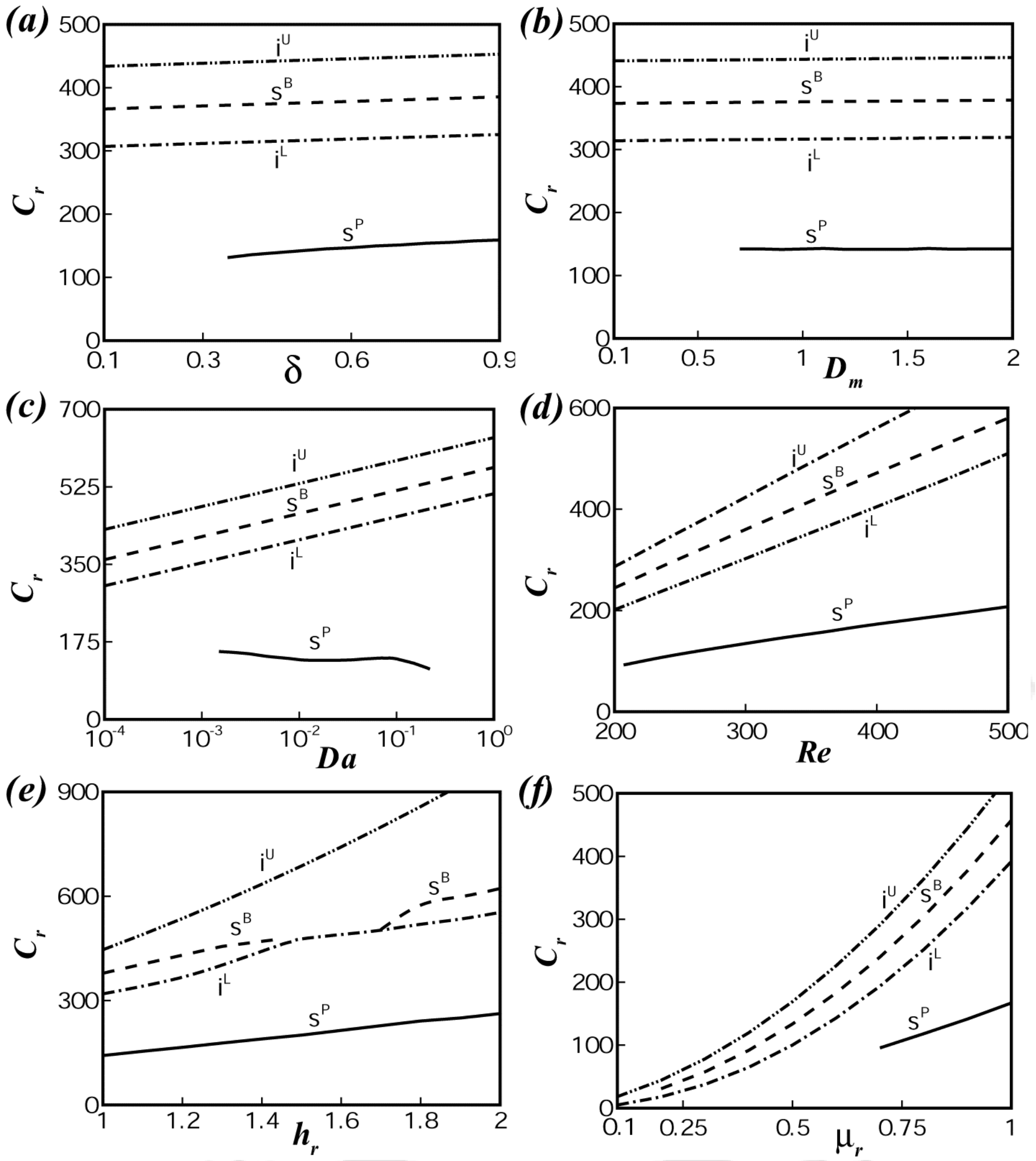

Figure 4.9: The plots (a) – (f) show the variation of C_r with δ, D_m, Da, Re, h_r and μ_r, respectively. The other parameters are fixed for the plots are, $\delta = 0.5$, $D_m = 1$, $Da = 5\times10^{-3}$, $\rho_r = 1$, $\mu_r = 0.9$, $h_r = 1$, $\Gamma_1 = 8 \times 10^3$, $\Gamma_2 = 15 \times 10^3$ and $\alpha = 0.2$.

Since the s^P mode has its origin at the lower layer near the porous-liquid interface it is under the maximum frictional influence as compared to the i^L mode at the liquid-liquid interface, i^U mode at the liquid-air interface, and s^B mode at the upper layer. Interestingly, the C_r for the instability modes ($i^U > s^B > i^L > s^P$) follow an order based on their location from the porous layer with the reduction in the frictional influence.

4.7 SUMMARY

The instabilities of an inclined free bilayer flowing over a Darcy-Brinkman porous layer have been explored. An O-S analysis of the governing equations and boundary conditions is performed to uncover the salient features of the instabilities. The major conclusions are,

(i) This configuration can be unstable by pair of long-wave interfacial modes at the free-surface and the interface together with a pair of finite wavenumbers shear modes originating from the inertial influences at the liquid layers. Like a free bilayer on an inclined impervious surface all the unstable modes are found to appear beyond a critical flow rate. All the modes are found to gain strength with increase in the flow rate, ratios of the upper to lower liquid film thickness and viscosities. The interfacial mode specific to the liquid-liquid interface (i^L mode) is found to be present only under the condition $\mu_r < 1$.

(ii) One of the shear modes (s^P mode) originates from the augmented inertial influence of the porous layer, which is found to be the dominant mode even at moderate porosity, permeability, and thickness of the porous layer. The strength of the s^P mode, (i) increases with increase in porosity, (ii) initially increases and then become constant with increase in porous layer thickness, and (iii) initially increases and then reduces with increase in the permeability of the porous layer. Interestingly, interfacial modes (i^L and i^U mode) and the conventional shear mode (s^B mode) specific to a bilayer on an impervious surface are found to be dormant to the change in the porous layer parameters.

(iii) Although the increase in the upper to lower ratios film thicknesses, viscosities, and the flow rate causes larger destabilization to all the modes, the s^P mode dominates when the porous medium is moderately porous, permeable, and thick.

(iv) Additional inertial influence originating from the flow inside porous media is the major reason behind the enhancement of the instability in a free bilayer flowing down an inclined plane

(v) An eigenfuction analysis shows the location of the s^B mode at the upper layer and the same for the s^P mode near the porous-liquid interface. Also, the phase speed analysis confirms the travelling nature of these instabilities and confirms a progressive increase in the phase speed as the modes are located away from the porous layer ($i^U > s^B > i^L > s^P$) and under the influence of lesser frictional force.

The results reported here of significance in improving the mixing, emulsification, and heat and mass transfer characteristics in the microscale devices.

Chapter 5

Dynamics of a liquid droplet on a granular bed of micro-structured particles

ABSTRACT

We explore the dynamics and morphologies of droplet permeation on loosely bound granular beds composed of micro-porous and micro-patterned particles. Naturally abundant particles such as *Cycas revoluta* (sago), *Papaver somniferum* (poppy), and *Sinapis alba* (mustard), have been employed to prepare the homogenous and heterogeneous porous-granular beds. The experiments uncovered that a highly porous bed of mustard particles could stabilize a static water lens by pinning the three-phase contact line of the droplet on the micro-patterns decorated on the particle surface. Interestingly, a water-lens could transform into a 'liquid marble' when the bed was composed of smaller poppy particles, which also possessed a micro-patterned hydrophobic surface. Simulations uncovered that an upward convective current originating from the deformation and recoil inside the droplet together with the vertical capillary force at the pinned three-phase contact line of the droplet enforced the poppy particles to climb up the surface of the water-lens and form the liquid marbles. A bed of micro-porous sago particles were also found to show a phenomenon similar to marble effect in which the particles remained partially or fully embedded inside the drop-surface rather than hanging from outside like the poppy particles. Simulations uncovered that an air current issuing out of the porous bed owing to the droplet permeation enforces the smaller micro-porous particles to dislodge from the bed and develop a marble effect type scenario. Heterogeneous porous-granular beds composed of poppy-crushed sago particles showed the two-different types of marble effects occurring simultaneously from different sides of the same droplet. The study on the kinetics of the drop permeation unfolded that the rate of permeation was much slower when the drop passed through the bed-air interface than when the droplet was already inside the bed. Addition of surfactant to the water droplet showed a faster

permeation rate, which also ensured a smaller life time for the lens and marble formation. In comparison, increase in viscosity increase the life of the lens and delayed the formation of the marble. Concisely, the study uncovers multitude of interesting dynamics of droplets over granular beds composed of particles with micro-porous and micro-patterned surface.

The manuscript on this chapter is currently under review.

5.1 INTRODUCTION

The hydrophobicity of a granular bed mainly depends on the surface energy of the materials. The studies regulate the hydrophobicity of the bed particles by choosing low surface energy bed particles such as talk, sand, and salinized glass beads. In contrast to this approach, natural surfaces inspire the use of periodic micro-structures on the surface of the bed particles to enhance the water repellence. Thus far, the behaviour of a water droplet on a bed of particles having micro-patterns or micro-pores is an entirely unexplored area of research.

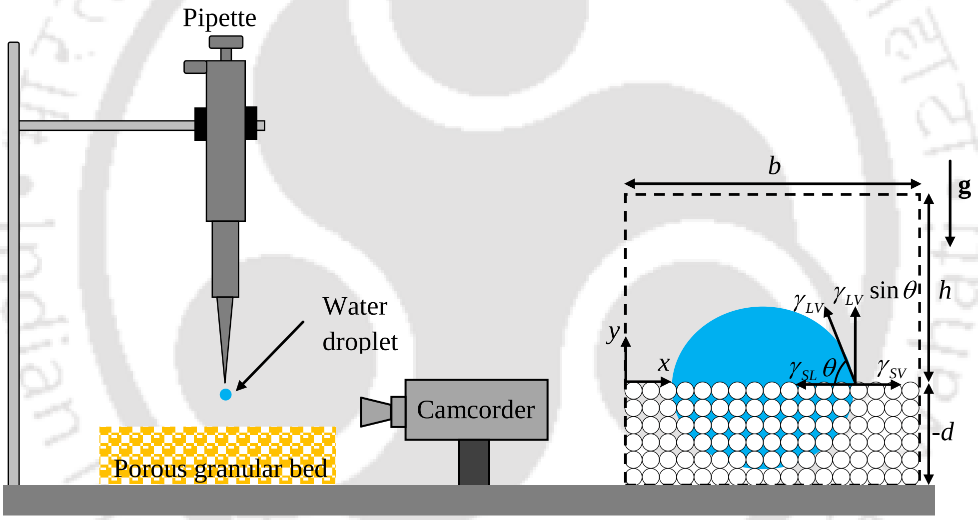

Figure 5.1: Schematic diagram of experimental setup of a droplet dispensed from a pipette nozzle on a porous-granular bed. The notations x and y denote the respective coordinates; the symbols γ_{LV}, γ_{SV}, and γ_{SL} denote interfacial tensions of the liquid-air, solid-air, and solid-liquid interfaces, θ is contact angle of droplet on the bed. In the computational study, the air domain was fixed to ($b \times h$), the porous-granular bed was in the ($d \times b$) domain, **g** shows the direction of the gravitational field.

In the present study, with the help of both computations and experiments, we unveil a number of exciting behaviors of a droplet on a bed of particles having either micro-patterned or micro-porous surface. Figure 5.1 schematically shows the experimental setup in which the porous-granular beds were prepared employing naturally abundant poppy (*Papaver somniferum*), mustard (*Sinapis alba*), sago (*Cycas revoluta*), and crushed-sago particles. The mustard and the poppy particles show excellent water repellency due to the presence of periodic microstructures decorated on the particle surface. The experiments revealed that a water droplet formed a lens on a highly porous mustard bed whereas the same experiment on a bed of smaller poppy particles showed a transition from a water lens to a liquid marble. The dynamics of drop permeation on a bed with micro-porous particles (sago and crushed-sago) was found to be completely different from the same on a bed of micro-patterned (mustard and poppy) particles. Further exciting behaviors were observed when the droplet was placed at the junction of a heterogeneous porous-granular bed composed of any two of the particles. The kinetics of the drop permeation on the uniform and heterogeneous porous-granular beds with the variations in the surface tension and the viscosity of the droplets have also been explored in detail. The mechanisms of the drop permeation on different types of beds were qualitatively analyzed through computational fluid dynamic (CFD) simulations, which uncovered different origins for the marble formation on beds with micro-patterned and micro-porous particles. Concisely, the study unveiled interesting transitions in the droplet and bed morphologies when high and low surface energy liquid droplets were dispensed on uniform and heterogeneous micro-porous or micro-patterned granular beds. The results reported could encourage future research related to the drop impact dynamics on porous and patterned granular beds.

5.2 EXPERIMENTAL PROCEDURE

Figure 5.1 shows the schematic diagram of the experiment setup. A rectangular trench with dimensions 22×17×5.5 mm (length × width × height) was prepared on a glass slide. Following this, *Cycas revoluta* (sago), *Papaver somniferum* (poppy), *Sinapis alba* (mustard), and crushed sago particles are employed to create the beds. The mustard and the poppy particles show excellent water repellency due to the presence of periodic polygonal cavities surrounded by ridges decorated on the particle surface, as shown in the SEM images (a) and (b) in Figure 5.2.

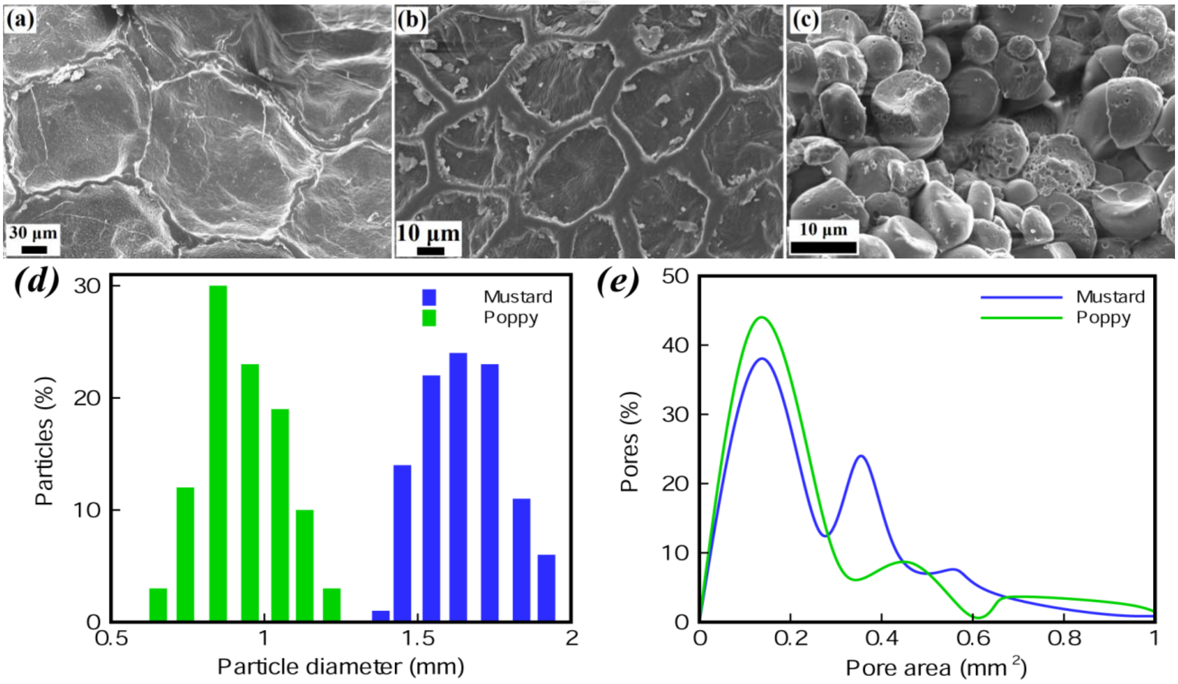

Figure 5.2: Scanning electron micrographs of the surfaces (a) *Papaver somniferum* (poppy), (b) *Sinapis alba* (mustard), and (c) *Cycas revoluta* (sago). Plot (d) shows the particle size distribution – particle diameter with percentage of the particles, for mustard and poppy particles, which is the. Plot (e) shows pore size distribution – pore area with percentage of pores, for mustard and poppy beds.

In comparison, the sago or the crushed-sago particles are rather hydrophilic owing to their micro-porous surface, as depicted in Figure 5.2(c). In the beginning of the experiments, the rectangular trenches were fully hand-filled with same type of granules to prepare beds with single type of particle. Heterogeneous beds were prepared using two types of granules in which each half of the trench was filled with one type of particles after making an interface between the two types of particles. An artificial barrier was placed in the middle of the trench before arranging the different types of particles on the sides. The barrier was then carefully removed after the bed was ready.

Table 5.1: Particle details

Particle	Shape	Mean size (mm)	Density[37] (kg/m^3)	Void fraction (ϕ)
Mustard	Circular	1.68	541	0.39
Poppy	Been shaped	0.94	596	0.43

Table 5.2: Surface tension and viscosities with the change in SDS and glycerol concentration

SDS in water (% w/v)	Surface Tension mN/m	Glycerol in water (% v/v)	Viscosity Pa s
0.1	37.1	100	1.069
0.5	36	75	0.0302
1	36.2	50	0.005
5	35.5	25	0.0031
10	34.6	0	0.001

The drop-impact experiments on these beds were performed after no further processing like vibration or shaking. The typical particle and pore size distributions are depicted in the Figures 5.2(d) and 5.2(e). The mean size, shape, and density of the particles are provided in the Table 5.1. The beds were placed on a stage and a micropipette attached to burette stand was employed to gently dispense the droplet on the bed. The distance between micropipette tip and bed surface was kept very small and constant for all the experiments and the mean size of the droplet is 4.74 mm. In the beginning of the experiments composed of Millipore water (resistivity of 18.2 MΩ cm) was gently dispensed at the center of the beds from the micropipette. The permeation of the water droplet through the porous-granular bed was recorded employing a camcorder (Sony HRD). The surface tensions of the samples were measured by a digital tensiometer [Krüss

(Germany)] employing a standard du Noüy ring (Pt/Ir) method following the procedure ASTM Standard D1331-11 (2001). In all the experiments 100 μl of blue dye was added to color the 100 ml of water for image analysis. The change in surface tension due to the dye addition was measured to be marginal – from 0.072 N/m to 0.068 N/m. To study the effect of surfactant, 0.1% to 10 % (w/v) of sodium dodecyl sulphate (SDS) was added in 100 ml water, as shown in the Table 5.2. Further, to study the effect of viscosity glycerol was mixed with water on v/v basis, as shown in the Table 5.2. The time dynamics of the droplets were studied by separating the frames from the video and then evaluating the area of the droplet from the open source image processing ImageJ software. The dyed blue area specific to the water droplet on the granular bed was isolated through the image analysis before calculating the area through the software. In order to find out the void-fraction (ϕ), initially the pore volume was determined by fully immersing the porous-granular beds with hexane and then evaluating the ratio of the pore to trench volume.

5.3 COMPUTATIONAL SECTION

Figure 5.1 schematically shows the two-dimensional (2-D) computational domain employed for this study. The fluid was assumed to be Newtonian, the flow was considered to be incompressible, and the gravitational field was assumed to be in the negative *y*-direction. The following continuity and equations of motion were employed to describe the motion of a droplet though a porous-granular bed:

$$\nabla \cdot \mathbf{v} = 0 , \tag{5.1}$$

$$\frac{\partial \mathbf{v}}{\partial t} + \mathbf{v} \cdot \nabla \mathbf{v} = -\frac{1}{\rho} \nabla p + \nu \nabla^2 \mathbf{v} . \tag{5.2}$$

Where the notations $\mathbf{v}$, p, μ , ρ and $\nu\left(=\mu / \rho\right)$ denote the velocity vector, pressure, viscosity, density and kinematic viscosity, respectively.

Table 5.3: Parameter for simulations

Particle Dimension (mm)			Computational Domain (mm × mm)	Droplet Properties	Air Properties
 **Porous**	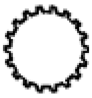 **Patterned**	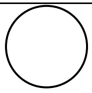 **Smooth**	Bed: 12×4.125	γ: 0.0728 N/m	-
			Air: 12×7.875	μ_2: 0.001 Pa s	μ_1: 1.78×10^{-5} Pa s
Dia.: 0.75 Pore width: 0.125	Dia.: 0.75 Ridge-width-0.05	Dia.: 0.75	Total: 12×12	ρ_2: 998.2 kg/m^3	ρ_1: 1.225 kg/m^3

Table 5.3 shows the typical values employed in the simulations and the structures employed for the granules to qualitatively model the experimental porous beds with micro-porous and micro-patterned particles. The air-water two-phase flow was modelled employing the volume of fluid method (VOF) from the commercial software ANSYS FLUENT^{TM}.

The method initially solved a single set of momentum equations and then tracked the interface by solving the continuity equation (Eq. 5.1) with the restriction, $\sum_{i=1}^{n} \alpha_i = 1$:

$$\frac{1}{\rho_i}\left[\frac{\partial}{\partial t}\left(\alpha_i \rho_i\right)+\nabla.\left(\alpha_i \rho_i \mathbf{v}_i\right)\right]=\sum_{j=1}^{n}\left(\dot{m}_{ij}-\dot{m}_{ji}\right). \qquad (5.3)$$

Here α_i and ρ_i denote the volume fraction and density of the i^{th} fluid. The notation $\dot{m}_{ij}$ ($\dot{m}_{ji}$) denotes the rate of mass transfer from phase *i* (*j*) to phase *j* (*i*). The geometries and the grids were prepared using the commercial software GAMBIT from ANSYS FLUENT^{TM}. The typical grid size was around 0.025 mm (~5×10^5 cells in a 12 mm ×12 mm domain). The side faces of the geometries were modelled with symmetry boundary condition. The top face of the geometry was modelled as velocity inlet with stationary fluid. The walls (granular bed surfaces) in the geometries were assumed to be no-slip and impermeable ($v_x = v_z = 0$).

The governing equations together with the boundary conditions were solved using ANSYS FLUENT^{TM}, which uses finite volume method to convert the governing equations to algebraic form. In this study, we employ PRESTO scheme for pressure interpolation scheme, SIMPLE scheme for the pressure–velocity coupling, and QUICK scheme for the upwinding of the convective terms of the momentum equation. The liquid-air interface module in ANSYS FLUENT follows the continuum surface force (CSF) model.[133] The most accurate geometric reconstruction model was employed to reconstruct the interface in each time step. The mixing law $\rho = \alpha_2 \rho_2 + (1-\alpha_1)\rho_1$ was used to calculate μ and ρ of the mixture. The simulations were conducted with typical time steps of around 10^{-5} to 10^{-6} sec and the grid independence of the solutions were ensured.

5.4 RESULTS AND DISCUSSION

Figure 5.1 schematically shows the various pathways of drop permeation after a droplet is gently dispensed on the surface of a loosely bound porous-granular bed. In this situation, it can easily be envisaged that the droplet can either immediately permeate through the bed or form a permanent lens by pinning the contact line on the bed particles or initially form a lens and later permeate through the bed. A water droplet is expected to permeate quickly through a hydrophilic granular bed with high porosity whereas a hydrophobic bed with lower porosity can promote the lens formation. In the latter case, while the water droplet forms a lens on the bed, it can undergo a periodic deformation and recoil to produce convection currents within the bulk of the droplet when it tries to achieve equilibrium contact angle. In parallel, the three-phase contact line of the droplet can also be under the exposure of the lateral and vertical components of the surface tension force, as depicted by the arrowheads in the Figure 5. 1.

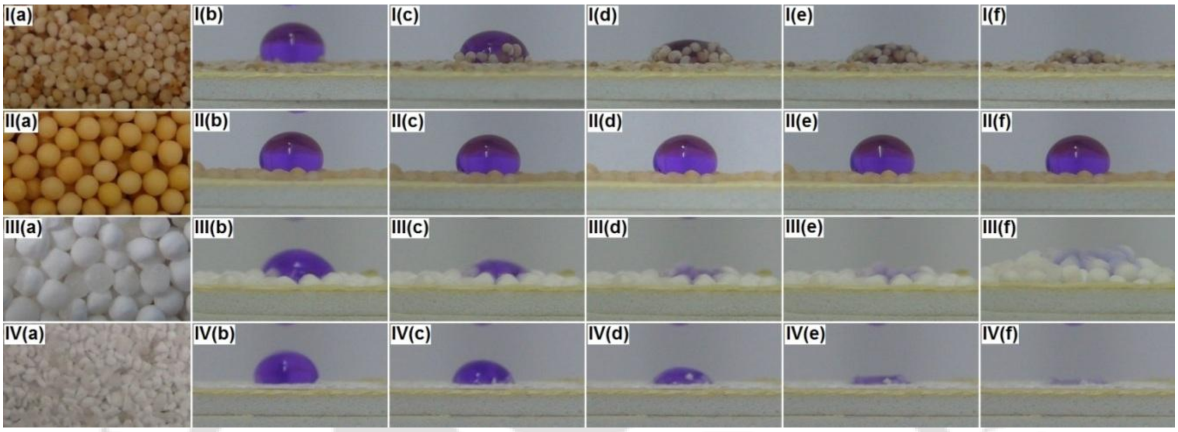

Figure 5.3: Dynamics of water droplet on porous-granular beds composed of poppy particles (ϕ = 0.39) in the I row, mustard particles (ϕ = 0.43) in the II row, sago particles (ϕ = 0.47) in the III row, and crushed sago particles (ϕ = 0.57) in the IV row. Image (a) in each row shows the bed morphology before the droplet was dispensed. Images (b) – (f) show the permeation of the droplet with time (t). I(b) – I(f) corresponds to t = 0, 20, 40, 60, and 80 s; II(b) - II(f) corresponds to t = 0, 10, 20, 30, and 100 s; III(b) - III(f) corresponds to t = 0, 0.04, 0.08, 0.12, and 1.6 s; IV(b) - IV(f) corresponds to t = 0, 0.08, 0.12, 0.16, and 0.24 s.

The cumulative influence of the vertical surface tension force and the convection current due to drop deformation and recoil can move or dislodge the loosely bound bed particles from the highly shearing base to the freely shearing roof of the droplet when the net vertical pull overcomes the weight of the bed particles. The following experiments and simulations uncover that the presence of micro-pores or micro-patterns on the surface of the bed particles can indeed play a decisive role in the movement of the bed particles and subsequent bed morphologies.

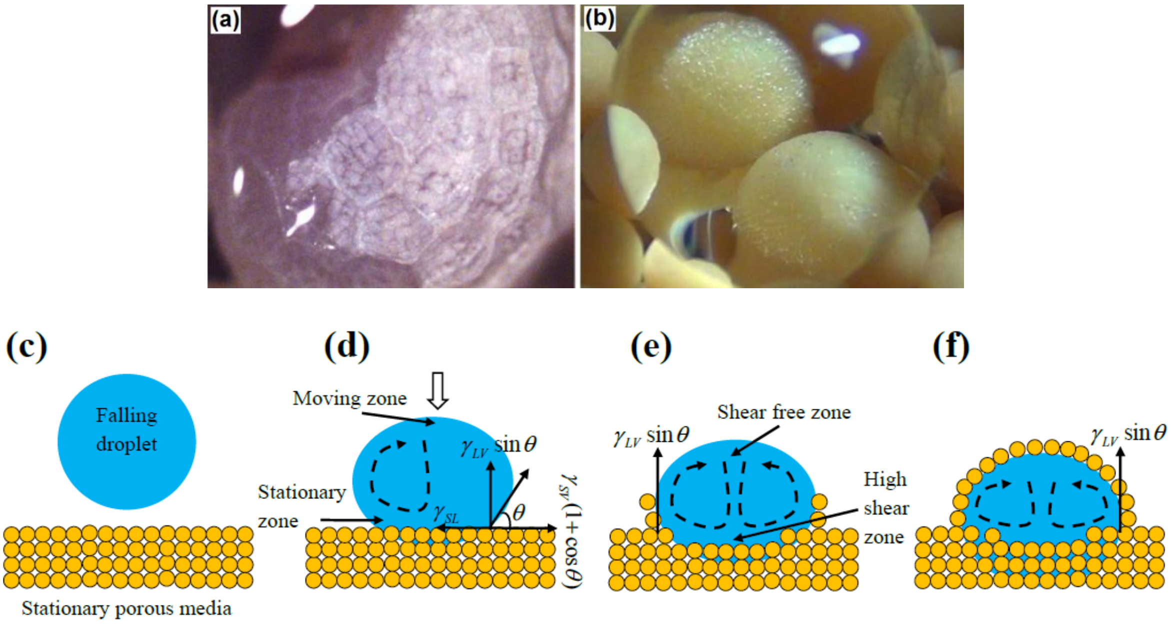

Figure 5.4: (a) Image of a water droplet (left part) pinned on the ridges of the patterns on the poppy surface forming a Wenzel state. (b) Droplet sits on the surface of mustard particle to form Wenzel type water lens. Images (c) – (f) illustrate the different stages of water droplet permeation through the porous granular bed. The symbol θ is contact angle and the symbols γ_{LV}, γ_{SV}, and γ_{SL} denote interfacial tensions of the liquid-air, solid-air, and solid-liquid interfaces respectively.

Rows I – IV in Figure 5.3 show spatiotemporal images of the permeation of a water droplet through the porous-granular beds composed of poppy, mustard, sago, and crushed sago particles, respectively. The image (a) in each row shows the top view of the bed before the droplet was dispensed. The row I of Figure 5.3 shows that in short time [image (b)] a water lens was formed after the droplet was dispensed on a poppy bed (void fraction, ϕ = 0.39). The SEM image in Figure 5.2(a) depicts the surface of a poppy particle having periodic polygonal cavities surrounded by elevated boundaries of average width ~10 μm. Thus, the base of the water lens was in contact with the periodic ridges of the micro-patterns decorated on the bed particles. Figure 5.4(a) confirms that the droplet was in Wenzel state in which the cavities were filled with the water while the contact line was pinned on the micro-structures. The pinning of the three-phase contact line of the water droplet on the micro-patterns prevented the permeation of the droplet at the initial stages. Images (c) – (f) in Figure 5.3 show that with progress in time the loosely bound poppy particles near the three-phase contact line were found to climb one after the other to the free-surface of the droplet. The micro-ridges decorated on the poppy particles pinned them to the free-surface of the droplet and the ‘clip-drop’ climbing of the particles led to a marble effect – as a collection of the poppy particles covered the droplet free-surface. Following this, the poppy particles covering the water droplet helped the drop to permeate through the bed as the total weight of the particle loaded on the droplet increased and a void inside the bed was created because of the movement of the bed particles to the droplet surface. Intuitively one can easily infer from this experiment that a bed with similar but smaller particles could lead to a temporally stable marble by delaying the drop permeation through the bed. With progress in time, as the drop permeated inside the bed [image (f)], a crater shaped morphology was observed on the bed surface. The mechanism of the droplet permeation is schematically illustrated in Figure 5.4 and later explained with CFD simulation in the Figures 5.6 and 5.7. The images (c) – (f) in Figure 5.4 show that the when the droplet came in contact with the granular bed composed of micro-patterned particles, it had undergone a deformation and recoil owing to the presence of a moving free surface and a stationary base of the droplet. The broken lines schematically show the typical convection current could set in owing to this reason. Further, at the pinned contact line the surface tension forces were also active to ensure an equilibrium contact angle. In consequence, the vertical component of the surface tension force together with the current due to the deformation and recoil of the droplet generated a motion from the highly shearing base to the freely shearing surface of the droplet, which eventually dislodged the particles to form the marble. Importantly, when the same experiment was performed with increasing surfactant concentration in the water droplet, the drop permeated through the bed at a faster rate reducing the time and scope for the marble formation. Further, a hexane droplet immediately permeated through the same bed without forming the marble. The control experiments confirmed that indeed the initial lens formation and the subsequent marble effect took place because of the pinning of the three-phase contact line of the high surface energy water droplet on the micro-ridges decorated on the poppy surface. The row II of Figure 5.3 shows the droplet formed a permanent Wenzel lens when the bed was composed of relatively bigger mustard particles with micro-patterned surface. Importantly, in this situation the weight of the bed particles was large enough to restrict the marble formation. The Wenzel state of the lens on the mustard bed is evident in the optical image in Figure 5.4(b), which also shows that the three-phase contact line pinned on the micro-ridges on the mustard particles. It may be noted here that even though the void fraction was larger for the mustard bed (ϕ = 0.43) as compared to the poppy bed (ϕ = 0.39), the micro-structures on the mustard surface were able to stabilize the lens. Importantly, a low surface energy water droplet with surfactant or a hexane droplet permeated instantaneously through the same mustard bed, which confirmed that the lens formation was only because of the pinning of the three-phase contact line on the micro-patterns. The two experiments reported above unveiled the interesting situations where a droplet on a micro-patterned porous-granular bed could either form a stable lens or transform a water lens to a liquid marble.

Apart from the micro-structures, the micro-pores on the surface of the bed particles could also show interesting features, as shown in the rows III and IV of the Figure 5.3. In these experiments we employed sago and crushed sago particles, which had size similar to the mustard and poppy particles, respectively. Images in row III of Figure 5.3 established that a water droplet permeated instantaneously through a bed of sago particles. The bed swelled with time as the sago particles soaked water from the droplet through the micro-porous surface.

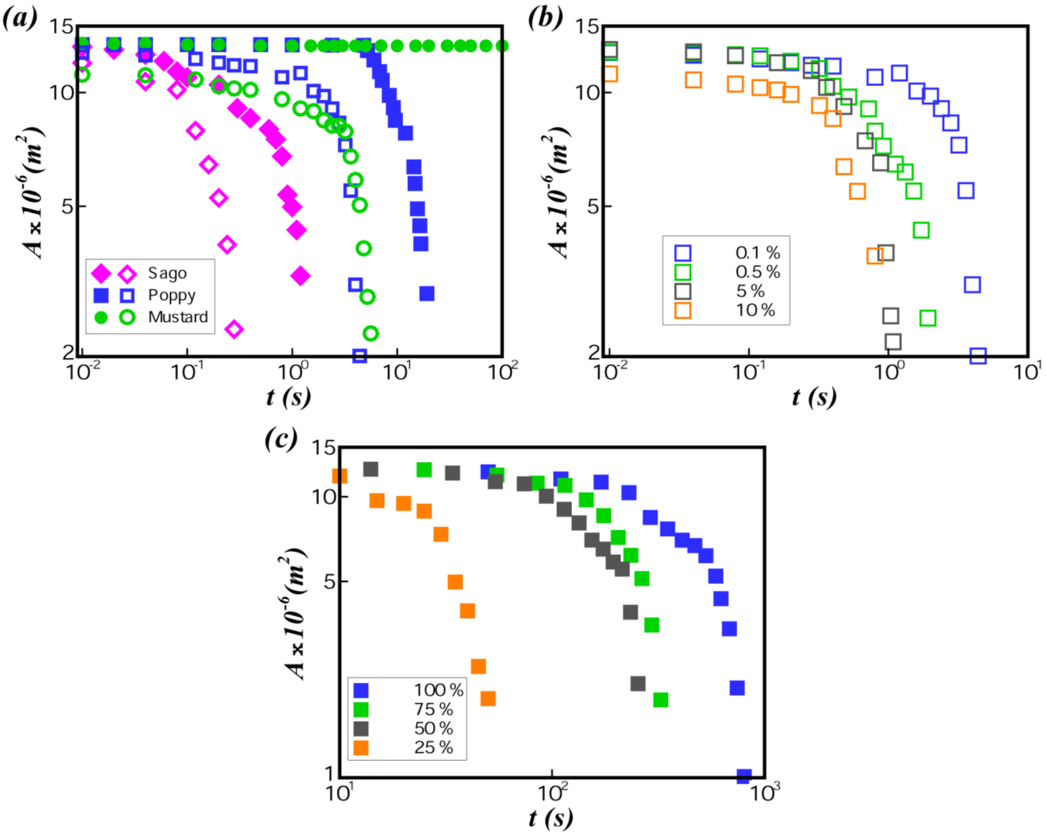

Figure 5.5: Plot (a) – (c) shows the variations in the area (*A*) of the droplet with time (*t*) on different types of porous beds. In the plot (a), filled symbols represent pure water and hollow symbols represent the droplets loaded with 0.1% of surfactant solution. Plot (b) shows the kinetics of the droplet on the poppy bed at different surfactant concentrations. Plot (c) shows kinetics of the droplet on the poppy bed at different viscosities of the droplet. The variations in the surface tension and the viscosities are provided on Table 5.2.

The experiment showed that the presence of micro-pores on the surface of the bed particles can impose a hydrophilic behavior to the bed particles and expedite the rate of permeation. The images in the row IV in Figure 5.3 suggest that when the sago particles were crushed down to the size of poppy particles, the time for droplet permeation remained similar as it was found for the regular sago particles. Interestingly, the images (b) – (c) in the row IV shows that the micro-porous crushed sago particles could also climb up on the drop surface, as it was observed previously for the poppy particles. A very close look on the drop surface ensured that unlike the poppy particles, which hanged to the outer periphery of the droplet, the crushed-sago particles moved upwards after remaining fully or partially embedded inside the droplet. The micro-capillaries present on the surface of the crushed sago particles not only soaked water from the droplet but also acted as a connector between the droplet and the sago particles, which helped them moving upward as the droplet moved within the bed. The phenomenon appeared similar to marble effect with the difference that the micro-porous bed particles remained connected from the inner water side of the droplet surface rather than hanging from the outer air side.

Figure 5.5 shows that kinetics of drop permeation through the beds of poppy, mustard, and sago particles in which the hollow (filled) symbols represent the water droplet with (without) surfactant. The variations in the area of the droplet above the bed (A) with time (t) were calculated through image analysis, as described in the experimental section. Three major observations from these plots are: (i) the drop permeation rate was much slower at the initial stage when the drop penetrated through the bed surface whereas at the later stage the droplet permeated at a faster rate; (ii) addition of surfactant led to faster permeation of the water droplet through the porous-granular bed; (iii) increase in viscosity of the droplet only led to a slower kinetics of penetration. The filled circular symbols in the plot (a) indicate that a pure water droplet formed a permanent lens on a mustard bed whereas addition of surfactant led to a quick permeation of the droplet through the bed, as shown by the hollow circles.

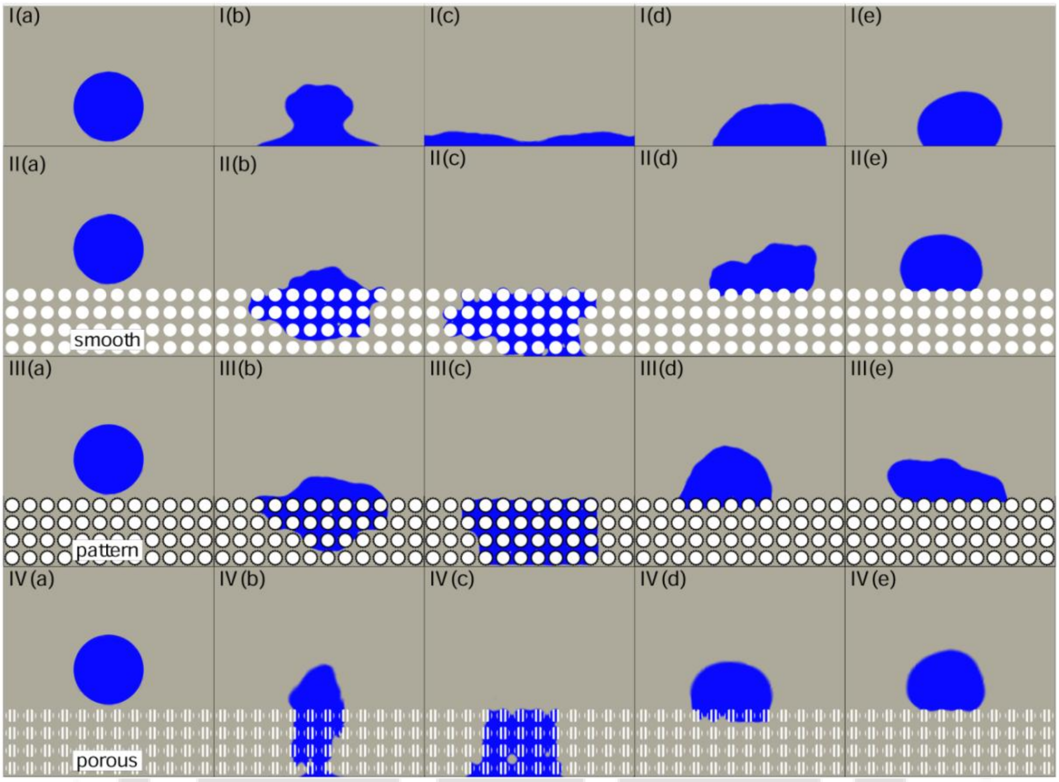

Figure 5.6: Numerical simulations of droplet permeation on different type of porous-granular beds. In row (I) the surface is flat and impermeable; in the row (II) the bed is composed of circular particles having smooth surface ($\phi = 0.55$); in the row (III) the circular bed particles posses micro-patterns on the surface ($\phi = 0.51$); in the row (IV) the bed is composed of micro-porous particles ($\phi = 0.78$). For the images (a) – (c) the equilibrium contact angle between the liquid and the solid surface is set to 20^o whereas for the images (d) and (e) the same is 90^o and 135^o, respectively. In row III the images (d) and (e) correspond to the contact angles 60^o and 90^o, respectively.

Addition of surfactant reduced the surface energy of the water droplet considerably, which relaxed the pinning of the three-phase contact line on the micro-ridges and allowed the water droplet to permeate easily through the bed. The filled square symbols in the plot (a) indicate a lens formation in short time on a bed of poppy particles. At the intermediate stage, formation of marbles slowly allowed the drop to permeate through the bed whereas in the later stages the poppy particles on the surface of the droplet quickly pushed the droplet into the bed. The hollow square symbols in the plot (a) show that the drop permeation was rather faster when surfactant was added to the water droplet. Even, the droplet with surfactant showed a faster permeation through the bed composed of sago particles as indicated by the diamond symbols. Plot (b) shows that with the increase in the surfactant concentration the time for lens and marble formation were reduced as the droplet permeated rather quickly through the bed. Plot (c) suggests that increase in the viscosity of the droplet could kinetically stabilize the lens formation and slow down the process of marble formation. Concisely, the plots summarize interesting kinetic behavior of the lens formation, transition from lens to marble, and the rate drop permeation on various porous-granular beds.

The simulation images in Figure 5.6 show the changes in the drop permeation process with the variation in the bed porosity, surface energy of bed particles, and the surface morphology of the bed particles. It may be noted here that for the simulations the bed particles were kept stationary. The images (a) – (c) in the row I show that spreading of a droplet on a smooth, non-slipping, and impermeable hydrophilic surface whereas images (d) and (e) show the lens formation on the surfaces with increasing hydrophobicity. In the simulations the hydrophobicity of the surface was increased by increasing the equilibrium contact angle between the liquid and the substrate, as reported in the figure captions. The images (a) – (c) in the row II show that when the flat surface was replaced by circular shaped smooth and hydrophilic particles, the drop quickly permeated through the porous bed (ϕ = 0.55). Image (c) clearly shows that the water droplet completely wetted the bed particles while permeating through the bed. Increasing the hydrophobicity of the same bed showed lens formation in the images (d) and (e) even when the bed porosity was maintained at ϕ = 0.55. A comparison between the shapes of the three-phase contact line of the droplets near the surface of the images (d) and (e) in the rows I and II uncover that the periodic roughness on the bed of circular particles increased the local equilibrium contact angle hence the hydrophobicity of the rough surface as compared to the flat surface. The images in the row III shows the drop permeation on a porous-granular bed (ϕ = 0.51) composed of circular particles having periodic micro-ridges on the surface, as shown in the Table 5.3. The micro-patterned particles in the simulations closely mimicked the cross-sectional geometry of the mustard particles. Images (a) – (c) in the row III show that the droplet easily permeated through a hydrophilic bed, which is well in agreement with the experiments where a water droplet with surfactant or a hexane droplet could easily permeated through the mustard bed. The images (d) and (e) reveal that as the hydrophobicity of the bed particles were enhanced by increasing the equilibrium contact angle between the droplet and the particles, the lens formation was encouraged. Importantly, we observe a transition from Wenzel to Cassie–Baxter state of lens formation with increase in the hydrophobicity of the patterned surface. The simulations uncovered that when the surface is partially wetting (θ = 60°) the Wenzel state was preferred whereas beds with particles having higher hydrophobicity (θ = 90° and 135°) showed a Cassie-Baxter state of lens formation. Again the computations corroborated that the partially-wetting and micro-patterned surface of the poppy and the mustard particles promoted a Wenzel state of lens formation with contact line pinning on the micro-structures. In addition, the simulations reveal that the particles with larger hydrophobicity can even form Cassie-Baxter lens when aided by the micro-structures on the surface. The row IV in the Figure 5.6 shows the permeation of the droplet through a porous-granular bed composed of particles having micro-capillaries or micro-pores, as shown in the Table 5.3. Images (a) – (c) show that presence of the micro-pores on the porous particles ensured a faster localized permeation of the droplet than spreading on a hydrophilic bed (ϕ = 0.78).

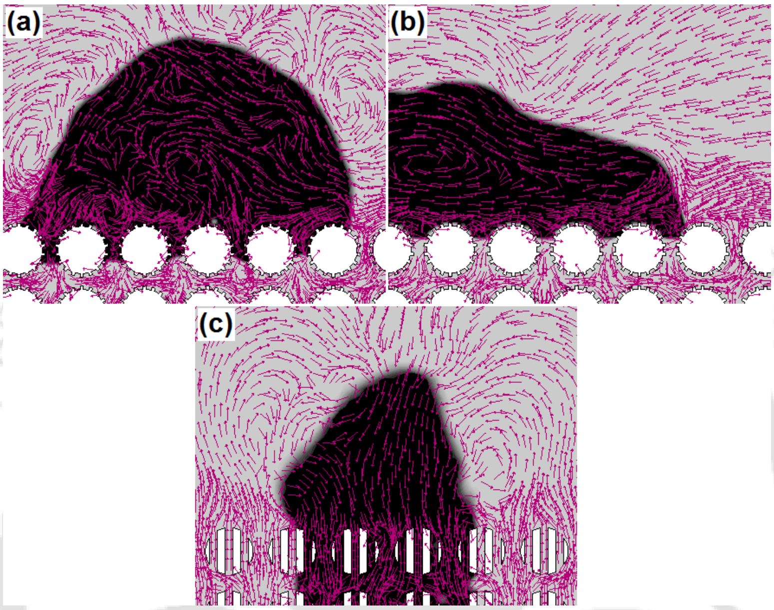

Figure 5.7: Velocity vector plots of droplet on porous beds, (a) granular bed with contact angle 60° [Figure 5.6 row III, image (d)], (b) granular bed with contact angle 90° [Figure 5.6 row III, image (e)] and (c) hydrophilic granular bed [Figure 5.6 row IV, image (b)].

The observations in the simulation qualitatively resembled the experiments as the droplet underwent a fast localized permeation through sago or crushed sago beds. Further, the images (d) and (e) show that the water droplet could form lens even on the porous bed when it is composed of hydrophobic or superhydrophobic micro-porous particles.

A magnified view with velocity vectors of the images III(d), III(e), and IV(b) of Figure 5.6 are shown in the images (a), (b), and (c) of Figure 5.7, respectively. These images provide important information on the drop dynamics through a porous bed composed of micro-patterned and micro-porous particles. Image (a) shows that, (i) the droplet formed a Wenzel lens when the bed was partially wetted by the liquid (θ = 60°); (ii) the three-phase contact line was always pinned to the micro-structures on the particle surface; (iii) the vectors indicate that there was a strong current starting from the basement of the droplet to the free-surface. The simulation qualitatively confirmed that the light-weight and loosely bound bed particles having micro-structures could move towards the droplet free-surface under the influence of this convection current, as observed for the poppy particles in the Figure 5.3. In such a situation, the particles would be connected to the droplet surface from the air-side through the three-phase contact line. The image (b) shows that increase in hydrophobicity (θ = 90°) of the particle surface led to a transition from Wenzel to Cassie-Baxter state. In such a situation, the contact line of the droplet was not only pinned on the micro-structures but also there were cushions of air pockets under the droplet in between the micro-patterns. The image (c) shows that, (i) when the bed was composed of micro-porous hydrophilic particles, the droplet permeation created a downward water current inside the droplet towards the bed; (ii) as the water flowed into the bed, the displaced air came out from the sides of the droplet through the open pores, which created an upward current towards the free-surface of the droplet; (iii) lighter and loosely bound particles could dislodge from the bed surface under this current, as found in the case of the crushed sago particles. The simulation also showed that the particles near the contact line were partially submerged, as observed in the experiments while the crushed sago particles showed a marble effect type scenario. Concisely, the motions inside and outside the droplet on a micro-patterned and micro-porous bed in Figure 5.7 qualitatively corroborate the propositions employed to describe the experimental results.

Rows I – III in Figure 5.8 show a collection of experimental images in which the permeation of a water droplet was studied on heterogeneous porous-granular beds such as mustard-poppy [image (a) in row I], poppy-crushed sago [image (a) in row II], mustard-crushed [image (a) in row III], and sago-crushed sago [image (a) in row IV]. In each case the drop was dispensed exactly at junction of the two different types of bed particles. The images (b) – (f) in the row I shows that the dispensed drop formed a lens on a mustard-poppy bed in short time.

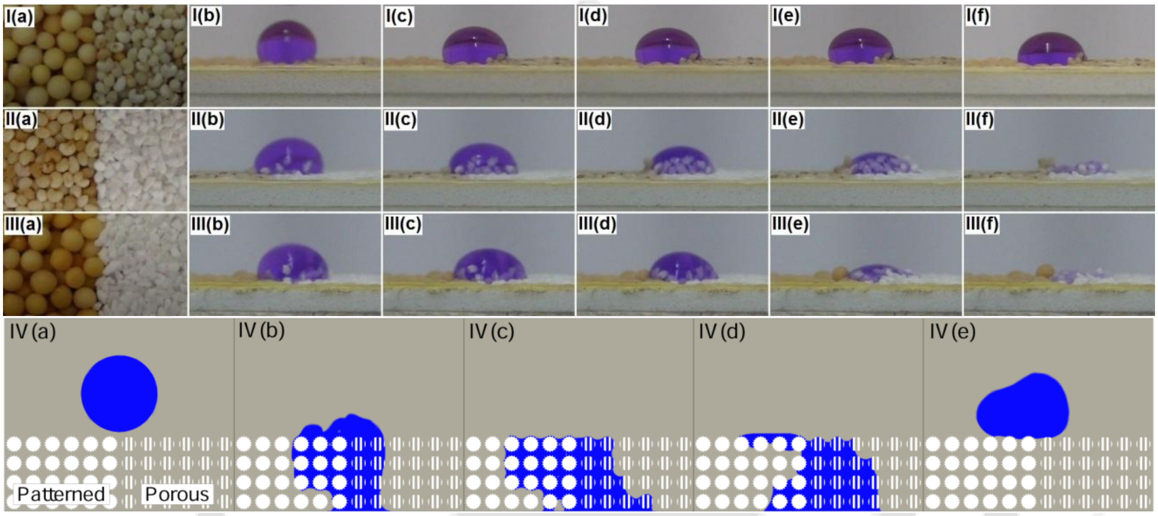

Figure 5.8: Dynamics of water droplet on heterogeneous porous beds composed of, mustard – poppy in the I row, poppy – crushed sago in the II row, and mustard – crushed sago in the III row. Image (a) show the bed before the experiment and the images (b) - (e) show the permeation of the droplet with time (*t*). Images I(b) – I(e) corresponds to t = 0, 2.8, 10, 22, and 48 s; 2(b) - 2(e) corresponds to t = 0, 0.04, 0.08, 0.12, and 0.2 s; and III(b) - III(e) corresponds to t = 0, 0.04, 0.08, 0.16, and 0.28 s. The images in the IV row show numerical simulations of droplet permeation on a heterogeneous porous bed – having one half micro-patterned particles and the other half with micro-porous particles. For the images (a) – (c) the equilibrium contact angle between the liquid and the solid surface is set to 20^{o} whereas for the images (d) and (e) the same is 90^{o} and 135^{o}, respectively.

With progress in time some of the poppy particles climbed on the drop surface leading to a partial permeation of the droplet in the side of the bed where the poppy particles were present. In this case a competition between the lens and marble formation was observed in which the lens formation prevailed largely with a partial marble effect in the poppy side. Images in the row II shows that in comparison to mustard-poppy bed, a crushed sago-poppy bed shows the marble effect when the drop was dispensed. The images (b) – (f) shows that in short time the droplet shifted towards the side where the sago particles were present. Following this, the poppy particles climbed on the drop free-surface from one side whereas the crushed sago particles from the other side led to a liquid marble comprising of both crushed sago and poppy particles before permeating through the bed. Again, the poppy particles were hanging outside whereas the crushed sago particles were partially or fully immersed inside the droplet. As compared to the experiment in row II, if the poppy particles were replaced with mustard particles (row III) the initial movement of the droplet towards the crushed sago side was found to dislodge some loosely bound mustard particle. However, in this situation, largely the crushed sago particles climbed up the droplet free-surface owing to its lesser weight as compared to the mustard particles.

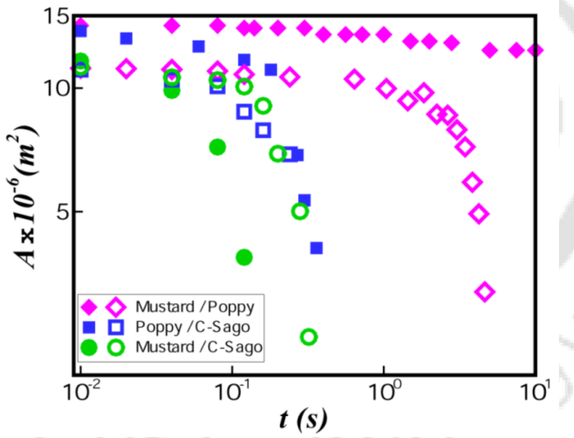

Figure 5.9: The plot shows the variation in the area (A) of the droplet with time (t) on different types of heterogeneous porous-granular beds. In the plot, filled symbols represent pure water droplet and hollow symbols represent the droplets loaded with 0.1% of surfactant solution. The notation ‘C-Sago’ corresponds to the crushed sago particles.

The simulation images (a) – (c) in the row IV rightly captured the movement of the droplet from the mustard to the sago side while showing a preferential permeation of the droplet through the sago part. The images (d) and (e) show that with increase in the equilibrium contact angle between the droplet and the micro-porous bed particles lens formation could also be a possibility for such types of porous-granular beds.

Figure 5.9 shows that kinetics of drop permeation through the porous-granular beds composed of heterogeneous particles as shown in Figure 5.8. The filled circular symbols depict the kinetics for the pure water droplet whereas the hollow symbols represent the droplets loaded with surfactant. As we observed for the beds with single particles, the drop permeation rate on the heterogeneous beds was also found to be much slower at the initial stages as compared to the later stages. Further, we also observed that addition of surfactant led to faster permeation of the water droplet through the beds. The filled diamond symbols indicate that a pure water droplet permeated partially on a bed composed of mustard-poppy particles and then formed a stable water lens on the bed. The hollow diamond symbols indicate that when such a droplet is loaded with surfactant, it could form lens only for short time before permeating through the bed. With increase in the surfactant concentration the time for lens formation and permeation was found to be smaller. The hollow and filled square (circular) symbols denote a pure water droplet on a bed of poppy-crushed sago (mustard-crushed sago) particle could permeate much slower as compared to the process when water droplet is loaded with surfactant.

5.5 SUMMARY

We explore the permeation of high surface energy water droplets through a bed of granular particles having micro-structured and micro-porous surfaces. Naturally abundant hydrophobic and hydrophilic particles were incorporated to prepare the uniform and heterogeneous granular beds. The major conclusions are,

(i) A high surface energy droplet on a bed of particles with micro-structured surface could form lens even on a highly porous bed. The three-phase contact line of the droplet was found to pin on the micro-structures present on the bed particles to stabilize a Wenzel type water lens. With increase in hydrophobicity of the particles a Cassie-Baxter type lens is predicted. The water lens was dynamically transformed into a liquid marble – with a water core encapsulated by micro-patterned particles, when smaller poppy particles with micro-patterned surface formed the granular bed. The duration of the lens and marble formation was found to reduce as the surface energy was reduced by adding surfactant into the water droplet. A stable lens and a delayed marble formation were observed with increase in the viscosity of the droplet. Computational studies uncovered that the convection current originating from the basement of the droplet to the free-surface because of the droplet deformation and recoil together with the vertical surface tension force was the major reason behind the marble formation. The micro-structures on the surface of the particles helped in pinning the bed particles while they were dislodged from the bed. As the surface energy of the droplet was reduced by adding surfactant to the water droplet or by employing a hexane droplet, the three-phase contact line de-pinned from the micro-patterns and did not show lens or marble formation.

(ii) The drop permeation rate was much slower at the initial stage when the drop penetrated through the bed-air interface whereas at the later stage the droplet permeated at a faster rate. Addition of surfactant led to faster permeation of the water droplet through the micro-patterned porous-granular beds, as the droplet de-pinned from the surface of the micro-structures particles. Increase in viscosity of the droplet led to a kinetically stable lens as the time span for the marble formation increased significantly.

(iii) Smaller and hydrophilic micro-porous particles also show a marble effect type phenomenon in which the particles were found to submerge fully or partially inside the droplet, rather than hanging at the outer periphery of the droplet free-surface. The air current coming out of the bed because of the fast permeation of the droplet through the bed of micro-porous particles was found to be the reason behind the movement. The simulations qualitatively show that the particles got connected to the droplet by soaking water through the micro-capillaries.

(iv) Heterogeneous bed composed of mustard-poppy particles showed lens formation and a hint of marble effect taking place simultaneously. Dispensing a water droplet on a poppy-crushed sago bed showed two-different types of marble effect happening in parallel at the different parts of the droplet.

Concisely, the study shows the interesting transitions in the droplet and bed morphologies on uniform and heterogeneous micro-porous or micro-patterned porous-granular beds. A host of novel droplet behaviors such as lens formation and transition from lens to marble effect on bed of micro-patterned particles together with a marble effect type phenomenon on a bed of micro-porous particles have been identified through systematic experiments. A qualitative explanation for the experimental observations is also reported through simulations. The results reported could encourage future research related to the drop impact dynamics on porous or patterned granular beds.

Chapter 6

Conclusions and scope for future work

A detailed study of the instabilities in two-layer flow under the influence of a confining porous substrate has been explored. Three different configurations have been considered for the study namely, (i) a confined two-layer plane Poiseuille flow in an inclined channel (PPFPM), (ii) a confined two-layer Couette flow in a confined channel (CFPM), and (iii) flow of a free bilayer in an inclined channel. The dynamics of droplets on porous granular beds have also been studied through experiments and simulations. The major conclusions of the studies are discussed below.

6.1 INSTABILITY OF A CONFINED TWO-LAYER FLOW ON A POROUS MEDIA

In chapter-2, instabilities of a two-layer Poiseuille flow on a Darcy-Brinkman porous layer have been explored. An Orr-Sommerfeld (O-S) system, derived from the linearized governing equations and boundary conditions, is solved numerically to compare and contrast the time and length scales of the different instability modes. The important conclusions are:

(i) The study uncovers the presence of a pair of, long-wave interfacial mode and finite wavenumber shear mode of instabilities, for almost all possible combinations of viscosity (μ_r) and thickness ratios of the liquid layers (h_r). The interfacial mode is found to be absent only under the condition $\mu_r = h_r$. The observation is in stark contrast to the two-layer flow between non-porous plates where the shear (interfacial) mode appear when $\mu_r < h_r^2$ ($\mu_r > h_r^2$) and at $\mu_r = h_r^2$ the flow is neutrally stable. Importantly, the reduced friction at the liquid layers due to the presence of the porous layer in a microchannel can more readily develop instabilities in a two-phase flow as compared to the similar microchannels with smoother walls, which can eventually lead to a larger mixing of phases, heat and mass transfer, and emulsification of the immiscible phases.

(ii) A permeable thick porous layer with high porosity is found to reduce frictional influence at the liquid layers especially when the lower layer is of low viscosity. The study shows that this reduction in frictional influence from the porous layer rapidly fuels up the instability due to the shear mode whereas the interfacial mode remains relatively dormant to these influences. The strength of the shear mode monotonically increases with porosity, initially increases and then becomes constant with porous layer thickness thereafter initially increases and then reduces with the increase in permeability. Finally it reduces with the increase in the stress jump coefficient across the porous-liquid interface. Thus, a dominant (subdominant) interfacial (shear) mode can be observed by tuning the porous media parameters for all possible μ_r and h_r.

(iii) For a fixed set of porous media parameters the shear mode is found to appear beyond a critical Re especially when $\mu_r > h_r^2$. Further, the results show that introduction of the porous medium can result in multiple shear modes. The eigenfunctions of these modes confirm the location of the critical layers of these shear modes at the porous and the liquid layers.

(iv) The study also shows that the presence of gravity in the inclined channels can act as an additional destabilizing influence and alters the length and the time scales of both the interfacial and the shear modes of the instabilities. Interestingly, the variations in the time and the length scales remain similar to that observed for the non-inclined case. However, the inclination angle plays a crucial role in the transition from dominant interfacial to dominant shear mode of instability when the porous media properties are changed.

(v) The numerical results are validated employing Chebychev-tau spectral and spectral collocation methods. The eigenvalues for the two-layer flow over porous media with infinitesimally thin porous layer are also verified against the existing eigenvalues for the two-layer flow between rigid non-porous substrates (PPF). These exercises endorse the correctness of the results reported.

Briefly, the study shows that the presence of the porous layer leads to a more unstable PPFPM, which can be of significant importance both micro and macroscopically in enhancing heat and mass transfer, mixing or stirring, and emulsification. The instability bounds and modes for a wide range thickness and viscosity of the liquid layers, porosity, permeability and thickness of the porous layer can be useful for fabricating microfluidic or microelectronic devices employing two-layer channel flow.

6.2 INSTABILITY OF A COUETTE TWO-LAYER FLOW ON A POROUS MEDIUM

In chapter-3, the instabilities of a pressure-driven two-layer plane Couette flow on a Darcy-Brinkman porous layer have been explored. An O-S analysis has been carried out by linearizing the governing equations and the boundary conditions of the liquid and the porous layers. The O-S system is solved numerically by employing two different methods to obtain the accurate eigenvalues, which are also validated against the results of the asymptotic cases that are available in the literature. The following are the important conclusions.

(i) The study reports the conventional long-wave interfacial mode and finite-wave-number shear mode of instabilities of a two-layer CF, where the CFPM may develop at least two additional finite-wave-number shear modes because of the movement of the bounding plate and the flow inside the porous layer. Thus, for a CFPM, beyond a critical velocity of the moving plate or beyond some threshold value of the physical properties of the porous layer, a finite-wave-number shear mode(or modes) can be observed for almost all possible combinations of viscosity μ_r and thickness ratios of the liquid layers h_r. Conditionally, we also observe the presence of twin shear modes, one of which grows with bounding plate velocity, whereas the other grows with the increased slippage at the porous-liquid interface.

(ii) A permeable thick porous layer with high porosity is found to reduce frictional influence in the liquid layers especially when the lower layer is of low viscosity. The study shows that the influence of the porous layer affects the shear mode as compared to the interfacial mode. The shear mode is more unstable at high porosity, whereas a porous layer with constant porosity and permeability can only increase the strength of the shear mode till a threshold thickness. The strength of the shear mode is found to increase and then decrease with the increase in permeability. The higher frictional influence with the increase in the stress-jump coefficient causes the reduction in strength of the shear modes and increase in strength of the interfacial modes. The analysis confirms that a transition from a dominant interfacial to a dominant shear mode can be performed only by tuning the velocity of the moving plate and the porous layer parameters for all possible μ_r and h_r.

Concisely, the study shows that the CFPM can be more unstable than conventional pressure-driven two-layer CF or PPF due to the flow inside the underlying porous layer coupled with the movement of the bounding plate. The augmented inertia (reduced friction) due to the presence of the porous layer or due to the movement of the bounding plate can more readily develop the shear modes of instabilities, eventually leading to a larger mixing, heat and mass transfer, and emulsification of the immiscible phases. The reported parameter bounds for the various unstable modes of the porosity, permeability, and thickness of the porous layer can be of importance in future studies related to the two-layer channel flow inside microfluidic devices.

6.3 INSTABILITY OF A FREE BILAYER FLOWING ON AN INCLINED POROUS MEDIUM

In chapter-4, instabilities of an inclined free bilayer flowing over a Darcy-Brinkman porous layer have been explored. An O-S analysis of the governing equations and boundary conditions is performed to uncover the salient features of the instabilities. The major conclusions are,

(i) This configuration can be unstable by pair of long-wave interfacial modes at the free-surface and the interface together with a pair of finite wavenumbers shear modes originating from the inertial influences at the liquid layers. Like a free bilayer on an inclined impervious surface all the unstable modes are found to appear beyond a critical flow rate. All the modes are found to gain strength with increase in the flow rate, ratios of the upper to lower liquid film thickness and viscosities. The interfacial mode specific to the liquid-liquid interface (i^L mode) is found to be present only under the condition $\mu_r \leq 1$.

(ii) One of the shear modes (s^P mode) originates from the augmented inertial influence of the porous layer, which is found to be the dominant mode even at moderate porosity, permeability, and thickness of the porous layer. The strength of the s^P mode, (a) increases with increase in porosity, (b) initially increases and then become constant with increase in porous layer thickness, and (c) initially increases and then reduces with increase in the permeability of the porous layer. Interestingly, interfacial modes (i^L and i^U mode) and the conventional shear mode (s^B mode) specific to a bilayer on an impervious surface are found to be dormant to the change in the porous layer parameters.

(iii) Although the increase in the upper to lower ratios film thicknesses, viscosities, and the flow rate causes larger destabilization to all the modes, the s^P mode dominates when the porous medium is moderately porous, permeable, and thick.

(iv) Additional inertial influence originating from the flow inside porous media is the major reason behind the enhancement of the instability in a free bilayer flowing down an inclined plane.

(v) An eigenfunction analysis shows the location of the s^B mode at the upper layer and the same for the s^P mode near the porous-liquid interface. Also, the phase speed analysis confirms the travelling nature of these instabilities and confirms a progressive increase in the phase speed as the modes are located away from the porous layer ($i^U > s^B > i^L > s^P$) and under the influence of lesser frictional force.

The results reported here of significance in improving the mixing, emulsification, and heat and mass transfer characteristics in the microscale devices.

6.4 DYNAMICS OF A LIQUID DROPLET ON A GRANULAR BED OF MICRO-STRUCTURE PARTICLES

In chapter 5, we explore the permeation of a high surface energy water droplet through a bed of granular particles having micro-structured and micro-porous surfaces. Naturally abundant hydrophobic and hydrophilic particles were incorporated to prepare the uniform and heterogeneous granular beds. The major conclusions are,

(i) A high surface energy droplet on a bed of particles with micro-structured surface could form lens even on a highly porous bed. The three-phase contact line of the droplet was found to pin on the micro-structures present on the bed particles to stabilize a Cassie–Baxter type water lens. The water lens was dynamically transformed into a liquid marble – with a water core encapsulated by micro-patterned particles, when smaller poppy particles with micro-patterned surface formed the granular bed. The duration of the lens and marble formation was found to reduce as the surface energy was reduced by adding surfactant into the water droplet. Computational studies uncovered that the convection current originating from the basement of the droplet to the free-surface because of the droplet deformation and recoil together with the vertical surface tension force induced marble formation. The micro-structures on the surface of the particles helped in pinning the bed particles while they were dislodged from the bed. As the surface energy of the droplet was reduced by adding surfactant to the water droplet or by employing a hexane droplet, the three-phase contact line de-pinned from the micro-patterns on the particle surface and did not show lens or marble formation.

(ii) The drop permeation rate was much slower at the initial stage when the drop penetrated through the bed-air interface whereas at the later stage the droplet permeated at a faster rate. Addition of surfactant led to faster permeation of the water droplet through the micro-patterned porous-granular beds, as the droplet de-pinned from the surface of the micro-structures particles.

(iii) Smaller and hydrophilic micro-porous particles also show a marble effect type phenomenon in which the particles were found to submerge fully or partially inside the droplet, rather than hanging at the outer periphery of the droplet free-surface. The air current coming out of the bed because of the fast permeation of the droplet through the bed of micro-porous particles was found to be the reason behind the movement. The simulations qualitatively show that the particles got connected to the droplet by soaking water through the micro-capillaries.

(iv) Heterogeneous bed composed of mustard-poppy particles showed lens formation and a hint of marble effect taking place simultaneously. Dispensing a water droplet on a poppy-crushed sago bed showed two-different types of marble effect happening in parallel at the different parts of the droplet.

In brief, the study shows the interesting transitions in the droplet and bed morphologies on uniform and heterogeneous micro-porous or micro-patterned porous-granular beds. A host of novel droplet behaviours such as lens formation and transition from lens to marble effect on bed of micro-patterned particles together with a marble effect type phenomenon on a bed of micro-porous particles have been identified through systematic experiments. A qualitative explanation for the experimental observations is also reported through simulations. The results reported could encourage future research related to the drop impact dynamics on porous or patterned granular beds.

6.5 FUTURE WORK

The work presented in this thesis can be extended in many different ways. Some of the interesting systems are,

(i) Instabilities in bilayer flow confined between a pair of deformable permeable walls, mimicking the movements of blood inside the vessels. The interlayer mixing of the two liquids can be enhanced from both sides of the channel. The instabilities can be controlled by the porous media parameters such as the flexibility, thickness, the porosity, and the permeability from both sides.

(ii) The effect of heated porous substrate can be studied for all the three configurations discussed in the thesis, such as the plane Poiseuille and Couette type confined two-layer flow on a heated porous media and free bilayer flow on a heated porous surface. Application of external electromagnetic field to these configurations can be another way to enhance the instability and expedite the mixing of layers, which can have wide applications as microfluidic devices.

(iii) The spatiotemporal linear stability analysis uncovering complex wavenumber and growth coefficient and their subsequent influence on the different instability modes can be one interesting problem to look into in future.

(iv) Full non-linear simulations of the existing configurations are still open problems and can be considered in future to uncover the effect of the nonlinear forces and their consequence to the onset and development on the different modes identified in this work.

REFERENCES

[1] H. S. Yu, and E. M. Sparrow, "Experiments on two-component stratified flow in a horizontal duct," J. Heat Trans. A.S.M.E. **C 91,** 51 (1969).

[2] H. H. Hu, and D. D. Joseph, "Lubricated pipelining: Stability of core-annular flow Part 2," J. Fluid Mech. **205**, 359 (1989).

[3] C. D. Han, *Multiphase Flow in Polymer Processing* (Academic Press, New York, 1981).

[4] P. A. Davidson, and R. I. Lindsay, "Stability of interfacial waves in aluminium reduction cells," J. Fluid Mech. **362**, 273 (1998).

[5] M. Ehrhardt, J. Fuhrmann, A. Linke, and E. Holzbecher, "Mathematical modeling of channel-porous layer interfaces in PEM fuel cells," WAIS preprint, 1375 (2008).

[6] P. X. Jiang, M. H. Fan, G. S. Si, and Z. P. Ren, "Thermal-hydraulic performance of small scale micro-channel and porous-media heat-exchangers," Int. J. Heat Mass Transf. **44**, 1039 (2001).

[7] M. B. Allen, G. A. Behie, and J. A. Trangenstein, *Multiphase flow in porous media. Mechanics, mathematics, and numerics* (Springer-Verlag, Berlin, 1988).

[8] A. R. A. Khaled, and K. Vafai, "The role of porous media in modeling flow and heat transfer in biological tissues," Int. J. Heat Mass Transf. **46**, 4989 (2003).

[9] C.-S. Yih, "Instability due to viscosity stratification," J. Fluid Mech. **27**, 337 (1967).

[10] Y. Renardy, "Instability at the interface between two shearing fluids in a channel," Phys. Fluids **28**, 3441 (1985).

[11] T. I. Hesla, F. R. Pranckh, and L. Preziosi, "Squire's theorem for two stratified fluids," Phys. Fluids **29**, 2808 (1986).

[12] S. G. Yiantsios, and B. G. Higgins, “Linear stability of plane Poiseuille flow of two superposed fluids,” Phys. Fluids **31**, 3225 (1988).

[13] F. Charru, and J. Fabre, “Long wave at the interface between two viscous fluids,” Phys. Fluids **6**, 1223 (1994).

[14] B. S. Tilley, S. H. Davis, and S. G. Bankoff, “Nonlinear long-wave stability of superposed fluids in an inclined channel,” J. Fluid Mech. **277**, 55 (1994).

[15] B. S. Tilley, S. H. Davis, and S. G. Bankoff, “Linear stability theory of two-layer fluid flow in an inclined channel,” Phys. Fluids **6**, 3906 (1994).

[16] M. E. Charles, and Lilleleh.Lu, “An experimental investigation of stability and interfacial waves in co-current flow of two liquids,” J. Fluid Mech. **22**, 217 (1965).

[17] T. W. Kao, and C. Park, “Experimental investigations of the stability of channel flows. Part 2. Two-layered co-current flow in a rectangular channel,” J. Fluid Mech. **52**, 401 (1972).

[18] C. E. Hickox, “Instability due to viscosity and density stratification in axisymmetric pipe flow”. Phys. Fluids **14**, 251 (1971).

[19] D. D. Joseph, M. Renardy, and Y. Renardy, “Instability of the flow of two immiscible liquids with different viscosities in a pipe,” J. Fluid Mech. **141**, 309 (1984).

[20] A. P. Hooper, and W. G. C. Boyd, “Shear-flow instability at the interface between two viscous fluids,” J. Fluid Mech. **128**, 507 (1983).

[21] A. P. Hooper, and W. G. C. Boyd, “Shear-flow instability due to a wall and a viscosity discontinuity at the interface,” J. Fluid Mech. **179**, 201 (1987).

[22] S. A. Orszag, “Accurate solution of the Orr-Sommerfeld stability equation” J. Fluid Mech. **50**, 689 (1971).

[23] A. P. Hooper, “The stability of two superposed viscous fluids in a channel,” Phys. Fluids **1** (7), 1133 (1989).

[24] A. P. Hooper, and R. Grimshaw, “Nonlinear instability at the interface between two viscous fluids,” Phys. Fluids. **28**, 37 (1985).

[25] A. P. Hooper, “Long-wave instability at the interface between two viscous fluids: Thin layer effects,” Phys. Fluids. **28**, 1613 (1985).

[26] Y. Y. Renardy, “The thin layer effect and interfacial stability in a two layer Couette flow with similar liquids,” Phys. Fluids. **30**, 1627 (1987).

[27] P. Barthelet, F. Charru, and J. Fabre, “Experimental study of interfacial long waves in a two layer shear flow,” J. Fluid Mech. **303**, 23 (1995).

[28] F. Charru, and P. Barthelet, “Secondary instability of interfacial waves due to coupling with long wave modes in a two-layer couette flow,” PHYSICA D. **125**, 311 (1999).

[29] F. Charru, and E. J. Hinch, “ ‘Phase diagram’ of interfacial instability in a two-layer Couette flow and mechanism of the long wave instability,” J. Fluid Mech. **414**, 195 (2000).

[30] P. Kapitza, “Wave flow of thin layers of a viscous fluid: I. free flow -II. fluid flow in the presence of continuous gas flow and heat transfer.” (1948). In Collected papers of P.L.Kapitza (ed. D.T. Haar), 690-709. Pergamon 1965, (Original paper in Russian: Zh. Ekper. Teor. Fiz., 18, I. 3-18, II. 19-28).

[31] P. Kapitza, and S. Kapitza, “Wave flow of thin layers of a viscous fluid: III. Experimental study of undulatory flow conditions.” (1949). In Collected papers of P.L.Kapitza (ed. D.T. Haar), 690-709. Pergamon 1965, (Original paper in Russian: Zh. Ekper. Teor. Fiz., 19, 105-120).

[32] T. B. Benjamin, “Wave formation in laminar flow down an inclined plane,” J. Fluid Mech. **2**, 554 (1957).

[33] C. -S. Yih, “Stability of liquid flow down an inclined plane,” Phys. Fluids. **6**, 321 (1963).

[34] A. Samanta, C. Ruyer-Quil, and B. Goyeau, “A falling film down a slippery inclined plane,” J. Fluid Mech. **684,** 353 (2011).

[35] S. W. Joo, and S. H. Davis, “Instabilities of three-dimensional viscous falling films,” J. Fluid Mech. **242**, 529 (1992a).

[36] S. W. Joo, and S. W. Davis, “Irregular waves on viscous falling films,” Chem. Eng. Commun. **118**, 111 (1992b).

[37] J. Liu, J. D. Paul, and J. P. Gollub, “Measurements of the primary instabilities of film flows,” J. Fluid Mech. **250**, 69 (1993).

[38] J. Liu, J. B. Schneider, and J. P. Gollub, “Three dimensional instabilities of film flows,” Phys. Fluids. **A7**, 55 (1995).

[39] J. Zhang, M. J. Miksis, S. G. Bankoff, and G. Tryggvason, “Nonlinear dynamics of an interface in an inclined channel,” Phys. Fluid. **14**, 1877 (2002).

[40] W. Y. Jiang, B. Helenbrook, and S. P. Lin, “Inertial instability of a two-layer liquid film flow,” Phys. Fluid. **16**, 652 (2004).

[41] D. D. Joseph, and Y. Y. Renardy, “Fundamentals of Two-Fluid Dynamics, Part I: Mathematical Theory and Applications,” Springer (1993).

[42] K. P. Chen, “Interfacial instabilities in stratified shear flows involving multiple viscous and viscoelastic fluids,” Appl. Mech. Rev. **48**, 763 (1995).

[43] P. G. Drazin, and W. H. Reid, “Hydrodynamic Stability,” Cambridge university press,

London (1981).

[44] P. A. M. Boomkamp, and R. H. M. Miesen, “Classification of instabilities in parallel two-phase flow,” Int. J. Multiphase Flow. **22**, 67 (1996).

[45] P. G. de Gennes, “Wetting: statics and dynamics,” Reviews of Modern Physics **57**, 827 (1985).

[46] A. Oron, S. H. Davis, and S. G. Bankoff, “Long-scale evolution of thin liquid films,” Rev. Mod. Phys. **69**, 931 (1997).

[47] R. V. Craster, and O. K. Matar, “Dynamics and stability of thin liquid films,” Rev. Mod. Phys. **81**, 1131 (2009).

[48] T. W. Kao, “Stability of 2-layer viscous stratified flow down an inclined plane,” Phys. Fluids **8**, 812 (1965).

[49] T. W. Kao, “Role of interface in stability of stratified flow down an inclined plane,” Phys. Fluids **8**, 2190 (1965).

[50] T. W. Kao, “Role of viscosity stratification in stability of 2-layer flow down an incline,” J. Fluid Mech. **33**, 561 (1968).

[51] D. S. Loewenherz, and C. J. Lawrence, “The effect of viscosity stratification on the stability of a free-surface flow at low Reynolds-number,” Phys. Fluids **A1**, 1686 (1989).

[52] J. Hu, S. Millet, V. Botton, H. Ben Hadid, and D. Henry, “Inertialess temporal and spatio-temporal stability analysis of the two-layer film flow with density stratification,” Phys. Fluids **18**, 104101 (2006).

[53] K. P. Chen, “Wave formation in the gravity-driven low-Reynolds-number flow of 2 liquid-films down an inclined plane,” Phys. Fluids **A5**, 3038 (1993).

[54] W. Y. Jiang, B. Helenbrook, and S. P. Lin, "Inertialess instability of a two-layer liquid film flow," Phys. Fluids **16**, 652 (2004).

[55] M. Amaouche, N. Mehidi, and N. Amatousse, "Linear stability of a two-layer film flow down an inclined channel: A second-order weighted residual approach," Phys. Fluids **19**, 084106 (2007).

[56] K. Alba, R. E. Khayat, and R. S. Pandher, "Steady two-layer gravity-driven thin-film flow," Phys. Rev. E **77**, 056304 (2008).

[57] P. Gao, and X. Y. Lu, "Mechanism of the long-wave inertialess instability of a two-layer film flow," J. Fluid Mech. **608**, 379 (2008).

[58] J. Hu, X. Y. Yin, H. B. Hadid, and D. Henry, "Linear temporal and spatiotemporal stability analysis of two-layer falling films with density stratification," Phy. Rev. E **77**, 026302 (2008).

[59] Gaurav, and V. Shankar, "Role of wall deformability on interfacial instabilities in gravity-driven two-layer flow with a free surface," Phys. Fluids **22**, 094103 (2010).

[60] S. Qian, J. Z. Zhu, and H. H. Bau, "A Stirrer for magnetohydrodynamically controlled minute Fluidic Networks," Phys. Fluids **14**, 3584 (2002).

[61] S. Qian, S. W. Joo, Y. Jiang, and M. A. Cheney, "Free-surface problems in electrokinetic micro- and nanofluidics," Mech. Res. Commun. **36**, 82 (2008).

[62] S. Qian, and H. H. Bau, "Magneto-hydrodynamics based micro fluidics," Mech. Res. Commun. **36**, 10 (2009).

[63] O. Ozen, N. Aubry, D. T. Papageorgiou, and P. G. Petropoulos, "Monodisperse drop formation in square microchannels," Phys. Rev. Lett. **96**, 144501 (2006).

[64] F. Li, O. Ozen, N. Aubry, D. T. Papageorgiou, and P. G. Petropoulos, “Linear stability of a two-fluid interface for electrohydrodynamic mixing in a channel,” J. Fluid Mech. **583**, 347 (2007).

[65] D. Bandyopadhyay, P. D. S. Reddy, A. Sharma, S. W. Joo, and S. Qian, “Electro-Magnetic field induced flow and interfacial instabilities in confined stratified liquid layers,” Theor. Comp. Fluid Dyn. **26**, 23 (2012).

[66] P. D. S. Reddy, D. Bandyopadhyay, S. W. Joo, A. Sharma, S. Qian, “Parametric study on instabilities in a two-layer electromagneto-hydrodynamic channel flow confined between two parallel electrodes,” Phys. Rev. E **83**, 036313 (2011).

[67] D. Bandyopadhyay, R. Gulabani, and A. Sharma, “Instability and dynamics of thin liquid bilayers,” Ind. Eng. Chem. Res. **44**, 1259 (2005).

[68] D. Bandyopadhyay, and A. Sharma, “Nonlinear instabilities and pathways of rupture in thin liquid bilayers,” J. Chem. Phys. **125**, 054711 (2006).

[69] H. H. Bau, J. Zhong, and M. Yi, “A minute magneto hydro dynamic (MHD) mixer,” Sens. Actuators B **79**, 205 (2001).

[70] J. Jang, and S. S. Lee, “Theorectical and experimental study of MHD (magnetohydrodynamic) micropump,” Sens. Actuators **80**, 84 (2000).

[71] B. Ray, D. Bandyopadhyay, S. W. Joo, A. Sharma, S. Qian, and G. Biswas, “Surface instability of a thin electrolyte film undergoing coupled electroosmotic and electrophoretic flows in a microfluidic channel,” Electrophoresis **32**, 1 (2011a).

[72] B. Ray, P. D. S. Reddy, D. Bandyopadhyay, S. W. Joo, A. Sharma, and S. Qian, “Instabilities in free-surface electro-osmotic flows,” Theor. Comp. Fluid. Dyn. **26**, 311 (2011b).

[73] G. S. Beavers, and D. D. Joseph, “Boundary conditions at a naturally permeable wall,” J. Fluid Mech. **30**, 197 (1967).

[74] J. P. Pascal, “Linear stability of fluid flow down a porous inclined plane,” J. Phys. D: Appl. Phys. **32**, 417 (1999).

[75] J. P. Pascal, “Instability of power-law fluid flow down a porous incline,” J. Non-Newtonian Fluid Mech. **133**, 109 (2006).

[76] I. M. R. Sadiq, and R. Usha, “Thin Newtonian film flow down a porous inclined plane: Stability analysis,” Phys. Fluids. **20**, 022105 (2008).

[77] I. M. R. Sadiq, and R. Usha, “Effect of permeability on the instability of a non-Newtonian film down a porous inclined plane,” J. Non-Newton. Fluid **165**, 1171 (2010).

[78] R. Usha, and S. Naire, “A thin film on a porous substrate: A two-sided model, dynamics and stability,” Chem. Eng. Sci. **89**, 72 (2013).

[79] I. M. R. Sadiq, R. Usha, and S. W. Joo, “Instabilities in a liquid film flow over an inclined heated porous substrate,” Chem. Eng. Science **65**, 4443 (2010).

[80] U. Thiele, B. Goyeau, and M. G. Velarde, “Stability analysis of thin film flow along a heated porous wall,” Phys. Fluids. **21**, 014103 (2009).

[81] L. E. Payne, and B. Straughan, “Analysis of the boundary condition at the interface between a viscous fluid and a porous medium and related modeling questions,” J. Math. Pure. Appl. **77**, 317 (1998).

[82] M. H. Chang, F. L. Chen, and B. Straughan, “Instability of Poiseuille flow in a fluid overlying a porous layer,” J. Fluid Mech. **564**, 287 (2006).

[83] R. Liu, Q. S. Liu, and S. C. Zhao, "Instabilities of plane Poiseuille flow in a fluid-porous system," Phys. Fluids. **20**, 104105 (2008).

[84] R. Liu, and Q. S. Liu, "Instabilities of a liquid film flowing down an inclined porous plane," Phys. Rev. E Physical Re. **80**, 036316 (2009).

[85] R. Liu, and Q. S. Liu, "Instabilities and transient behaviors of a liquid film flowing down a porous inclined plane," Phys. Fluids. **22**, 074101 (2010).

[86] A. A. Hill, and B. Straughan, "Poiseuille flow in a fluid overlying a porous medium," J. Fluid Mech. **603**, 137 (2008).

[87] A. A Hill, and B. Straughan, "Poiseuille flow in a fluid overlying a highly porous material," Adv. Water Resour. **32**, 1609 (2009a).

[88] A. A. Hill, and B. Straughan, "Global stability for thermal convection in a fluid overlying a highly porous material," Proc. Roy. Soc. London A. **465**, 207 (2009b).

[89] Anjalaiah, R. Usha, and S. Millet, "Thin film flow down a porous substrate in the presence of an insoluble surfactant: Stability analysis," Phys. Fluids **25**, 022101 (2013).

[90] A. Samanta, B. Goyeau, and C. Ruyer-Quil, "A falling film on a porous medium," J. Fluid Mech. **716**, 414 (2013).

[91] B. Goyean, D. Lhuillier, D. Gobin, and M. G. Velarde, "Momentum transport at a fluid-porous interface," Int. J. Heat Mass. Tran. **46**, 4071 (2003).

[92] J. A. Ochoa-Tapia, and S. Whitaker**,** "Momentum transfer at the boundary between a porous medium and a homogeneous fluid-I. Theoretical development," Int. J. Heat Mass. Tran. 30, 2635 (1995).

[93] J.J. Dongarra, B. Straughan, and D. W. Walker, "Chebyshev tau-QZ algorithm methods for calculating spectra of hydrodynamic stability problems," Appl. Numer.

Maths **22**, 399 (1996).

[94] D. Gottlieb, and S. A. Orszag, “Numerical Analysis of Spectral Methods: Theory and Applications,” (CBMS Regional Conference Series in Applied Mathematics, 1977).

[95] J. A. C. Weideman, and S. C. Reddy, “A MATLAB differentiation matrix suite,” ACM Trans. Math. Soft. **26**, 465 (2000).

[96] B. Bhushan, Y. C. Jung, and K. Koch, “Micro-, nano- and hierarchical structures for superhydrophobicity, self-cleaning and low adhesion,” Philos. T. Roy. Soc. A, **367**,1631 (2009).

[97] W. Barthlott, and C. Neinhuis, “Purity of the sacred lotus, or escape from contamination in biological surfaces,” Planta, **202**, 1 (1997).

[98] C. Neinhuis, and W. Barthlott, “Characterization and distribution of water-repellent, self-cleaning plant surfaces,” Ann. Bot., **79**, 667 (1997).

[99] H. J. Melosh, *Impact Cratering: A Geologic Process*, (Oxford University Press, New York, 1989).

[100] A. M. Worthington, *The Splash of a Drop*, (General Literature Committee, London, 1895).

[101] R. D. Deegan, P. Brunet, and J. Eggers, “Complexities of splashing,” Nonlinearity, **21**, C1 (2008).

[102] R. Rioboo, C. Bauthier, J. Conti, M. Voue, and J. De Coninck, “Experimental investigation of splash and crown formation during single drop impact on wetted surfaces,” Exp. Fluids, **35**, 648 (2003).

[103] R. Bergmann, D. van der Meer, M. Stijnman, M. Sandtke, A. Prosperetti, and D. Lohse, “Giant bubble pinch-off,” Phys. Rev. Lett., **96**, 154505 (2006).

[104] A. L. Yarin, “Drop impact dynamics: Splashing, spreading, receding, bouncing,” Annu. Rev. Fluid Mech., **38**, 159 (2006).

[105] L. Xu, “Instability development of a viscous liquid drop impacting a smooth substrate,” Phys. Rev. E, **82**, 025303 (2010).

[106] K. P. Hapgood, J. D. Litster, S. R. Biggs, and T. Howes, “Drop penetration into porous powder beds,” J. Colloid Interf. Sci., **253**, 353 (2002).

[107] G. Delon, S. Dorbolo, N. Vandewalle, and H. Caps, 62nd. Annual Meeting of the APS Division of Fluid Dynamics. **54**, AH.00006 (2009).

[108] E. Nefzaoui, and O. Skurtys, “Impact of a liquid drop on a granular medium: Inertia, viscosity and surface tension effects on the drop deformation,” Experimental Thermal and Fluid Science, **41**, 43 (2012).

[109] H. Katsuragi, “Morphology Scaling of Drop Impact onto a Granular Layer,” Phys. Rev. Lett., **104**, 218001 (2010).

[110] P. Taylor, “The wetting of leaf surfaces,” Curr. Opin. Colloid Interf. Sci., **16**, 326 (2011).

[111] G. Delon, D. Terwagne, S. Dorbolo, N. Vandewalle, and H. Caps, “Impact of liquid droplets on granular media,” Phys. Rev. E, **84**, 046320 (2011).

[112] P. Aussillous, and D. Quere, “Liquid marbles,” Nature, **411**, 924 (2001).

[113] M. Dandan, and H. Y. Erbil, “Evaporation Rate of Graphite Liquid Marbles: Comparison with Water Droplets,” Langmuir, **25**, 8362 (2009).

[114] E. Bormashenko, “New insights into liquid marbles,” Soft Matter, **8**, 11018 (2012).

[115] C. P. Whitby, X. Bian, and R. Sedev, “Spontaneous liquid marble formation on packed porous beds,” Soft Matter, **8**, 11336 (2012).

[116] G. McHale, and M. I. Newton, “Liquid marbles: principles and applications,” Soft Matter, **7**, 5473 (2011).

[117] E. Bormashenko, R. Balter, and D. Aurbach, “Use of Liquid Marbles as Micro-Reactors,” Int. J. Chem. React. Engg., **9**, S10 (2011).

[118] E. Bormashenko, R. Balter, and D. Aurbach, “Formation of liquid marbles and wetting transitions,” J. Colloid Interf. Sci., **384**, 157 (2012).

[119] B. P. Binks, and R. Murakami, “Phase inversion of particle-stabilized materials from foams to dry water,” Nature Materials, **5**, 865 (2006).

[120] D. Dupin, S. P. Armes, and S. Fujii, “Stimulus-Responsive Liquid Marbles,” J. Am. Chem. Soc., **131**, 5386 (2009).

[121] S. Fujii, S. Kameyama, S. P. Armes, D. Dupin, M. Suzaki, and Y. Nakamura, “pH-responsive liquid marbles stabilized with poly(2-vinylpyridine) particles,” Soft Matter, **6**, 635 (2010).

[122] L. C. Gao, and T. J. McCarthy, “Reply to "Comment on How Wenzel and Cassie Were Wrong by Gao and McCarthy",” Langmuir, **23**, 13243 (2007).

[123] Y. H. Xue, H. X. Wang, Y. Zhao, L. M. Dai, L. F. Feng, X. G. Wang, and T. Lin, “Magnetic Liquid Marbles: A "Precise" Miniature Reactor,” Adv. Mater., **22**, 4814 (2010).

[124] D. Matsukuma, H. Watanabe, H. Yamaguchi, and A. Takahara, “Preparation of Low-Surface-Energy Poly 2-(perfluorooctyl)ethyl acrylate Microparticles and Its Application to Liquid Marble Formation,” Langmuir, **27**, 1269 (2011).

[125] Y. L. Zhang, H. Xia, E. Kim, and H. B. Sun, “Recent developments in superhydrophobic surfaces with unique structural and functional properties,” Soft Matter, **8**, 11217 (2012).

[126] T. Nguyen, W. Shen, and K. Hapgood, “Drop penetration time in heterogeneous powder beds,” Chem. Engg. Sci., **64**, 5210 (2009).

[127] N. Eshtiaghi, and K. P. Hapgood, “A quantitative framework for the formation of liquid marbles and hollow granules from hydrophobic powders,” Powder Tech., **223**, 65 (2012).

[128] I. S. Aranson, and L. S. Tsimring, “Patterns and collective behavior in granular media: Theoretical concepts,” Rev. Mod. Phys., **78**, 641 (2006).

[129] S. H. Davis, and L. M. Hocking, “Spreading and imbibition of viscous liquid on a porous base,” Phys. Fluids **11**, 1 (1999).

[130] S. H. Davis, and L. M. Hocking, “Spreading and imbibition of viscous liquid on a porous base. II,” Phys. Fluids **12**, 7 (2000).

[131] X. Frank, and P. Perre, “Droplet spreading on a porous surface: A lattice Boltzmann study,” Phys. Fluids **24**, 042101 (2012).

[132] V. M. Starov, M. G. Velarde and C. J. Radke, *Wetting and spreading dynamics* (CRC press, Boca Raton, 2007).

[133] J. U. Brackbill, D. B. Kothe, and C. Zemach, “A continuum method for modeling surface-tension,” J. Comput. Phys., **100**, 335 (1992).

APPENDIX A

The base-state governing equations are

$$\bar{U}_{1ZZ} = P_{0X} - G\sin\alpha\,, \tag{A1}$$

$$\bar{U}_{2ZZ} = (1/\mu_r)P_{0X} - (1/\nu_r)G\sin\alpha\,, \tag{A2}$$

$$(1/b)\bar{U}_{mZZ} - (1/Da)\bar{U}_m = P_{0X} - G\sin\alpha\,. \tag{A3}$$

The dimensionless no-slip boundary condition at the porous-solid interface $(Z = -D_m)$ is

$$\bar{U}_m = 0\,. \tag{A4}$$

The dimensionless no-slip boundary condition at the liquid-solid interface $(Z = B)$ is

$$\bar{U}_2 = 0\,. \tag{A5}$$

The dimensionless form of the continuity of velocity, and the stress jump conditions at the liquid-porous interface $(Z = 0)$ are

$$\bar{U}_1 = \bar{U}_m\,, \tag{A6}$$

$$(1/b)\bar{U}_{mZ} - \bar{U}_{1Z} - \left(\chi/\sqrt{Da}\right)\bar{U}_m = 0\,. \tag{A7}$$

The dimensionless form of the continuity of velocity, and tangential stress balances at the liquid-liquid interface $(Z = 1)$ are

$$\bar{U}_1 = \bar{U}_2\,, \tag{A8}$$

$$\bar{U}_{1Z} = \mu_r\left(\bar{U}_{2Z}\right). \tag{A9}$$

The above governing equations and boundary conditions yields

$$\bar{U}_1 = C_{11}Z^2 + C_{12}Z + C_{13},\ \ 0 \le Z \le 1\,, \tag{A10}$$

$$\bar{U}_2 = C_{21}Z^2 + C_{22}Z + C_{23},\ \ 1 \le Z \le B\,, \tag{A11}$$

$$\bar{U}_m = C_{m1}\,\mathrm{e}^{MZ} + C_{m2}\,\mathrm{e}^{-MZ} + C_{m3}, \quad -D_m \le Z \le 0\,, \tag{A12}$$

$$C_{11} = \left(P_{0X} - G^*\right)\big/2\,, \tag{A13}$$

$$C_{12} = \frac{a_2\left(P_{0X} - G^*\right) + C_{13}\phi}{a_1}\,, \tag{A14}$$

$$C_{13} = \left(\frac{a_4}{2a_3}\right)\left(P_{0X} - G^*\right) - \left(\frac{a_1 a_5}{2a_3}\right)\left(P_{0X} - \rho_r G^*\right), \tag{A15}$$

$$C_{21} = \frac{\left(P_{0X} - \rho_r G^*\right)}{2\mu_r}\,, \tag{A16}$$

$$C_{22} = \frac{a_2 + a_1}{a_1\mu_r}\left(P_{0X} - G^*\right) - \frac{1}{\mu_r}\left(P_{0X} - \rho_r G^*\right) + \frac{\phi}{a_1\mu_r}C_{13}\,, \tag{A17}$$

$$C_{23} = -\frac{\left(P_{0X} - \rho_r G^*\right)B^2}{2\mu_r} - C_{22}B\,, \tag{A18}$$

$$C_{m1} = -\left(\frac{Da\left(F_- - 1\right)\left(P_{0X} - G^*\right) + C_{13}F_-}{a_1}\right), \tag{A19}$$

$$C_{m2} = \frac{Da\left(F_+ - 1\right)\left(P_{0X} - G^*\right) + C_{13}F_+}{a_1}\,, \tag{A20}$$

$$C_{m3} = -Da\left(P_{0X} - G^*\right). \tag{A21}$$

where $\phi = F_- J_+ + F_+ J_-$; $\psi = \dfrac{\chi\left(F_+ - F_-\right)}{\sqrt{Da}} - 2\sqrt{\dfrac{1}{b\,Da}}$; $G^* = G\sin\alpha\,, F_+ = e^{\sqrt{b/Da}\,D_m}$;

$F_- = e^{-\sqrt{b/Da}\,D_m}$; $J_+ = \left(\sqrt{1/b\,Da} + \chi/\sqrt{Da}\right)$; $J_- = \left(\sqrt{1/b\,Da} - \chi/\sqrt{Da}\right)$; $M = \sqrt{b/Da}\,,$

$a_1 = \left(F_+ - F_-\right)$; $a_2 = \left(Da\left(\phi - J_- - J_+\right) + a_1\chi\sqrt{Da}\right)$; $a_3 = \left(B-1\right)\phi + \left(\phi + a_1\right)\mu_r\,,$

$a_5 = \left(B-1\right)^2$; $a_4 = \left(1 - B - \mu_r\right)2a_2 + \left(2 - 2B - \mu_r\right)a_1$;

From equation (38)

$$P_{0X}=\frac{\left(\begin{array}{l} 6G^{*}\left(-4Da\left(F_{+}-1\right)^{2}F_{-}\mu_{r}+M\left(\left(B-1\right)^{2}-\mu_{r}\right)a_{2}\right)a_{3} \\ +3G^{*}\left(-2\left(F_{+}-1\right)^{2}F_{-}\mu_{r}+M\left(\left(B-1\right)^{2}-\mu_{r}\right)\phi\right)a_{4}+6M\mu_{r}a_{1}^{2}G^{*}\rho_{r}a_{5} \\ +a_{1}\left(\begin{array}{l} 2M\left(-6Q\mu_{r}+G^{*}\left(3-6B+3B^{2}-\mu_{r}+6DDa\mu_{r}+2\left(B-1\right)^{3}\rho_{r}\right)\right)a_{3} \\ -6G^{*}M\mu_{r}a_{4}+3\left(2\left(F_{+}-1\right)^{2}F_{-}\mu_{r}+MG^{*}\rho_{r}a_{5}\left(-\left(B-1\right)^{2}+\mu_{r}\right)\phi\right) \end{array}\right) \end{array}\right)}{\left(\begin{array}{l} -2\left(\begin{array}{l} 12Da\left(F_{+}-1\right)^{2}F_{-}\mu_{r}+M\left(-1+\left(3-2B\right)B^{2}+\mu_{r}-6DDa\mu_{r}\right)a_{1} \\ +3M\left(-\left(B-1\right)^{2}+\mu_{r}\right)a_{2} \end{array}\right)a_{3} \\ +3\left(2\left(F_{+}-1\right)^{2}F_{-}\mu_{r}+M\left(-\left(B-1\right)^{2}+\mu_{r}\right)\phi+2M\mu_{r}a_{1}\right)\left(a_{1}a_{5}-a_{4}\right) \end{array}\right)}. \tag{A22}$$

APPENDIX B

The base-state governing equations are

$$\bar{U}_{1ZZ} = P_{0X} - G\sin\alpha\,, \tag{B1}$$

$$\bar{U}_{2ZZ} = \left(1/\mu_r\right)P_{0X} - \left(1/\nu_r\right)G\sin\alpha\,, \tag{B2}$$

$$\left(1/b\right)\bar{U}_{mZZ} - \left(1/Da\right)\bar{U}_m = P_{0X} - G\sin\alpha\,. \tag{B3}$$

The dimensionless no-slip boundary condition at the porous-solid interface $\left(Z = -D_m\right)$ is

$$\bar{U}_m = 0\,. \tag{B4}$$

The dimensionless no-slip boundary condition at the liquid-solid interface $\left(Z = B\right)$ is

$$\bar{U}_2 = V. \tag{B5}$$

The dimensionless form of the continuity of velocity, and the stress jump condition at the liquid-porous interface $\left(Z = 0\right)$ are

$$\bar{U}_1 = \bar{U}_m\,, \tag{B6}$$

$$\left(1/b\right)\bar{U}_{mZ} - \bar{U}_{1Z} - \left(\chi/\sqrt{Da}\right)\bar{U}_m = 0\,. \tag{B7}$$

The dimensionless form of the continuity of velocity, and the tangential stress balance at the liquid-liquid interface $\left(Z = 1\right)$ are

$$\bar{U}_1 = \bar{U}_2\,, \tag{B8}$$

$$\bar{U}_{1Z} = \mu_r\left(\bar{U}_{2Z}\right). \tag{B9}$$

The above governing equations and boundary conditions yield

$$\bar{U}_1 = C_{11}Z^2 + C_{12}Z + C_{13},\quad 0 \le Z \le 1\,, \tag{B10}$$

$$\bar{U}_2 = C_{21}Z^2 + C_{22}Z + C_{23},\quad 1 \le Z \le B\,, \tag{B11}$$

$$\bar{U}_m = C_{m1}\,\mathrm{e}^{MZ} + C_{m2}\,\mathrm{e}^{-MZ} + C_{m3}, \quad -D_m \le Z \le 0, \tag{B12}$$

$$C_{11} = \left(P_{0X} - G^*\right)/2\,, \tag{B13}$$

$$C_{12} = \frac{a_2\left(P_{0X} - G^*\right) + C_{13}\phi}{a_1}\,, \tag{B14}$$

$$C_{13} = \left(\frac{a_4}{2a_3}\right)\left(P_{0X} - G^*\right) - \left(\frac{a_1 a_5}{2a_3}\right)\left(P_{0X} - \rho_r G^*\right), \tag{B15}$$

$$C_{21} = \frac{\left(P_{0X} - \rho_r G^*\right)}{2\mu_r}\,, \tag{B16}$$

$$C_{22} = \frac{a_2 + a_1}{a_1\mu_r}\left(P_{0X} - G^*\right) - \frac{1}{\mu_r}\left(P_{0X} - \rho_r G^*\right) + \frac{\phi}{a_1\mu_r}C_{13}\,, \tag{B17}$$

$$C_{23} = -\frac{\left(P_{0X} - \rho_r G^*\right)B^2}{2\mu_r} - C_{22}B\,, \tag{B18}$$

$$C_{m1} = -\left(\frac{Da\left(F_- - 1\right)\left(P_{0X} - G^*\right) + C_{13}F_-}{a_1}\right), \tag{B19}$$

$$C_{m2} = \frac{Da\left(F_+ - 1\right)\left(P_{0X} - G^*\right) + C_{13}F_+}{a_1}\,, \tag{B20}$$

$$C_{m3} = -Da\left(P_{0X} - G^*\right). \tag{B21}$$

where $\phi = F_- J_+ + F_+ J_-$; $\psi = \chi\left(F_+ - F_-\right)Da^{-1/2} - 2\left(b\,Da\right)^{-1/2}$; $G^* = G\sin\alpha$; $F_+ = e^{\sqrt{b/Da}\,D_m}$;

$M = \sqrt{b/Da}$; $F_- = e^{-\sqrt{b/Da}\,D_m}$; $J_+ = \left(\sqrt{1/b\,Da} + \chi/\sqrt{Da}\right)$; $J_- = \left(\sqrt{1/b\,Da} - \chi/\sqrt{Da}\right)$;

$a_1 = \left(F_+ - F_-\right)$; $a_5 = \left(B-1\right)^2$; $a_2 = \left(Da\left(\phi - J_- - J_+\right) + a_1\chi\sqrt{Da}\right)$; $a_3 = \left(B-1\right)\phi + \left(\phi + a_1\right)\mu_r$;

$a_4 = \left(1 - B - \mu_r\right)2a_2 + \left(2 - 2B - \mu_r\right)a_1$.

APPENDIX C

The base-state governing equations are

$$\bar{U}_{1ZZ} = -G\sin\alpha\,, \tag{C1}$$

$$\bar{U}_{2ZZ} = -(1/\nu_r)G\sin\alpha\,, \tag{C2}$$

$$(1/b)\bar{U}_{mZZ} - (1/Da)\bar{U}_m = -G\sin\alpha\,. \tag{C3}$$

The dimensionless no-slip boundary condition at the porous-solid interface $(Z = -D_m)$ is

$$\bar{U}_m = 0\,. \tag{C4}$$

The dimensionless form of the continuity of velocity, and the stress jump conditions at the liquid-porous interface $(Z = 0)$ are

$$\bar{U}_1 = \bar{U}_m\,, \tag{C5}$$

$$(1/b)\bar{U}_{mZ} - \bar{U}_{1Z} - \left(\chi/\sqrt{Da}\right)\bar{U}_m = 0\,. \tag{C6}$$

The dimensionless form of the continuity of velocity, and tangential stress balances at the liquid-liquid interface $(Z = 1)$ are

$$\bar{U}_1 = \bar{U}_2\,, \tag{C7}$$

$$\bar{U}_{1Z} = \mu_r\left(\bar{U}_{2Z}\right). \tag{C8}$$

The dimensionless stress balance condition at the liquid-air interface $(Z = H_2)$ is

$$\bar{U}_{2Z} = 0\,. \tag{C9}$$

The above governing equations and boundary conditions yields

$$\bar{U}_1 = C_{11}Z^2 + C_{12}Z + C_{13},\ 0 \le Z \le 1\,, \tag{C10}$$

$$\bar{U}_2 = C_{21}Z^2 + C_{22}Z + C_{23},\ 1 \le Z \le B\,, \tag{C11}$$

$$\bar{U}_m = C_{m1}\,\mathrm{e}^{MZ} + C_{m2}\,\mathrm{e}^{-MZ} + C_{m3},\ -D_m \le Z \le 0\,, \tag{C12}$$

$$C_{11} = -G\sin\alpha/2\,, \tag{C13}$$

$$C_{12} = -2C_{11} - 2\mu_r\left(H_2 - 1\right)C_{21}\,, \tag{C14}$$

$$C_{13} = \left[\begin{array}{l}\left(\dfrac{\chi\left(F_+ - F_-\right) - \sqrt{Da}\left(J_+ + J_- - \phi\right)}{\phi\sqrt{Da}}\right)C_{m3} \\ -\dfrac{2\left(F_+ - F_-\right)}{\phi}C_{11} - \dfrac{2\mu_r\left(H_2 - 1\right)\left(F_+ - F_-\right)}{\phi}C_{21}\end{array}\right], \tag{C15}$$

$$C_{21} = -G\sin\alpha/2\nu_r\,, \tag{C16}$$

$$C_{22} = -2C_{21}H_2\,, \tag{C17}$$

$$C_{23} = C_{11} + C_{12} + C_{13} + \left(2H_2 - 1\right)C_{21}\,, \tag{C18}$$

$$C_{m1} = \frac{\left(F_- - 1\right)C_{m3} - F_- C_{13}}{\left(F_+ - F_-\right)}\,, \tag{C19}$$

$$C_{m2} = -\frac{\left(F_+ - 1\right)C_{m3} - F_+ C_{13}}{\left(F_+ - F_-\right)}\,, \tag{C20}$$

$$C_{m3} = DaG\sin\alpha\,. \tag{C21}$$

where $\phi = F_- J_+ + F_+ J_-$; $F_+ = e^{\sqrt{b/Da}\,D_m}$; $F_- = e^{-\sqrt{b/Da}\,D_m}$; $J_+ = \left(\sqrt{1/b\,Da} + \chi/\sqrt{Da}\right)$;

$M = \sqrt{b/Da}$; $J_- = \left(\sqrt{1/b\,Da} - \chi/\sqrt{Da}\right)$.